

For Reference

NOT TO BE TAKEN FROM THIS ROOM

Ex LIBRIS
UNIVERSITATIS
ALBERTAENSIS





Digitized by the Internet Archive
in 2022 with funding from
University of Alberta Libraries

<https://archive.org/details/Beamish1982>

THE UNIVERSITY OF ALBERTA

RELEASE FORM

NAME OF AUTHOR: John Richard Beamish

TITLE OF THESIS: Dislocations and Sound Propagation in
Solid ^3He and ^4He .

DEGREE FOR WHICH THESIS WAS PRESENTED: Ph.D.

YEAR THIS DEGREE GRANTED: 1982

Permission is hereby granted to THE UNIVERSITY OF ALBERTA LIBRARY to reproduce single copies of this thesis and to lend or sell such copies for private, scholarly or scientific research purposes only.

The author reserves other publication rights, and neither the thesis nor extensive extracts from it may be printed or otherwise reproduced without the author's written permission.

THE UNIVERSITY OF ALABAMA

RELEASE FORM

NAME OF AUTHOR: JOHN F. BARNES

TITLE OF PAPER: REPRODUCTION AND OTHER INFORMATION

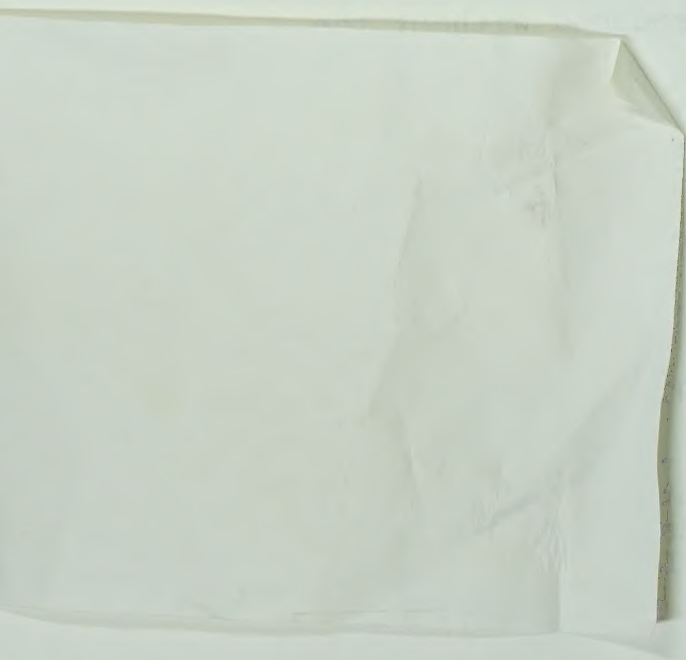
DATE: 10-1-60

DEGREE FOR WHICH THIS IS SUBMITTED: M. A.

YEAR THIS DEGREE AWARDED: 1960

Reproduction is hereby granted to the University
of Alabama Libraries as copyright owner of this
thesis and to lend or sell this copy to the
University of Alabama Libraries.
The author reserves all other rights.
and retains the right to publish elsewhere.

may be printed or otherwise reproduced
author's written permission.



THE UNIVERSITY OF ALBERTA

DISLOCATIONS AND SOUND PROPAGATION

IN SOLID ^3He AND ^4He

by

JOHN RICHARD BEAMISH

A THESIS

SUBMITTED TO THE FACULTY OF GRADUATE STUDIES AND RESEARCH
IN PARTIAL FULFILMENT OF THE REQUIREMENTS FOR THE DEGREE
OF DOCTOR OF PHILOSOPHY IN PHYSICS.

DEPARTMENT OF PHYSICS

EDMONTON, ALBERTA

SPRING 1982

THE UNIVERSITY OF ALBERTA

FACULTY OF GRADUATE STUDIES AND RESEARCH

The undersigned certify that they have read, and recommend to the Faculty of Graduate Studies and Research, for acceptance, a thesis entitled Dislocations and Sound Propagation in Solid ^3He and ^4He submitted by John Richard Beamish in partial fulfilment of the requirements for the degree of Doctor of Philosophy in Physics.

DEDICATION

I would like to dedicate this thesis to my father,
Elton Beamish.

ACKNOWLEDGEMENTS

I would like to express my gratitude to my supervisor, Professor J.P. Franck for his generous support and encouragement.

The expert technical assistance of Alan O'Shea was invaluable and greatly appreciated. I would also like to thank Mrs. Ruth Nelson for her efficient and accurate typing of this thesis.

Awards of scholarships from the National Research Council of Canada and from the Province of Alberta are gratefully acknowledged.

Finally, I would like to thank my wife Kathie for her support and active encouragement.

TABLE OF CONTENTS

CHAPTER	PAGE
1. INTRODUCTION	1
2. BACKGROUND	6
2.1 Lattice Dynamics and Elastic Properties	6
2.2 Sound Velocity and Attenuation in an Ideal Solid	16
2.3 Crystal Defects and Sound Propagation	21
2.4 Experimental Results in Solid Helium	30
3. EXPERIMENT	39
3.1 Experimental Apparatus	39
3.1-1 Refrigeration	39
3.1-2 Thermometry and Temperature Control	43
3.1-3 Pressure System	47
3.1-4 Ultrasonic Cell	50
3.1-5 Ultrasonic Electronics	53
3.1-6 Sample Gas	61
3.2 Experimental Procedures	62
3.2-1 Cooling Down	62
3.2-2 Pressurizing and Cooling the Sound Cell	64
3.2-3 Crystal Growth	65
3.2-4 Ultrasonic Measurements	70
4. EXPERIMENTAL RESULTS AND ANALYSIS	74
4.1 Introduction	74
4.2 hcp ^3He	81
4.2-1 hcp ^3He 5 (@ 18.6 cm ³ /mole)	81

CHAPTER	PAGE
4.2-2 hcp ^3He (@ 18.6 cm ³ /mole)	98
4.2-3 hcp ^3He (@ 17.8 cm ³ /mole)	102
4.2-4 Effects of Impurities	105
4.3 bcc ^3He	117
4.3-1 bcc ^3He 43 (@ 20.1 cm ³ /mole)	117
4.3-2 bcc ^3He (@ 20.1 cm ³ /mole)	120
4.3-3 bcc ^3He (@ 22.3 and 24.2 cm ³ /mole)	123
4.3-4 Effects of Impurities	129
4.4 hcp ^4He	141
4.4-1 hcp ^4He (@ 17.7 cm ³ /mole)	141
4.4-2 hcp ^4He (@ 20.3 cm ³ /mole)	144
4.4-3 Effects of Impurities	146
4.5 Adiabatic Region	149
4.6 Thermally Activated Recovery	157
4.7 Dislocation Parameters	167
4.8 Zero Sound	171
5. DISCUSSION AND CONCLUSIONS	174
5.1 Discussion	174
5.2 Conclusion	194
Bibliography	195

LIST OF TABLES

Table	Description	Page
1	Adiabatic Sound Velocity in hcp ^3He	153
2	Adiabatic Sound Velocity in bcc ^3He	154
3	Adiabatic Sound Velocity in hcp ^4He	155
4	Recovery Rates in ^3He	161
5	Thermal Activation Energies in ^3He	166
6	Dislocation Parameters for hcp ^3He	168
7	Dislocation Parameters for bcc ^3He	169
8	Dislocation Parameters for hcp ^4He	170

LIST OF FIGURES

Figure		Page
1.1	Solid phase diagrams of ^3He and ^4He	3
2.1	Orientation dependence of sound velocities and beam deviations in hcp ^4He at $17.7 \text{ cm}^3/\text{mole}$	15
2.2	Dislocation contributions to velocity and attenuation as a function of loop length	25
2.3	Dislocation contributions to velocity and attenuation of a distribution of loop lengths	27
2.4	Dislocation orientation factors in hcp ^4He at $17.7 \text{ cm}^3/\text{mole}$	29
2.5	Dislocation contributions to velocity and attenuation as functions of temperature	31
2.6	Dislocation contributions to velocity and attenuation as functions of frequency	32
3.1	Cryostat	41
3.2	Pumping systems	45
3.3	Pressure system	49
3.4	Ultrasonic cell	52
3.5	Block diagram of ultrasonic electronics	54
3.6	Echo envelopes: (A) Liquid helium (B) Solid hcp helium	59
4.1	v and α in hcp ^3He 5 @ 3 MHz	82
4.2	v and α in hcp ^3He 5 @ 9 MHz	83
4.3	v and α in hcp ^3He 5 @ 21 MHz	84
4.4	Time and pulse number dependence of high amplitude 3 MHz pulse effect	87
4.5	Temperature dependence of high amplitude 3 MHz pulse effect	89

Figure		Page
4.6	Dislocation pinning by high amplitude 3 MHz pulses (effect on v and α)	91
4.7	Effect of temperature dependence of dislocation damping on velocity fits	93
4.8	Dislocation fits (3, 9 and 21 MHz) of v and α for hcp ^3He 5 using 9 MHz velocity data	95
4.9	Dislocation fits (3, 9 and 21 MHz) of v and α for hcp ^3He 5 using 21 MHz velocity data	97
4.10	Dislocation fits (3 and 9 MHz) of v and α for hcp ^3He 2	100
4.11	Dislocation fits (3 and 9 MHz) of v and α for hcp ^3He 3	101
4.12	v and α in hcp ^3He 7 ($17.8 \text{ cm}^3/\text{mole}$) @ 3 MHz	103
4.13	v and α in hcp ^3He 7 ($17.8 \text{ cm}^3/\text{mole}$) @ 9 MHz	104
4.14	Dislocation fits (3 and 9 MHz) of v and α for hcp ^3He 7	106
4.15	Dislocation fits (3 and 9 MHz) of v and α for $^*\text{hcp } ^3\text{He}$ 12 ($47 \text{ ppm } ^4\text{He}$)	108
4.16	Dislocation fits (3 and 9 MHz) of v and α for $^{**}\text{hcp } ^3\text{He}$ 12 ($430 \text{ ppm } ^4\text{He}$)	109
4.17	v and α in $^{***}\text{hcp } ^3\text{He}$ 17 ($0.53\% ^4\text{He}$) @ 3 MHz	110
4.18	v and α in $^{***}\text{hcp } ^3\text{He}$ 17 ($0.53\% ^4\text{He}$) @ 21 MHz	111
4.19	Amplitude dependence in $^{***}\text{hcp } ^3\text{He}$ 17 ($0.53\% ^4\text{He}$)	113
4.20	Amplitude dependence of attenuation and critical stress in $^{***}\text{hcp } ^3\text{He}$ 17 ($0.53\% ^4\text{He}$)	115

Figure		Page
4.21	v and α in bcc ^3He 43 @ 3 MHz	118
4.22	v and α in bcc ^3He 43 @ 9 MHz	119
4.23	Dislocation fits (3 and 9 MHz) of v and α for bcc ^3He 43	121
4.24	Dislocation fits (3, 9 and 21 MHz) of v and α for bcc ^3He 36	122
4.25	v and α in bcc ^3He 45 ($22.3 \text{ cm}^3/\text{mole}$) @ 3 MHz	124
4.26	v in bcc ^3He 45 ($22.3 \text{ cm}^3/\text{mole}$) @ 9 MHz	125
4.27	v and α in bcc ^3He 46 ($24.2 \text{ cm}^3/\text{mole}$) @ 3 MHz	127
4.28	v and α in bcc ^3He 46 ($24.2 \text{ cm}^3/\text{mole}$) @ 9 MHz	128
4.29	v and α in $^*\text{bcc}$ ^3He 50 (47 ppm ^4He) @ 3 MHz	130
4.30	v and α in $^*\text{bcc}$ ^3He 50 (47 ppm ^4He) @ 9 MHz	131
4.31	Dislocation fits (3 and 9 MHz) of v and α for $^*\text{bcc}$ ^3He 50 (47 ppm ^4He)	132
4.32	v and α in $^{**}\text{bcc}$ ^3He 54 (430 ppm ^4He) @ 3 MHz	133
4.33	v and α in $^{**}\text{bcc}$ ^3He 54 (430 ppm ^4He) @ 9 MHz	134
4.34	Dislocation fits (3 and 9 MHz) of v and α for $^{**}\text{bcc}$ ^3He 54 (430 ppm ^4He)	136
4.35	v and α in $^{***}\text{bcc}$ ^3He 54 (0.53% ^4He) @ 3 MHz	137
4.36	v and α in $^{***}\text{bcc}$ ^3He 54 (0.53% ^4He) @ 9 MHz	138
4.37	v and α in $^{***}\text{bcc}$ ^3He 54 (0.53% ^4He) @ 21 MHz	139
4.38	v and α in hcp ^4He 1 ($17.7 \text{ cm}^3/\text{mole}$) @ 3 MHz	142

Figure		Page
4.39	v and α in hcp ^4He 1 ($17.7 \text{ cm}^3/\text{mole}$) @ 9 MHz	143
4.40	Dislocation fits (3 and 9 MHz) of v and α for hcp ^4He 1	145
4.41	Dislocation fits (3 and 9 MHz) of v and α for $^*\text{hcp } ^4\text{He}$ 7 (10 ppm ^3He)	147
4.42	Dislocation fits (3 and 9 MHz) of v and α for $^{**}\text{hcp } ^4\text{He}$ 8 (105 ppm ^3He)	148
4.43	v and α in $^{***}\text{hcp } ^4\text{He}$ 9 (1400 ppm ^3He) @ 3 MHz	150
4.44	v and α in $^{***}\text{hcp } ^4\text{He}$ 9 (1400 ppm ^3He) @ 9 MHz	151
4.45	Time dependent recovery in hcp ^3He 5 ($18.6 \text{ cm}^3/\text{mole}$)	159
4.46	Time dependent recovery in bcc ^3He 43 ($20.1 \text{ cm}^3/\text{mole}$)	162
4.47	Time dependent recovery in bcc ^3He 45 ($22.3 \text{ cm}^3/\text{mole}$)	163
4.48	Thermal activation of the recovery process in ^3He	165
4.49	Zero sound attenuation in $^{***}\text{hcp } ^3\text{He}$ 17 (0.53% ^4He)	172
5.1	Vacancy activation energies in ^3He	192

CHAPTER 1

INTRODUCTION

Helium is chemically inert with a weak, spherically symmetric interatomic potential. It forms a dielectric solid with a simple cubic or hexagonal symmetry. In view of this simplicity and the accuracy with which the potential is known, solid helium seems to be a model substance in which to compare experimental results to theoretical predictions.

Early experiments showed that, in its thermal and elastic properties, solid helium is similar to more conventional solids. The first theoretical calculations, however, were in quantitative disagreement with the measured values of such properties as the compressibility, molar volume and sound velocities. It was soon realized that the discrepancies were due to the very large zero point motion of the atoms, a result of their small mass and weak interaction. Subsequent work (for a review see, e.g. Glyde (1976)) has taken the quantum effects into account and there now exists sufficient agreement between theory and experiment to make quantitative comparisons possible.

The effects of quantum statistics are most dramatic in the liquid state where ^4He is a Bose fluid undergoing a transition to a superfluid around 2.17 K while ^3He remains a normal Fermi liquid down to a few mK. In the solid, the atoms are more localized, reducing the effects of quantum

statistics. The solid phase diagrams of ^3He and ^4He (shown in figures 1A and 1B) are qualitatively similar but there are quantitative differences as a result of the difference in the magnitude of the zero point motion.

One of the most interesting manifestations of the quantum nature of solid helium is the non-thermal motion of such defects as vacancies and impurities. This results from the overlap of the wave functions of adjacent atoms which permits quantum exchange (or tunneling) of atoms. Due to the periodic potential presented by the lattice, this tunneling may become coherent under certain conditions and allow defects to propagate through the crystal.

Ultrasonic measurements of sound velocities provide direct information about such properties as the elastic constants and the phonon specific heat. Combined with attenuation measurements, the sound velocities can yield information about defects such as dislocations, vacancies and impurities and their interactions.

Solid helium has several experimental advantages over more conventional solids for such ultrasonic studies. First, because of its very low boiling point, it can be obtained free of all but isotopic impurities and these can be reduced to low concentrations (~ 1 ppm). The existence of Fermi and Bose isotopes makes it possible to isolate the effects of statistics while the existence of easily accessible body centered cubic (bcc) and hexagonal close packed (hcp) phases allows the effects of crystal symmetry

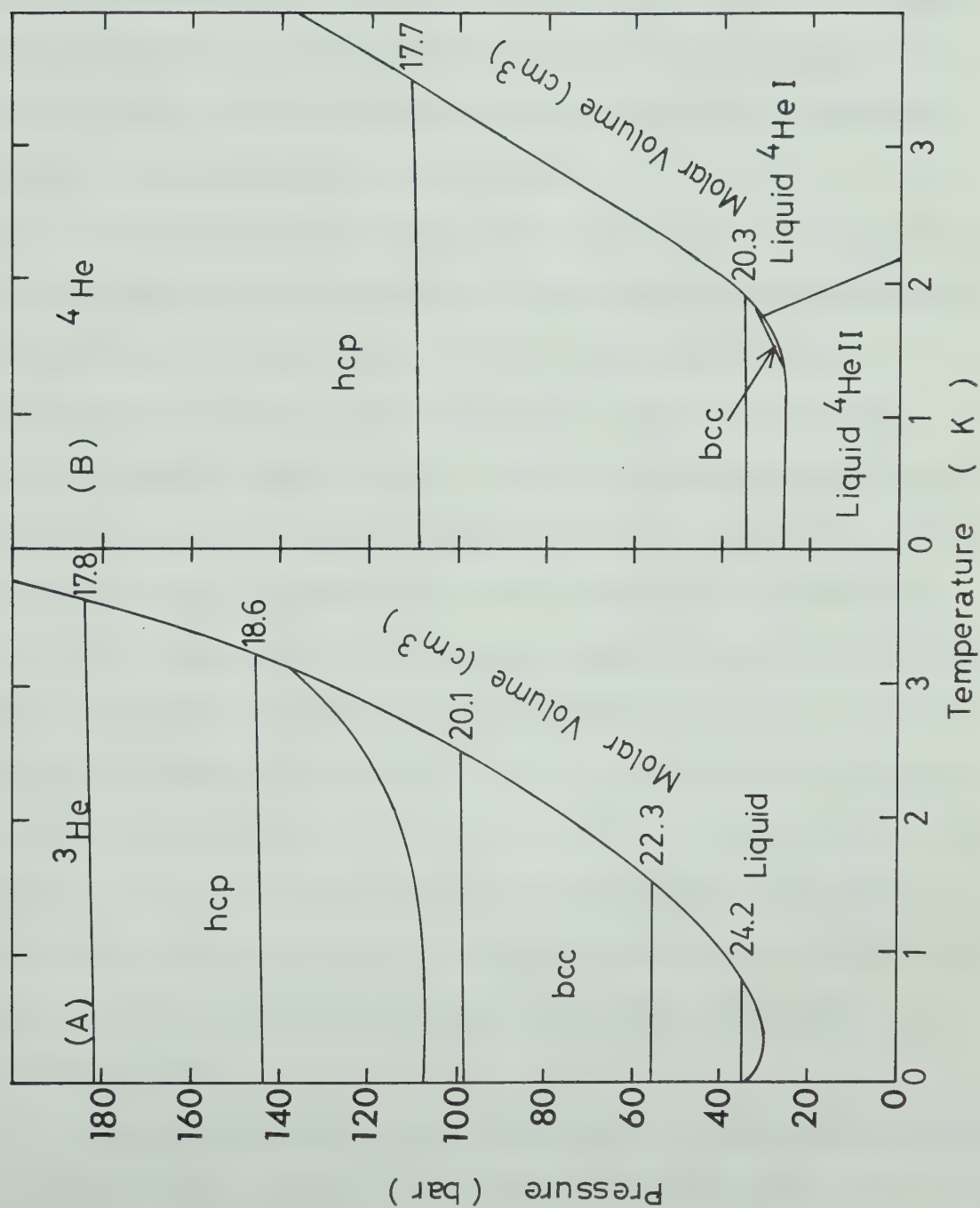


Figure 1.1. Solid phase diagrams of ^3He and ^4He

to be determined. Also, the very large compressibility of helium permits experiments to be performed at constant volume over a wide range of densities. Finally, it is fairly easy to grow the large single crystals needed for ultrasonic studies. The fact that these crystals remain under pressure at all temperatures eliminates spurious effects due to the strains which would be introduced by bonding the crystals to transducers.

Counterbalancing these advantages are the experimental difficulties in generating and maintaining the necessary pressures and temperatures. It is also difficult to control or determine the orientation of the crystals. Another disadvantage is the lack of an independent determination of defect concentrations such as would be available in conventional solids (e.g. from electron microscopy).

The motivation for the experiments described in this thesis was the observation of an anomalous sound velocity and attenuation in pure hcp ^4He ($\lesssim .1$ ppm ^3He) which was not present in impure bcc ^3He ($\lesssim 0.1\%$ ^4He). This anomaly (cf. section 2.4 for a more complete description) has been attributed to interaction between sound waves and dislocations in ^4He but no explanation has been given for its absence in ^3He .

These experiments were intended to determine whether the differences between hcp ^4He and bcc ^3He were due to the differences in isotope, i.e. statistics, in crystallographic phase, or in sample purity. As well, it was hoped that

further evidence to connect the anomaly to crystal dislocations could be obtained and the interactions between the dislocations and other defects studied.

With these aims, crystals of ^4He (hcp) and ^3He (bcc and hcp) were grown and studied at a variety of densities. The longitudinal sound velocity and attenuation were measured between about 80 mK and melting at frequencies between 3 and 21 MHz. The effects of isotopic impurities were investigated by adding up to 0.53% of the other isotope to the initially pure ^3He (1.35 ppm of ^4He) and ^4He ($\lesssim 1$ ppm of ^3He). The effects of pulse amplitude were also studied.

Chapter 2 of this thesis gives some of the theoretical and experimental background to the work. Chapter 3 describes the experimental apparatus and procedures. The experimental results and analysis are presented in Chapter 4 and the final Chapter 5 summarizes and discusses the results.

CHAPTER 2

BACKGROUND

2.1 Lattice Dynamics and Elastic Properties

Propagation of sound in solids is generally described in terms of the linear elasticity equations of a continuous medium. The important quantities in such a description are the displacement from equilibrium of a volume element at position \underline{x} in the i direction, denoted by $u_i(\underline{x})$, the strain tensor

$$\epsilon_{ij} = \frac{1}{2} \left(\frac{\partial u_i}{\partial x_j} + \frac{\partial u_j}{\partial x_i} \right) \quad (2.1-1)$$

and the stress tensor σ_{ij} defined as the force per unit area in the i direction on a surface normal to the j direction. For small strains, the stress is proportional to the strain (Hooke's law) so

$$\sigma_{ij} = C_{ijkl} \epsilon_{kl} \quad (2.1-2)$$

where summation over repeated indices is assumed.

The equation of motion is

$$\rho \ddot{u}_i - \frac{\partial \sigma_{ij}}{\partial x_j} = 0 \quad (2.1-3)$$

or, using (2.1-2)

$$\rho \ddot{u}_i - C_{ijkl} \frac{\partial^2 u_k}{\partial x_j \partial x_l} = 0 \quad (2.1-4)$$

where ρ is the mass density. By assuming solutions of the plane wave form

$$u_k = A_k e^{i(\underline{q} \cdot \underline{x} - \omega t)} \quad (2.1-5)$$

we get the secular equation

$$\det[C_{ijkl} q_j q_l - \rho \omega^2 \delta_{ik}] = 0. \quad (2.1-6)$$

In this description, the coefficients C_{ijkl} which are characteristic of the solid are treated as phenomenological. They can, however, be derived from the microscopic properties of the solid by using lattice dynamics.

The classical picture of a solid at zero temperature is of individual atoms localized at lattice sites. The atoms sit at the minima of the potential wells created by the interatomic potentials of the surrounding atoms. The effect of finite temperatures or elastic strains is to cause displacements of the atoms from their equilibrium positions. If the interparticle potential is known, the elastic and thermal properties of the lattice may be calculated.

For small displacements from equilibrium, the potential energy of the lattice may be written as

$$V = V_0 + \frac{1}{2} \sum_{\underline{\ell}, \underline{\ell}'} \left. \frac{\partial^2 V}{\partial u_i(\underline{\ell}) \partial u_j(\underline{\ell}')} \right|_0 u_i(\underline{\ell}) u_j(\underline{\ell}') \quad (2.1-7)$$

where $u_i(\underline{\ell})$ is the displacement of the atom at position $\underline{\ell}$ in the direction i . The kinetic energy then is

$$T = \frac{1}{2} \sum_{\underline{\ell}} m \dot{u}_i(\underline{\ell}) \dot{u}_i(\underline{\ell}). \quad (2.1-8)$$

It is then possible to derive from the Lagrange equations of motion (e.g. Musgrave (1970)) the secular equation

$$\det[D_{ij}(\underline{q}) - m\omega^2(\underline{q}) \delta_{ij}] = 0 \quad (2.1-9)$$

where \underline{q} is the wavevector, δ the Kronecker delta and

$$D_{ij}(\underline{q}) = \sum_{(\underline{\ell}-\underline{\ell}')} \left. \frac{\partial^2 V}{\partial u_i(\underline{\ell}-\underline{\ell}') \partial u_j(0)} \right|_0 e^{i\underline{q} \cdot (\underline{\ell}-\underline{\ell}')} \quad (2.1-10)$$

In the long wavelength limit (i.e. small \underline{q}), this can be written (Maradudin (1971)) in the form

$$\det[(C_{ijkl} + C'_{ijkl}) q_k q_l - \rho\omega^2 \delta_{ij}] = 0 \quad (2.1-11)$$

where C and C' are complicated functions of the derivatives of $D_{ij}(\underline{q})$. This is identical in form to equation (2.1-6) and shows the connection between elasticity theory and classical lattice dynamics.

Unfortunately, applying classical lattice dynamics to

helium using the well known interatomic potential gives sound velocities four times larger, compressibilities thirty times smaller, and molar volumes smaller by half than those observed experimentally.

The origin of this large discrepancy is the quantum zero point motion which was ignored in the classical calculation. From quantum mechanics, it is known that the perfect localization of atoms at zero temperature in the classical picture cannot be correct since the uncertainty in momentum would then be infinite. For a particle of mass m localized within one lattice spacing a , the kinetic zero point energy can be estimated from the uncertainty principle as

$$E_z = \frac{(\Delta p)^2}{2m} \approx \frac{\hbar^2}{2ma^2} . \quad (2.1-12)$$

If the lattice spacing is increased compared to its classical value, the zero point energy is decreased but the potential energy due to the interparticle potential is increased. The equilibrium lattice spacing in a quantum solid is thus a balance between the repulsion due to the zero point motion and the attraction due to the potential. The small mass and weak attractive potential of helium result in a very large expansion. Associated with the expansion are large increases in the compressibilities and decreases in the sound velocities.

In view of the very large amplitude of the zero

point motion of helium atoms about their mean positions, the harmonic form (2.1-7) is totally inadequate. In fact, calculations using the known potential and lattice spacings (deWette and Nijboer (1965)) show that at low densities the lattice sites are not at minima but rather at local maxima of the potential wells and the calculated phonon frequencies are imaginary. The helium atoms may be visualized as occupying spherical shells about their lattice sites.

In contrast to this unusual microscopic picture of solid helium, experiments show that sound propagates quite normally, albeit slowly, in accordance with equation (2.1-6) and the low temperature specific heat and thermal conductivity indicate that phonons are good excitations. What is needed is a theory of lattice dynamics of quantum solids which takes into account the zero point motion and which describes the propagation of sound in the long wavelength limit.

Considerable progress on such a theory has been made (e.g. Guyer (1969) or Glyde (1976)). The essential features of the theory of quantum solids are very briefly summarized below.

First, it is important to realize that, in their zero point motion, the atoms' positions will be correlated in order to avoid close encounters in which the hard core repulsion is important. These short range correlations may be taken into account (Nosanow (1966)) by assuming the

wave function to be of the form

$$\psi = \prod_i \phi_i(r_i - \ell_i) \prod_{i < j} f(r_i - r_j) \quad (2.1-13)$$

where ϕ_i is the single particle wave function localized at lattice site ℓ_i and f is a Jastrow function describing the short range correlation and could, for example, have the form

$$f(r) = e^{-KV(r)}. \quad (2.1-14)$$

By choosing a plausible Gaussian form for the single particle wave function

$$\phi_i(r) = e^{-Ar_i^2/2} \quad (2.1-15)$$

we can vary K and A to minimize the energy and find

$$E = \frac{\hbar}{4} \sum_{\underline{q}} \omega(\underline{q}) + \sum_{i < j} \langle \Phi | V_{\text{eff}}(r_{ij}) | \Phi \rangle \quad (2.1-16)$$

where

$$\Phi = \prod_i \phi_i(r_i) \quad (2.1-17)$$

and the effective potential is

$$V_{\text{eff}}(r_{ij}) = f^2(r_{ij}) \left[V(r_{ij}) - \frac{\hbar^2 K}{2m} \nabla^2 V(r_{ij}) \right]. \quad (2.1-18)$$

As shown by Fredkin and Werthamer (1965), the phonons may be included with the resulting equation

$$\det[D_{ij}(\underline{q}) - m \omega^2(\underline{q}) \delta_{ij}] = 0, \quad (2.1-19)$$

identical to (2.1-9) except that the dynamical matrix is given by

$$D_{ij}(\underline{q}) = \sum_{\underline{k}, \underline{l}} (e^{i\underline{q} \cdot \underline{r}_{k\ell}} - 1) \langle \Phi | \frac{\partial^2 V_{\text{eff}}(r_{k\ell})}{\partial u_i(\underline{k}) \partial u_j(\underline{l})} | \Phi \rangle. \quad (2.1-20)$$

Thus, in a quantum solid, short range correlations can be included by using an effective potential of the form (2.1-18) while averaging the second derivative of the effective potential over the zero point motion as in (2.1-20) gives the renormalized force constants which give rise to phonons.

With the above in mind, we can use equation (2.1-6) to find the various sound modes in helium, taking the stiffness constants C_{ijkl} from experiments.

The number of independent constants C_{ijkl} can be greatly reduced by using the symmetry of the crystal. The elastic constants are generally written in the Voight notation in which C_{ijkl} is written as a 6×6 matrix by replacing index pairs by single indices according to the

prescription 11→1, 22→2, 33→3, 23 or 32→4, 13 or 31→5, and 12 or 21→6.

For a crystal with hexagonal symmetry, the matrix C_{ij} has 5 independent elements:

$$C_{ij} = \begin{pmatrix} C_{11} & C_{12} & C_{13} & 0 & 0 & 0 \\ C_{12} & C_{11} & C_{13} & 0 & 0 & 0 \\ C_{13} & C_{13} & C_{33} & 0 & 0 & 0 \\ 0 & 0 & 0 & C_{44} & 0 & 0 \\ 0 & 0 & 0 & 0 & C_{44} & 0 \\ 0 & 0 & 0 & 0 & 0 & \frac{1}{2}(C_{11}-C_{12}) \end{pmatrix} \quad (2.1-21)$$

while in a cubic crystal there are only 3 independent elastic constants

$$C_{ij} = \begin{pmatrix} C_{11} & C_{12} & C_{12} & 0 & 0 & 0 \\ C_{12} & C_{11} & C_{12} & 0 & 0 & 0 \\ C_{12} & C_{12} & C_{11} & 0 & 0 & 0 \\ 0 & 0 & 0 & C_{44} & 0 & 0 \\ 0 & 0 & 0 & 0 & C_{44} & 0 \\ 0 & 0 & 0 & 0 & 0 & C_{44} \end{pmatrix} \quad (2.1-22)$$

By solving the secular equation (2.1-6) for the crystal symmetry, the various sound modes can be found. In general there are three sound modes whose polarizations are mutually orthogonal. These do not propagate normal to the wave front but rather at some angle Δ from it.

For hexagonal crystals there is one pure transverse mode, one quasi-transverse mode and one quasi-longitudinal mode. The sound velocities v and the beam deviation angles Δ depend only on the angle θ between the wave normal and the c -axis of the hexagonal crystal.

The velocity of the quasi-longitudinal mode is given by

$$\rho v_L^2 = \frac{1}{2}[c_{11}+c_{44})\sin^2\theta + (c_{33}+c_{44})\cos^2\theta + \phi(\theta)] \quad (2.1-23)$$

where

$$\begin{aligned} \phi^2(\theta) = & (c_{11}-c_{44})^2\sin^4\theta + (c_{33}-c_{44})^2\cos^4\theta + \\ & + 2\sin^2\theta\cos^2\theta[(c_{11}-c_{44})(c_{44}-c_{33})+2(c_{13}+c_{44})^2]. \end{aligned} \quad (2.1-24)$$

Similar expressions give the velocities of the pure transverse mode v_{T1} and the quasi-transverse mode v_{T2} .

Figures 2.1A and 2.1B show the sound velocities and beam deviations, Δ , for hcp ^4He at $17.7 \text{ cm}^3/\text{mole}$ using the elastic constants as calculated by Calder (1977). Note that since v_L depends only on θ , measuring the longitudinal sound velocity allows one to determine θ , although not always uniquely.

For cubic crystals, the sound velocities, polarizations and beam deviations depend on the angles between the

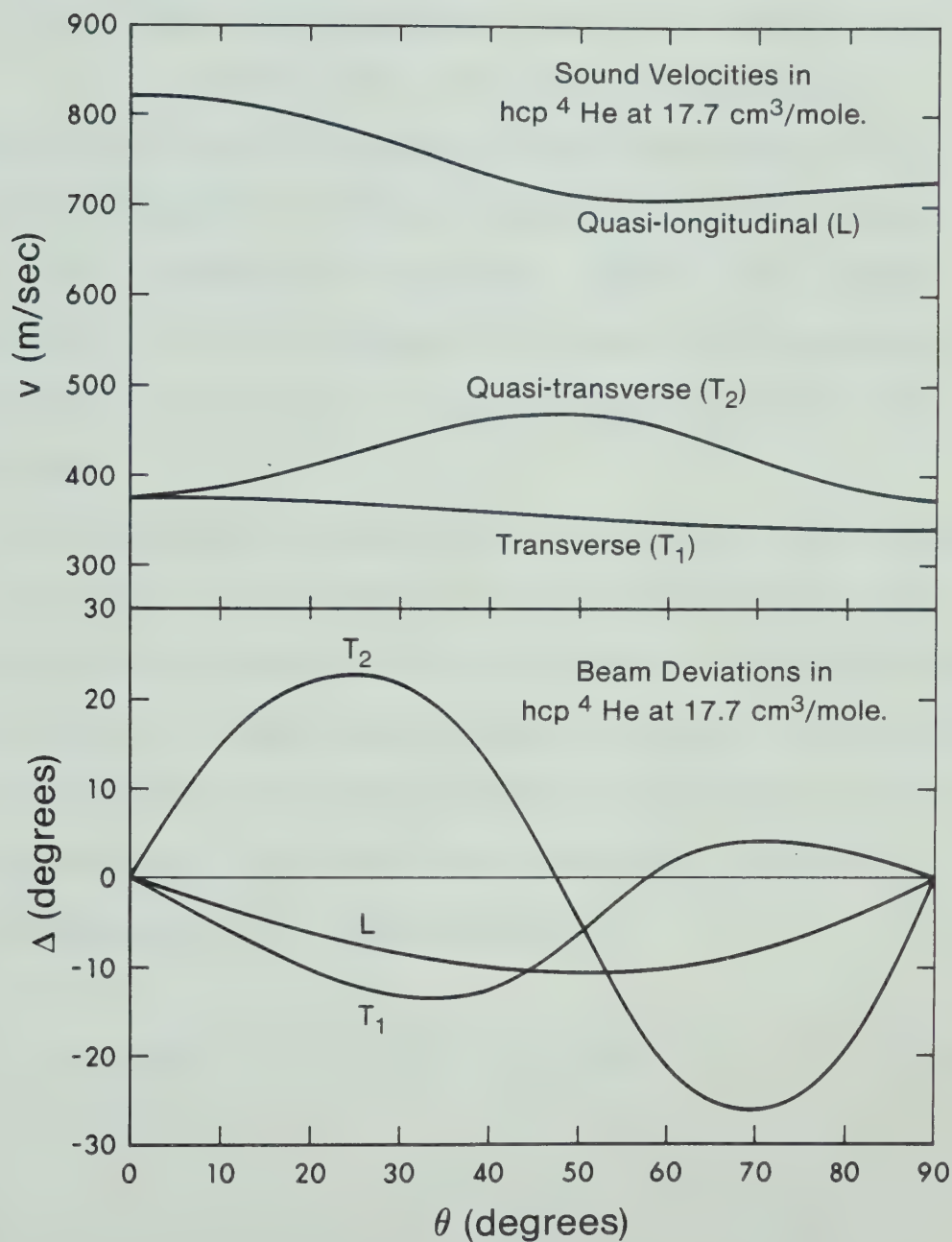


Figure 2.1 Orientation dependence of sound velocities and beam deviations in hcp ^4He at $17.7 \text{ cm}^3/\text{mole}$.

the wave front normal and two crystal axes so that at least two velocities are needed to find the orientation.

2.2 Sound Velocity and Attenuation in an Ideal Solid

In the previous section the sound velocities depended on elastic constants which were essentially phenomenological. At finite temperatures, the thermal motion of the atoms will certainly affect the elastic properties. In this section, the expected temperature dependences of the sound velocity and attenuation are discussed.

A longitudinal wave may be thought of as a periodic density variation in which the compressed regions are heated and the rarefied regions cooled. If the heat Q_1 which flows from the warm to the cool region during one period is much less than the heat Q_2 required to equalize the temperature, then the sound wave will propagate adiabatically. Using the expressions

$$Q_1 = \frac{\kappa \Delta T}{v} \approx \frac{1}{3} \frac{C_V}{V} \cdot \frac{v_D}{v} \cdot v_D \tau_u \Delta T \quad (2.2-1)$$

and

$$Q_2 = \frac{1}{2} \Delta T \cdot \frac{C_P}{V} \cdot \frac{\lambda}{2} \quad (2.2-2)$$

where v_D is the Debye velocity and τ_u is the relaxation

time for resistive phonon scattering processes, the condition for adiabatic propagation is

$$\omega \tau_u \ll \frac{3\pi}{2} \left(\frac{C_P}{C_V} \right) \left(\frac{v}{v_D} \right)^2 \sim 1 \quad (2.2-3)$$

so that sound propagates adiabatically for low frequencies or high temperatures (where τ_u is small).

In the adiabatic regime, the variation with temperature of the attenuation α and the adiabatic velocity v_a come from a mechanism considered by Akhieser (1939). The sound wave strains the medium and, since the thermal phonon frequencies depend on strain, the phonon system is disturbed from equilibrium. The phonon system then irreversibly relaxes to equilibrium via collisions between the thermal phonons. The effect on α due to this mechanism has been calculated (e.g. Bhatia (1967)) as

$$\alpha \approx \frac{\pi}{3} \frac{\gamma^2 C_V T}{\rho V v^2} \cdot \omega \tau_u \quad (2.2-4)$$

where γ is the Grüneisen constant (assumed to be the same for all modes).

For an isotropic material obeying a reduced equation of state, Wanner (1973) has shown that the adiabatic velocity has the form

$$v_a(T) - v_a(0) = \frac{\gamma}{2\rho V v_a(0)} \left(\gamma + 1 - \frac{d \ln \gamma}{d \ln V} \right) [U(T) - U(0)] \quad (2.2-5)$$

where U is the internal energy. At low temperatures where $U(T) - U(0) = AT^4 + BT^6 + \dots$, this reduces to

$$v_a(T) - v_a(0) = aT^4 + bT^6. \quad (2.2-6)$$

As the temperature is lowered, τ_u becomes larger until at some point the condition (2.2-3) for adiabatic propagation is violated. For helium, the relaxation times as determined from thermal conductivities (Hogan (1969), Thomlinson (1972)) are such that $\omega\tau_u \approx 1$ at a temperature between 1 and 2 K for a frequency of 3 MHz. Below this temperature sound propagation is no longer adiabatic and it might be expected that the propagation would become isothermal. However, in order to speak meaningfully of either adiabatic or isothermal sound propagation, the phonon system must be in local equilibrium over regions small compared to the sound wavelength. This means that the phonon mean free path ℓ must be much shorter than the sound wavelength

$$\ell \ll \lambda \quad \text{or} \quad \omega\tau \ll 1 \quad (2.2-7)$$

where τ is the total phonon relaxation time determined from the relaxation times τ_N for momentum conserving (normal) processes and τ_u for resistive (umklapp) processes by

$$\frac{1}{\tau} = \frac{1}{\tau_N} + \frac{1}{\tau_u}. \quad (2.2-8)$$

Thus, for isothermal, as well as for adiabatic sound propagation, it is necessary that

$$\omega\tau_N \ll 1. \quad (2.2-9)$$

The time τ_N can also be found from the thermal conductivity and, for 3 MHz sound, the condition (2.2-9) breaks down at about the same temperature as the condition (2.2-3) for adiabatic propagation. Thus, there is no region of isothermal sound propagation in solid helium at frequencies above a few MHz.

At low temperatures the mean free path of thermal phonons becomes very large and they are said to propagate ballistically. The sound wave is then best regarded as a beam of coherent low energy phonons which are scattered by thermal phonons because of the anharmonicity of the crystal. In this so-called "zero sound" regime, the sound velocity has been calculated (Maris (1971)) as

$$v_z(T) = v_a(T) + \frac{\gamma_{\text{eff}}^2 C_V T}{2\rho V v_a} \quad (2.2-10)$$

where γ_{eff} is a complicated effective Grüneisen constant. The zero sound attenuation was also calculated and found to be of the form

$$\alpha \sim \omega T^4. \quad (2.2-11)$$

Thus at $\omega\tau \sim 1$, there is a transition from zero to adiabatic sound propagation which shifts to lower temperatures (larger τ) as the frequency is decreased. At the transition, the attenuation changes from the T^4 dependence of equation (2.2-11) to the form (2.2-4). In addition, the velocity has a shift given by (2.2-10). The magnitude of the shift is hard to estimate but the zero sound velocity is greater than the adiabatic velocity and approaches it as $T \rightarrow 0$.

In solid helium, it is also possible to propagate a lightly damped phonon density wave or second sound (Ackerman and Overton (1969)). This is not a quantum effect but is rather due to the high purity of solid helium which permits long relaxation times for resistive processes. If this relaxation time is much longer than the period of the oscillation ($\omega\tau_u \gg 1$) then the disturbance can propagate. However, in order for the phonons to be in local equilibrium within one wavelength there must be many normal processes ($\omega\tau_N \ll 1$). Thus, there is a window for second sound propagation given by (Guyer and Krumhansl (1964))

$$\omega\tau_N \ll 1 \ll \omega\tau_u. \quad (2.2-12)$$

If second sound can propagate, it will couple to

first sound, attenuating it and shifting its velocity. However, the window for second sound (2.2-12) is essentially the same for isothermal propagation and does not exist at frequencies above a few MHz.

2.3 Crystal Defects and Sound Propagation

So far, only perfect crystals have been considered. In this section the effects of crystal imperfections on sound propagation are discussed.

Since helium can be highly purified, the only point defects which need to be considered are vacancies and isotopic impurities. Direct X-ray measurements of the number of thermally activated vacancies (Fraas, Heald and Simmons (1977), Heald (1976)) give activation energies W_V in ^3He of between 2.3 K ($V = 24.86 \text{ cm}^3/\text{mole}$) and 21.4 K ($18.8 \text{ cm}^3/\text{mole}$) and vacancy concentrations at melting of about 0.5% (bcc) and 0.1% (hcp). In hcp ^4He ($V = 20.2 \text{ cm}^3/\text{mole}$) the activation energy is 12.7 K with about 0.2% of vacancies at melting.

The vacancies give a significant contribution to the thermal properties of helium, particularly in bcc ^3He at low density (Greywall (1977)) where, near melting, the specific heat due to vacancies is comparable to the lattice specific heat. Therefore, the expression (2.2-5) for the adiabatic velocity should be modified to account for the vacancy energy. Iwasa and Suzuki (1981) have shown that a term proportional to $\int C_{\text{vac}}(T) dT$ should be added to (2.2-6)

where

$$C_{\text{vac}}(T) \sim \left(\frac{W_V}{T} \right)^2 e^{-W_V/T} \quad (2.3-1)$$

is the vacancy specific heat.

The quantum nature of solid helium has important consequences for the mobility of point defects. Due to the large overlap of the wave functions of neighbouring lattice sites, exchange (tunneling) processes are possible. This allows vacancies and impurities to move, even at zero temperature. Various authors (Hetherington (1968) and Mineev (1973)) have considered this process and concluded that the tunneling motion of vacancies or impurities can become coherent at low temperatures and lead to wavelike propagation of the defects. Experimental evidence to support this viewpoint comes from NMR spin diffusion experiments on dilute mixtures of ^3He in ^4He (Mikheev et al. (1977)) in which the mobility of the ^3He impurities increased as the temperature decreased, limited only by impurity-impurity scattering.

The effect of such mobile defects on sound propagation was considered by Meierovich (1975). He found a contribution to the attenuation of the form

$$\alpha \sim N_V(T) \frac{\tau}{1+\tau^2 \omega^2} \quad (2.3-2)$$

where $N_V(T) \sim e^{-W_V/T}$ is the number of thermal vacancies and $\tau \sim T^{-9}$ is the relaxation time. This attenuation increases monotonically with decreasing frequency and goes rapidly to zero at low temperatures as the number of vacancies decreases.

Besides point defects, all real crystals contain dislocations. These are known to make important contributions to the attenuation and velocity of sound, especially in metals (De Batist (1972)).

The effect of dislocations on sound propagation was treated by Granato and Lücke (1956), based on a model due to Koehler (1952). In this model, a dislocation line behaves like a damped vibrating string. The fundamental equation of motion for the transverse displacement $\xi(x)$ of the dislocation is

$$A \frac{\partial^2 \xi}{\partial t^2} + B \frac{\partial \xi}{\partial t} - C \frac{\partial^2 \xi}{\partial x^2} = a\sigma. \quad (2.3-3)$$

The effective mass ($A = \pi \rho a^2$ where a is the Burger's vector) and the effective string tension ($C = 2Ga^2/\pi(1-\nu)$ where G is the shear modulus and ν is Poisson's ratio), result from the energy in the elastic strain field around the dislocation. The damping B comes from interactions between the moving dislocation and thermal phonons and is at low temperatures generally of the form

$$B = gT^n. \quad (2.3-4)$$

The driving force is provided by σ , the shear stress normal to the Burger's vector. The contributions $\Delta\tilde{v}(\ell)$ and $\tilde{\alpha}(\ell)$ to the velocity and attenuation due to a unit density of dislocation loops of length ℓ are

$$\frac{\Delta\tilde{v}(\ell)}{v_0} = \frac{-4v_0^2}{\pi^3} \frac{\omega^2(\ell) - \Omega^2}{[\omega^2(\ell) - \Omega^2]^2 + \left(\frac{B\Omega}{A}\right)^2} \quad (2.3-5)$$

and

$$\tilde{\alpha}(\ell) = \frac{4v_0}{\pi^3} \frac{\Omega^2 B/A}{[\omega^2(\ell) - \Omega^2]^2 + \left(\frac{B\Omega}{A}\right)^2} \quad (2.3-6)$$

where Ω is the sound frequency and

$$\omega(\ell) = \sqrt{\frac{2}{1-v}} \left(\frac{v_T}{\ell} \right) \quad (2.3-7)$$

where v_T is the velocity of transverse sound. The critical loop length ℓ_c which has a resonant frequency Ω is

$$\ell_c = \sqrt{\frac{2}{1-v}} \left(\frac{v_T}{\Omega} \right). \quad (2.3-8)$$

The forms of $\Delta\tilde{v}(\ell)/v$ and $\tilde{\alpha}(\ell)$ are shown in figure 2.2 for various values of the damping B . Note that the loops shorter than ℓ_c reduce the sound velocity while those longer than ℓ_c increase it.

In a real crystal, the dislocations form an irregular

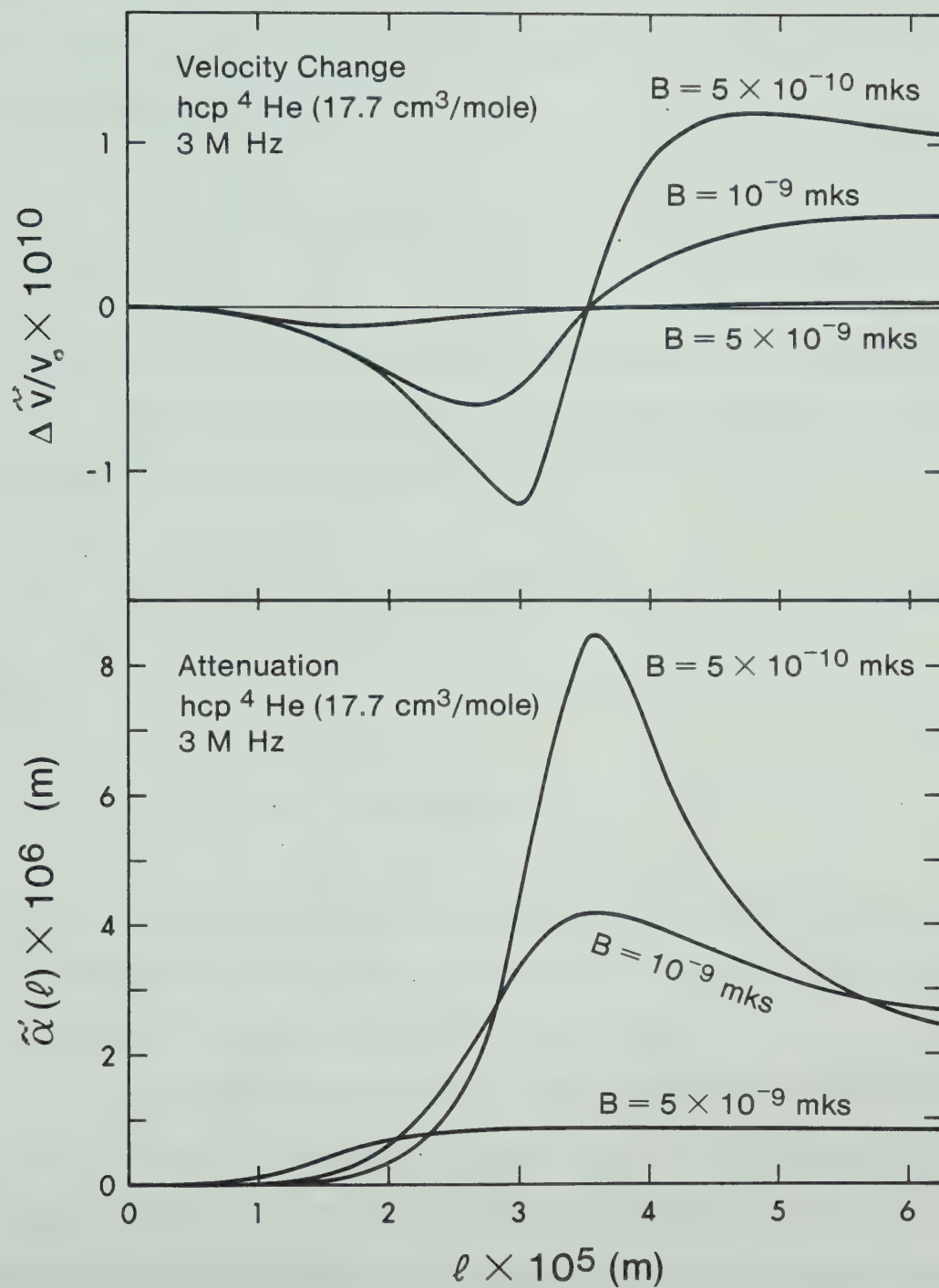


Figure 2.2 Dislocation contributions to velocity and attenuation as a function of loop length.

network with the loops pinned where they intersect. They can also be pinned by impurities which are bound to them and by jogs. The result is a distribution of loop lengths. For the case of pinning by random point defects, the distribution is

$$N(\ell) = \frac{\Lambda}{L^2} \exp \left(-\frac{\ell}{L} \right) \quad (2.3-9)$$

for an average loop length L and dislocation density Λ .

The contribution of all the dislocations to the velocity and attenuation is

$$\frac{\Delta v}{v_0} = R \int \ell N(\ell) \frac{\Delta \tilde{v}(\ell)}{v_0} d\ell \quad (2.3-10)$$

and

$$\alpha = R \int \ell N(\ell) \tilde{\alpha}(\ell) d\ell \quad (2.3-11)$$

where R is an orientation factor which accounts for the fact that only the shear component of the stress normal to the Burger's vector acts on the loop.

The effect of having a continuous distribution of loop lengths is shown in figure 2.3. This shows the contributions $\Delta v(L)$ to the velocity and $\alpha(L)$ to the attenuation due to a unit density of dislocation loops with a length distribution $\sim e^{-\ell/L}$. Comparing figures 2.2 and 2.3, we see that the distribution of loop lengths

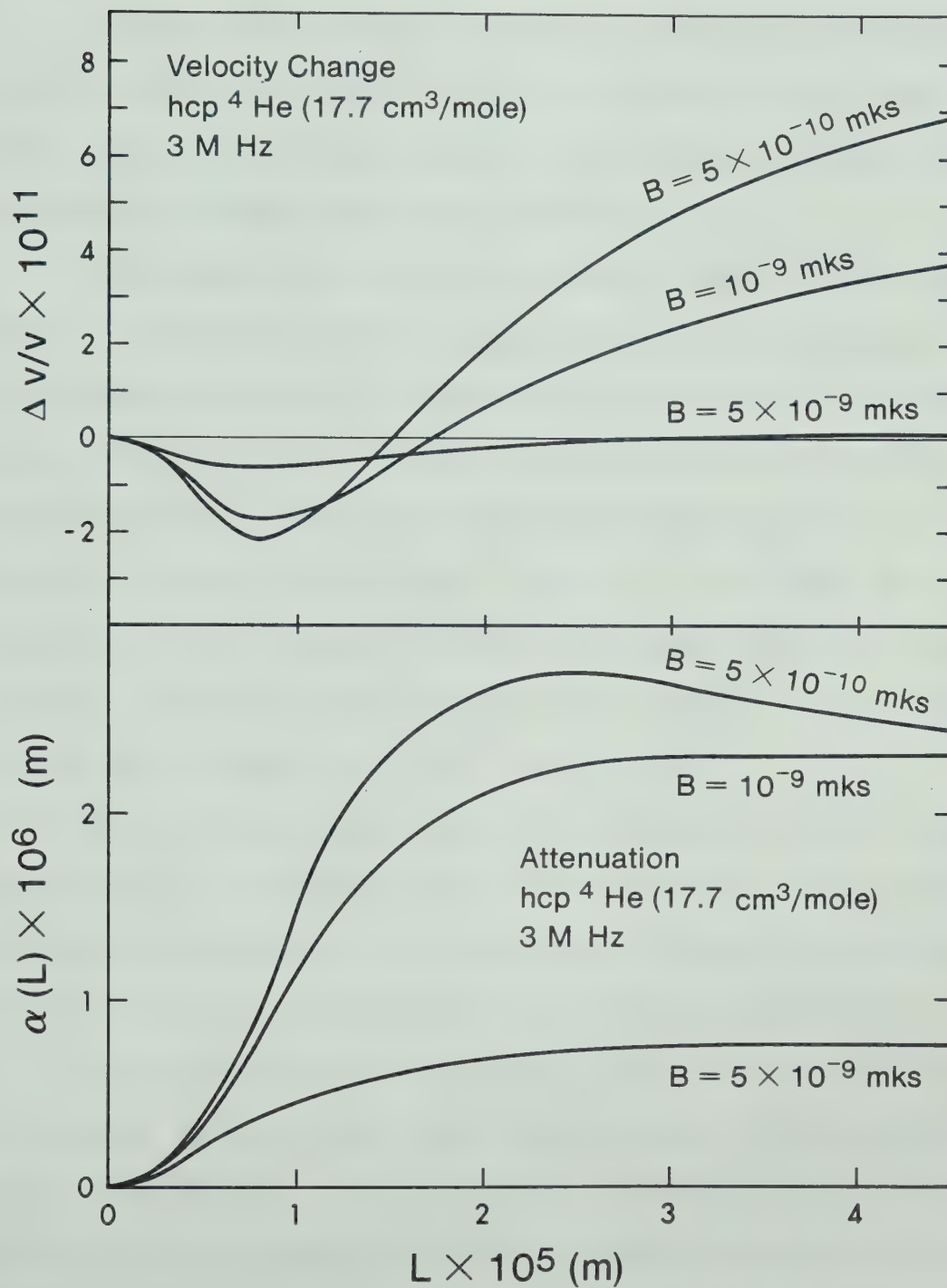


Figure 2.3 Dislocation contributions to velocity and attenuation of a distribution of loop lengths

reduces and smears out the anomaly at low damping and reduces the effective critical length (value of L for which $\Delta v = 0$).

If the slip systems (planes in which the dislocations lie, together with the glide directions in which they move) are known, then R can be calculated from the elastic constants (Henneke and Green (1967)).

Measurements in metals (Nabarro (1967)) indicate that in materials with the hcp structure the dominant slip system consists of dislocations lying in the basal plane, free to glide in the three close packed directions. The orientation factor for the three sound modes is shown in figure 2.4 for hcp ^4He at $17.7 \text{ cm}^3/\text{mole}$ as a function of the angle θ between the wave normal and the c -axis. Note that for longitudinal waves $R \leq 0.13$ for all angles and is zero at $\theta = 0^\circ$ and $\theta = 90^\circ$.

In bcc materials, the slip systems are not so well defined but, in systems with cubic symmetry, the orientation factor is much less anisotropic (Green and Hinton (1966)) and depends on both orientation angles.

The damping coefficient B is due to the interaction of thermal phonons with the dislocations and so increases with temperature. If the thermal phonons scatter off the strain field of the moving dislocation due to the anharmonicity of the lattice, the damping reduces to the form $B \sim T^5$ at low temperatures (Brailsford (1972)). The dislocations can also "flutter" in the stress field of the

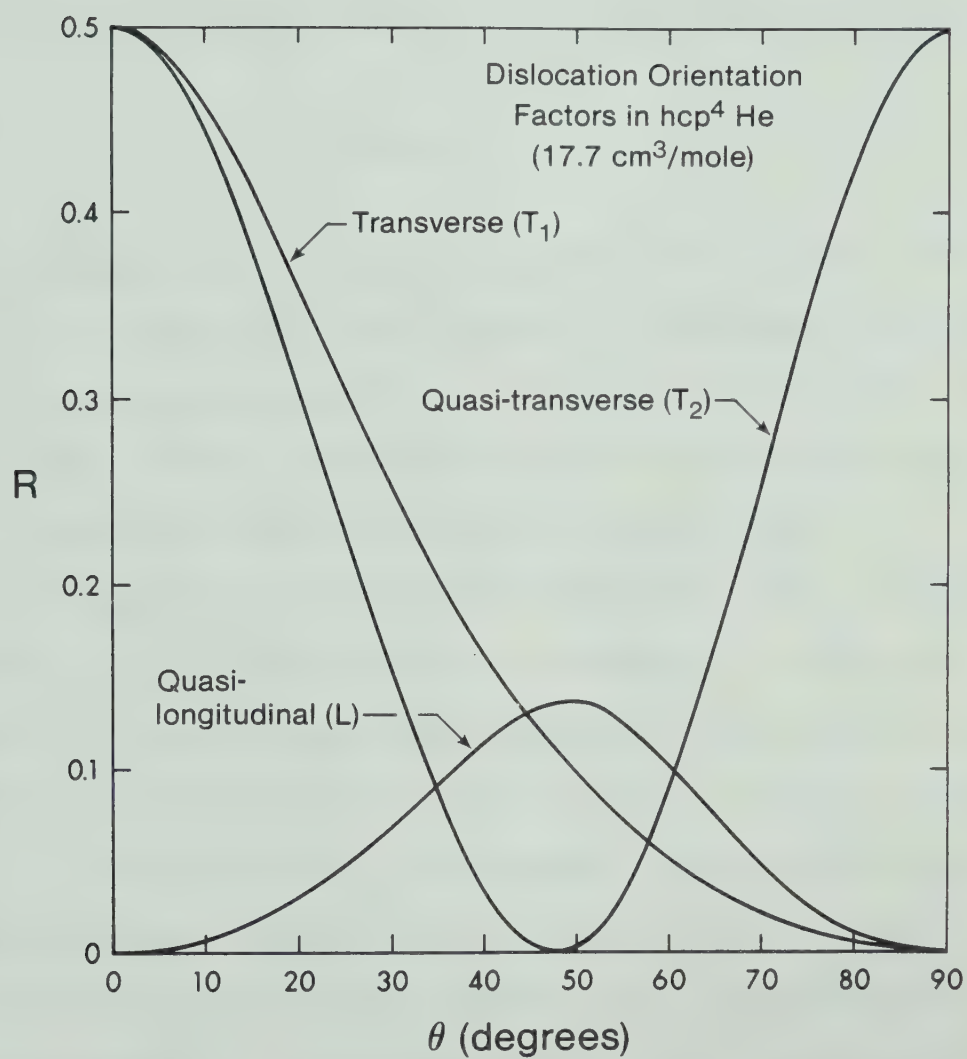


Figure 2.4 Dislocation orientation factors in hcp ⁴He at 17.7 cm³/mole

thermal phonons, radiating energy and giving a low temperature damping $B \sim T^3$ (Ninomiya (1974)).

The temperature dependence of the velocity change and attenuation due to the exponential distribution (2.3-9) of loop lengths is shown in figure 2.5 with the choice $B \sim T^3$ for the damping. The parameter t is defined as

$$t = L/\ell_c. \quad (2.3-13)$$

The parameters B , A and $\omega(\ell)$ in equations (2.3-5) and (2.3-6) are those for hcp ^4He at $17.7 \text{ cm}^3/\text{mole}$. The short loops are more important at high temperatures where the long loops are too strongly damped to have much effect while the long loops become important at low T .

By increasing the sound frequency Ω , the critical length ℓ_c is reduced and so the parameter t increases. The effect of changing the sound frequency while keeping the loop length distribution (2.3-9) fixed is shown in figure 2.6. As the frequency is increased, any negative velocity anomaly changes eventually to a positive one. Further increases in the frequency reduce the amplitude of the positive anomaly. The attenuation, which rises roughly as $\sim \frac{1}{B} \sim T^{-n}$ at high temperatures, eventually levels out at a temperature which is higher for higher frequencies.

2.4 Experimental Results in Solid Helium

The earliest measurements of sound velocities

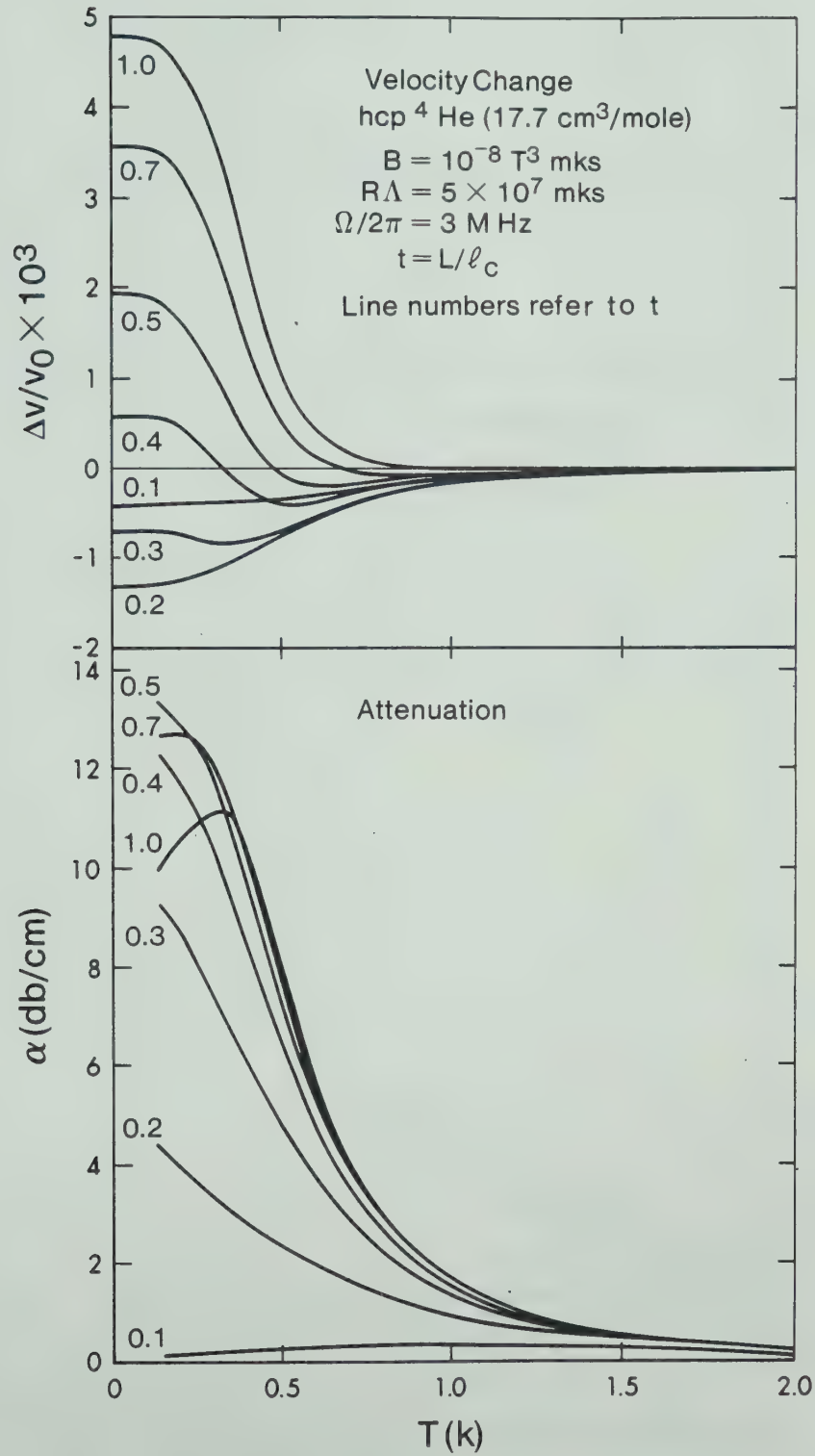


Figure 2.5 Dislocation contributions to velocity and attenuation as functions of temperature

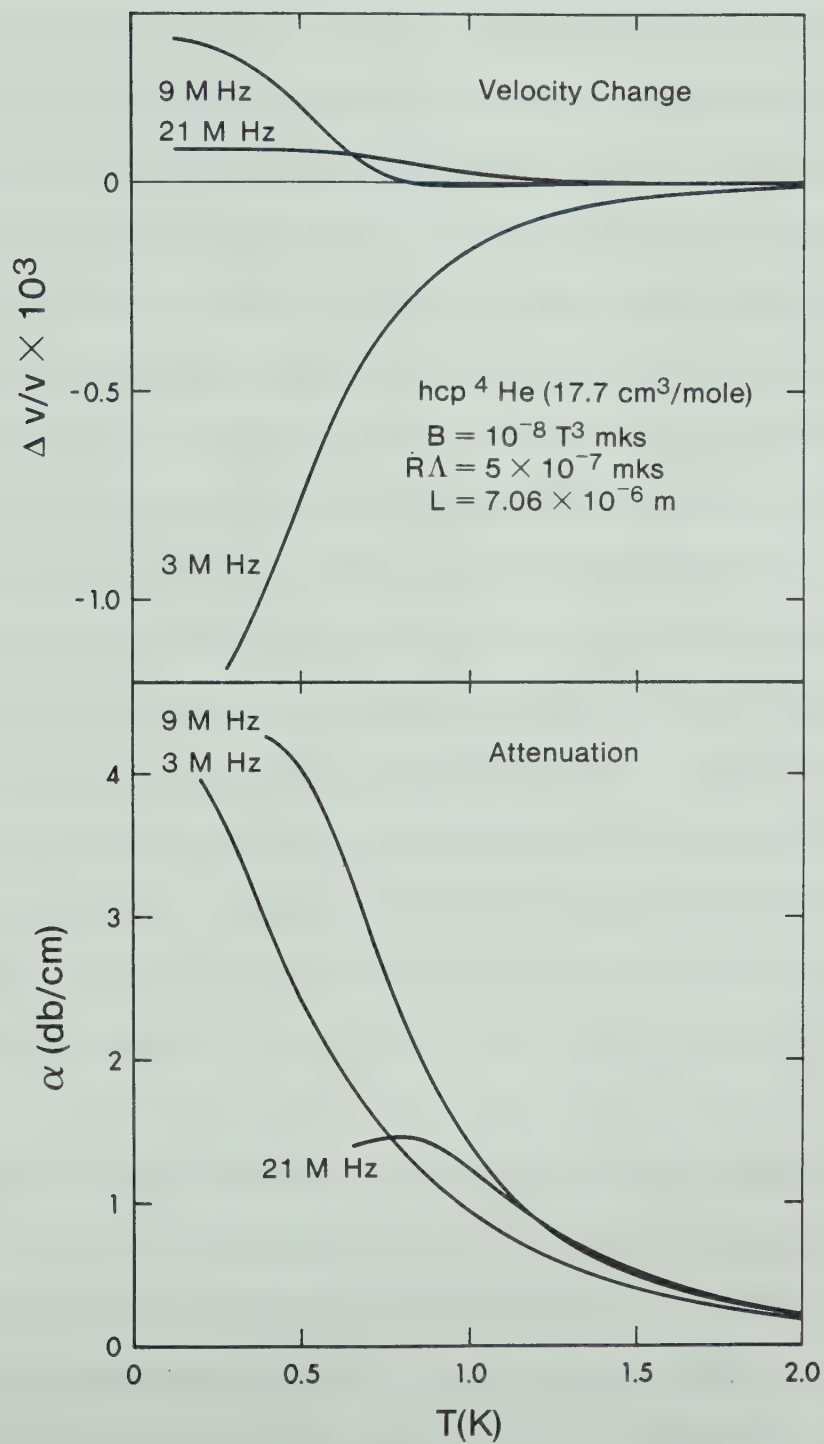


Figure 2.6 Dislocation contributions to velocity and attenuation as functions of Frequency

in solid helium were made by Vignos and Fairbank (1966) (both bcc and hcp, ^3He and ^4He). Their measurements showed a scatter of up to 12% which was interpreted as evidence of anisotropy. Later measurements of sound velocities in single crystals oriented by birefringence methods (hcp ^4He ; Wanner and Franck (1970), Crepeau et al. (1971)) and by X-ray methods (hcp and bcc ^4He , bcc ^3He ; Greywall (1971), (1975), (1976)) have confirmed this and allowed the elastic constants to be determined. In hcp ^3He the elastic constants are unknown but the variation in v observed by Vignos and Fairbank indicates an anisotropy similar to that of hcp ^4He at the same density.

Once the description of sound propagation in terms of elastic constants was established and the molar volume dependence of those constants measured, attention was turned to the temperature dependence of the sound velocity and attenuation. Almost all of the measurements to date have been on hcp ^4He due to the availability of pure ^4He and the existence of the hcp phase over a wide temperature range.

The early measurements of Franck and Hewko (1973) with 5 MHz longitudinal sound in hcp ^4He showed a velocity decreasing with temperature proportional to T^4 , in agreement with equation (2.2-6). However, at about one half of the melting temperature, most crystals showed a "knee" below which v did not change. The attenuation increased rapidly in the knee region. This combination of a

deviation of the sound velocity from the adiabatic form (2.2-6) and an increasing attenuation as the temperature is lowered is referred to as the anomaly.

Later measurements by Wanner, Iwasa and Wales (1976) at 8 and 12 MHz also showed the anomaly in the longitudinal velocity. In their measurements the anomaly took the form of a smooth deviation of the velocity from the adiabatic form. The anomaly was sometimes positive and sometimes negative and had a magnitude $\Delta v/v_0 \leq 3 \times 10^{-3}$. They fitted their data quite successfully with a parameterized form of the Granato-Lücke equation (2.1-11) and found typical dislocation parameters $B = (2-3) \times T^n$ where $n \approx 2$, $L \approx 10^{-3}$ cm and $RA \approx (2-5) \times 10^4$ cm⁻². They also observed an anomaly with transverse sound and found that adding 0.01% ³He suppressed the anomaly.

The longitudinal measurements were later extended to cover a range of frequencies and to include the attenuation.

Calder and Franck (1977) and (1978) and Calder (1977) measured v and α in hcp ⁴He between 5 and 25 MHz. They found the anomaly to be very frequency dependent, with smaller positive velocity anomalies at higher frequencies and attenuation rising down to temperatures of about 0.5 K. The anomaly at 5 MHz was generally positive but in at least one case was negative. In addition, they grew two crystals which showed no anomaly at all.

Iwasa, Araki and Suzuki (1979) performed measurements between 10 and 50 MHz with results similar to those of

Calder and Franck. They were able to fit the velocity anomaly at 10 MHz to the Granato-Lücke equation (2.1-11) using the exponential distribution (2.3-10) of loop lengths. They then found that the velocity at higher frequencies and the attenuation were at least in qualitative agreement with the Granato-Lücke values found from the 10 MHz parameters. Their dislocation parameters were substantially in agreement with those of Wanner et al. (1976). Iwasa and Suzuki (1980) investigated the effect of adding ^3He impurities to their samples. They found that, at low impurity concentrations (30 and 300 ppm), the anomaly was partially suppressed but had an amplitude dependence which could be described by the Granato-Lücke theory of stress induced breakaway from impurity pinning points. The binding energy between a ^3He impurity and a dislocation was estimated as about 0.3 K. At high ^3He concentrations (1%) the attenuation below 1 K was fairly well described by the zero sound form (2.2-11) while the velocity was of the adiabatic form (2.2-6) down to the lowest temperatures (~ 0.1 K).

There have been several other ultrasonic measurements of attenuation in hcp ^4He . Tsuruoka and Hiki (1979) measured the attenuation of longitudinal sound between 5 and 45 MHz near the melting temperature. They interpreted their results in terms of overdamped dislocations but their dislocation densities ($3-6 \times 10^9 \text{ cm}^{-2}$) are very different from those found in other experiments. By using

the sound velocity to orient their crystals they found that the attenuation had an orientation factor of the form shown in figure 2.4, indicating that the glide plane is the basal plane.

Sanders et al. (1977) measured the attenuation during plastic deformation and found that it increased greatly during the first 1% of deformation, a result which could be due to dislocation multiplication during deformation.

Tsymbalenko (1978), (1979) measured the internal friction in hcp ^4He at 15 and 78 KHz. His results were also attributed to overdamped dislocations and the dislocation densities and damping constants agreed reasonably well with those of Wanner et al. (1976) and Iwasa et al. (1979). He found that adding ^3He impurities decreased the internal friction but observed little change when he deformed his samples.

Paalanen et al. (1981) measured the internal friction and shear modulus in hcp ^4He at 330 Hz. They observed very large reductions in the shear modulus which were greatly affected by ^3He concentrations as low as 0.3 ppm. Their results were well described in terms of overdamped dislocations and, using the dislocation parameters obtained, they were able to show agreement with the higher frequency measurements of Tsymbalenko and of Tsuruoka and Hiki. From the amplitude dependence of the internal friction they estimated the energy binding a ^3He atom to a dislocation

as 0.7 K. In ultra pure ^4He (0.0024 ppm ^3He) the damping constant was found to be of the form $B = gT^2$.

Finally, Berberich et al. (1976) measured the attenuation of GHz phonons using stimulated Brillouin scattering and found it to have the zero sound form (2.2-11) over the entire temperature range.

There are far fewer results on sound propagation in ^3He . Other than the early results of Vignos and Fairbank (1966) there have been no measurements in hcp ^3He and the few measurements in bcc ^3He did not show any anomaly.

Wanner et al. (1973) measured the temperature dependence of the sound velocity at 10 and 12 MHz in bcc ^3He ($\leq 0.1\%$ ^4He) at $24.1 \text{ cm}^3/\text{mole}$ down to 123 mK. They were able to observe the longitudinal and both transverse modes but found no anomaly. The velocities were of the form (2.2-6) with large T^6 terms.

Iwasa and Suzuki (1981) made similar measurements of longitudinal velocities in bcc ^3He ($24.4 \text{ cm}^3/\text{mole}$) between 10 and 50 MHz also without seeing an anomaly. They interpreted the large T^6 term as being due to vacancies and were able to fit the velocity by using a term of the form (2.3-1).

Iwasa et al. (1981) observed an increase in attenuation in impure bcc ^3He (480 to 1600 ppm of ^3He) below the isotopic phase separation temperature which they attributed to dislocation multiplication during the phase separation. They also concluded that dislocations are

pinned by the Peierls potential in bcc ^3He .

The experiments reported in this thesis were intended to duplicate in ^3He as closely as possible the conditions of the ultrasonic experiments in hcp ^4He . To do this, pure ^3He was used (1.35 ppm ^4He) and crystals were grown in the hcp phase. In addition, bcc ^3He crystals were studied and the effect of impurities (^4He) was investigated. Finally, hcp ^4He crystals were grown with varying amounts of ^3He to provide a comparison to previous work on hcp ^4He .

CHAPTER 3

EXPERIMENT

3.1 Experimental Apparatus

In order to perform these experiments, it was necessary to achieve and measure temperatures down to 100 mK, to maintain pressures up to 200 bar and to measure the ultrasonic velocity and attenuation with considerable sensitivity.

3.1-1 Refrigeration

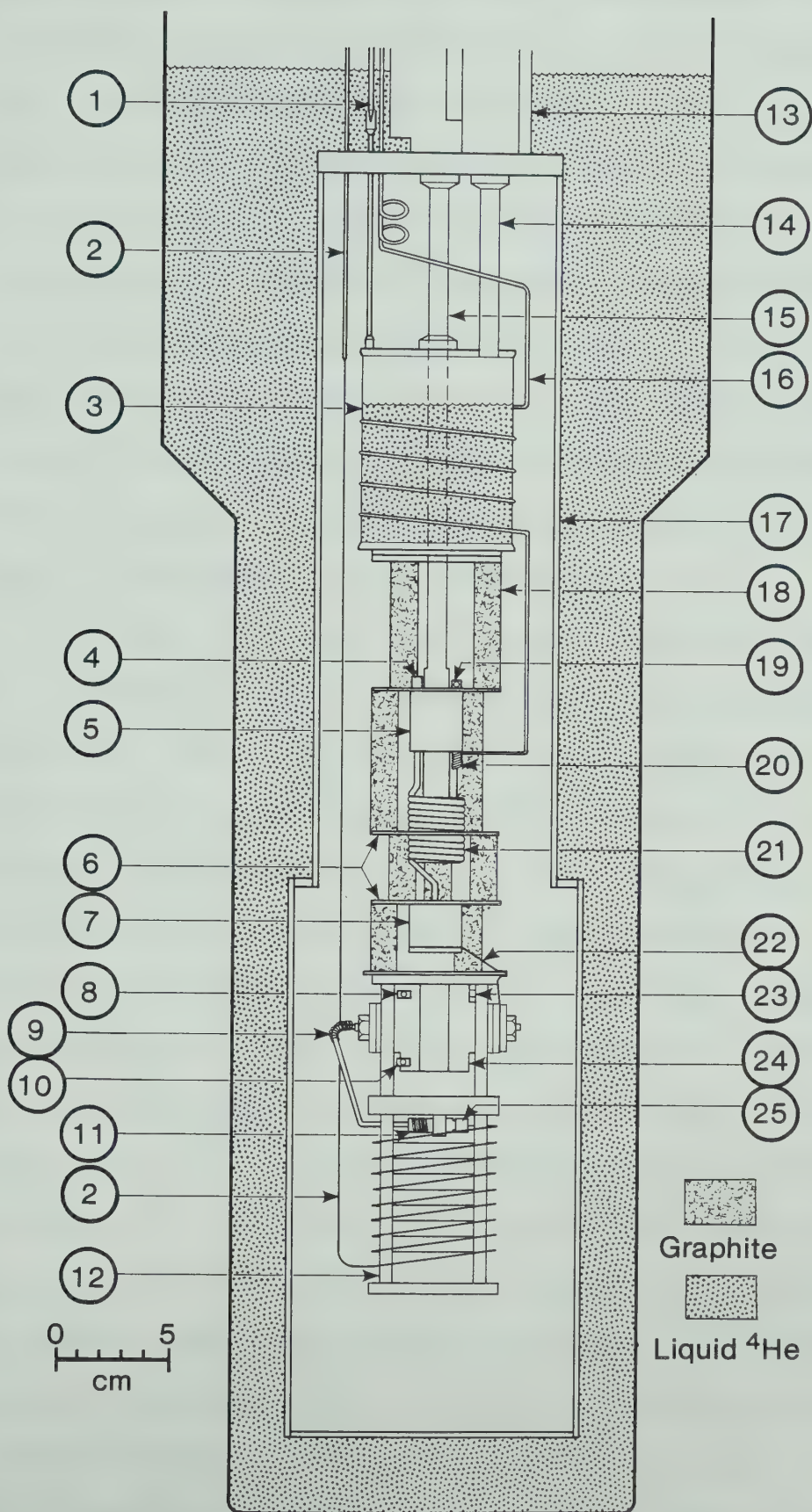
The low temperature portion of the cryostat is shown in figure 3.1. The primary means of cooling was a dilution refrigerator (SHE minifridge). The 1K stage consisted of a ^4He pot with a volume of about 0.4 liters which could be refilled from the main dewar. The ultrasonic cell was thermally coupled to the mixing chamber of the fridge by strips of high purity copper clamped tightly to the mixing chamber and to one end of the cell. The cell was supported by a graphite column hung from the ^4He pot. This support column had several copper rings which were thermally anchored to the still, the heat exchanger and the mixing chamber.

When tested without the sound cell, the fridge reached about 50 mK, near the limit of 40 mK quoted by the manufacturer, indicating that heat leaks due to the support column and thermometer leads were less than about 1 μW .

Figure 3.1

Cryostat

1. ^4He pot needle valve
2. Pressure line (capillary)
3. ^4He pot
4. Still heater
5. Still
6. Copper rings
7. Mixing chamber
8. Calibrated Germanium thermometer
9. Pressure line heater
10. Temperature controller thermometer
11. Capillary heater
12. Capillary support
13. Vacuum can pumping line
14. ^4He pot pumping line
15. Dilution fridge pumping line
16. ^3He return line
17. Vacuum can
18. Graphite support column
19. Still thermometer
20. Flow limiting capillary
21. Heat exchanger
22. Thermal link (copper foil)
23. Cell heater
24. Ultrasonic cell
25. Electrically insulating pressure line coupling



With the cell in place the lowest temperatures reached were about 65 mK, indicating an extra heat leak of about 3 μ W. Most of this was probably due to the stainless steel pressure capillary which entered the vacuum can at 4K. This leak was reduced as much as possible by making the capillary as small (0.3 mm outer diameter with a 0.1 mm i.d.) and as long as possible (about 3 m long, coiled below the cell for compactness). Some heat flowed through the helium in the capillary but no difference was observed between the ultimate temperatures of the cell when it was empty and when it was full.

In fact, the main heat input to the cell came from the ultrasonic signal. Due to inadequate electrical shielding, noise from the ultrasonic electronics was picked up by the thermometers and heaters on the cell, warming it to about 75 mK. Even more significant was the heating due to the rf signal to the transducers. Some of this was converted to sound waves which were attenuated and converted to heat in the helium sample. The rest of the rf energy was converted directly to heat in the coaxial leads to the cell and the electrical feedthroughs in the cell. The amplitude of ultrasonic signal needed depended on the quality of the signal in the sample. Even in samples with strong signals and low attenuation, the minimum input which still allowed an accurate measurement of the velocity and attenuation heated the cell to about 90 mK, indicating a total heat input of about 10 μ W. At

higher ultrasonic frequencies and in crystals with poor signals, the necessary input signal was greater and the limiting temperature correspondingly higher.

The pumping systems are shown schematically in figure 3.2. Due to the relatively small fridge, the pumping requirements for the system were modest. Not shown in figure 3.2 is a Varian 974 partial pressure gauge which was connected to the pot system, the fridge system and the vacuum can system. This was used to monitor ^3He - ^4He ratios in the dilution fridge and to look for leaks in the pumping and pressure systems and was invaluable in diagnosing leaks in the low temperature portion of the cryostat.

3.1-2 Thermometry and Temperature Control

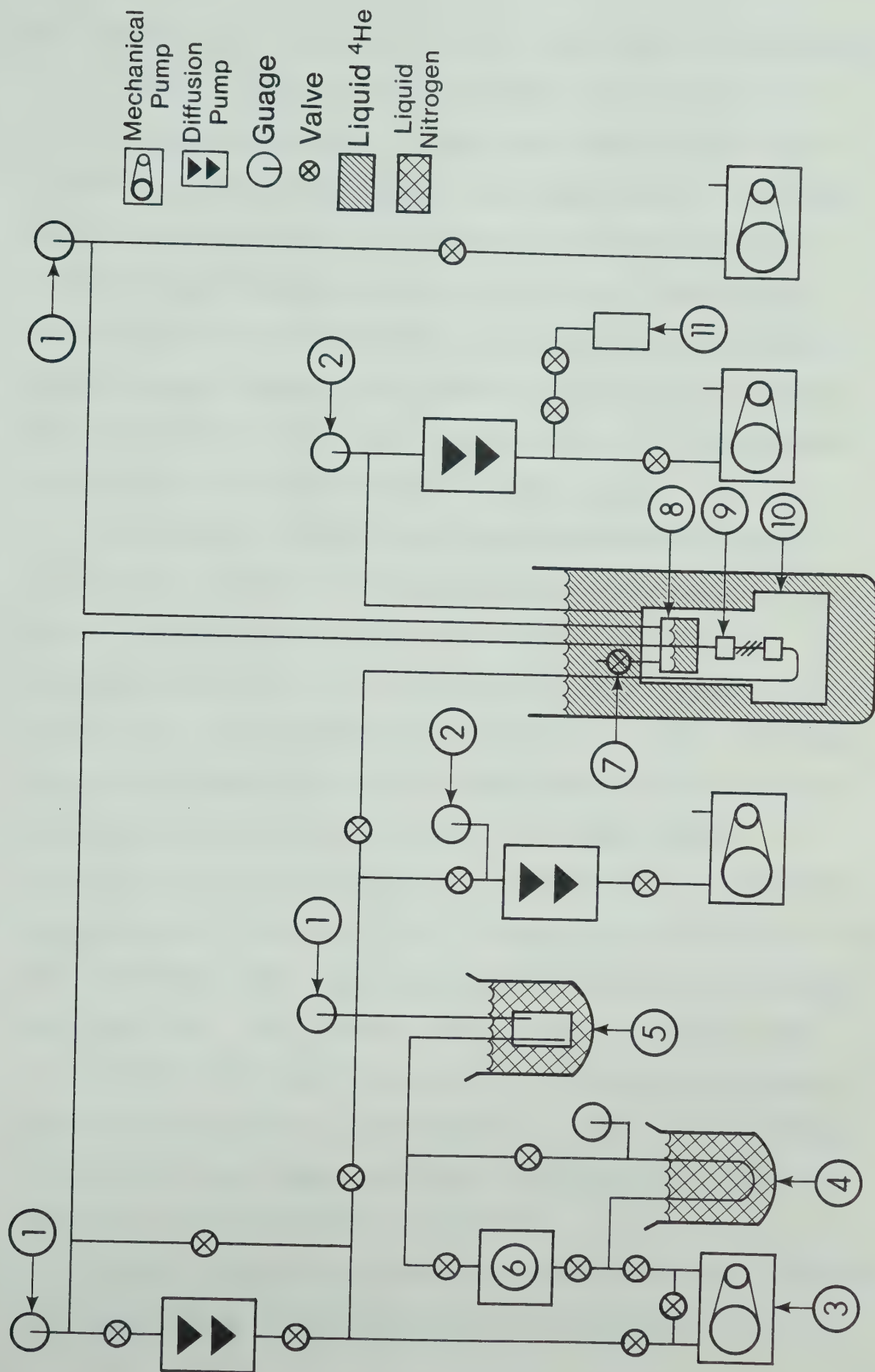
Since the lowest temperatures encountered were around 65 mK, electrical resistance thermometry was adequate and no problems were encountered in making thermal contact to the thermometers. All thermometers were mounted in copper blocks which were clamped to the cell or fridge. Thermal contact was made with Apiezon grease and by varnishing the leads to copper posts screwed into the mounting blocks. All thermometer and heater leads were thermally anchored at the pot, the still, and the heat exchanger to reduce the heat load on the fridge.

Speer carbon resistors (220Ω , 0.5 W) were mounted on the still and on the sound cell and were used primarily

Figure 3.2

Pumping Systems

1. Thermocouple vacuum gauge (0-2000 μ)
2. Cold cathode ionization gauge (10^{-8} - 10^{-4} torr)
3. Sealed mechanical pump
4. Cold trap
5. Molecular sieve cold trap
6. ^3He - ^4He mixture storage
7. ^4He pot fill valve
8. ^4He pot
9. Dilution refrigerator (SHE minifridge)
10. Vacuum can
11. Exchange gas (^4He) storage



for temperature control. For this purpose they were used in a two-wire configuration in the arm of a bridge in which the out of balance signal was amplified and fed to a heater in order to control the temperature. Due to the limited sensitivity of the controller, this method was useful only at temperatures above 0.5 K. Below 0.5 K, temperatures were maintained by manually balancing the heater current against the cooling power of the fridge. The cell heater consisted of about 200 Ω of fine manganin wire wound and varnished onto a brass post.

The primary thermometer for data gathering was a calibrated (30 mK to 5 K) germanium resistance thermometer (Lakeshore Cryogenics GR-200A-30) which had an estimated accuracy of ± 1 mK below 0.5 K and ± 2 mK above 0.5 K. The resistance was measured in a 4-wire configuration by a SHE potentiometric conductance bridge which had an accuracy comparable to that of the thermometer. No change in the resistance of the thermometer was observed after thermal cycling to room temperature and no indication of thermometer self heating or inadequate thermal contact was observed. As a result, the limiting factor in the accuracy of the temperature measurements was the temperature stability during a measurement. For typical heating or cooling rates this contributed an uncertainty of less than 5 mK to the temperature values.

When a continuous record of temperature was required, the output from the SHE bridge was recorded on a chart

recorder.

3.1-3 Pressure System

Since crystals of both bcc and hcp ^3He were to be grown and the effects of density studied, it was necessary to generate and maintain pressures up to 200 bar. The limited amount of ^3He available (about 0.56 moles) meant that the cell and the auxiliary equipment (gauges, valves, etc.) could have little volume. The sound cell, when built, had an internal volume of $2.1 \pm 1 \text{ cm}^3$ and, using this size, a pressure system was designed to generate 200 bar and maintain it during crystal growth. A schematic of this system is shown in figure 3.3.

The valves PV1 to PV7 are HIP 1/16" valves, selected for their small internal volume and their ability to hold up to 1000 bar. The pressure gauge is a Heise bourdon tube gauge (0-200 bar) which was calibrated against a dead weight gauge to an accuracy of $\pm(0.1 \text{ bar} + 0.1\%)$.

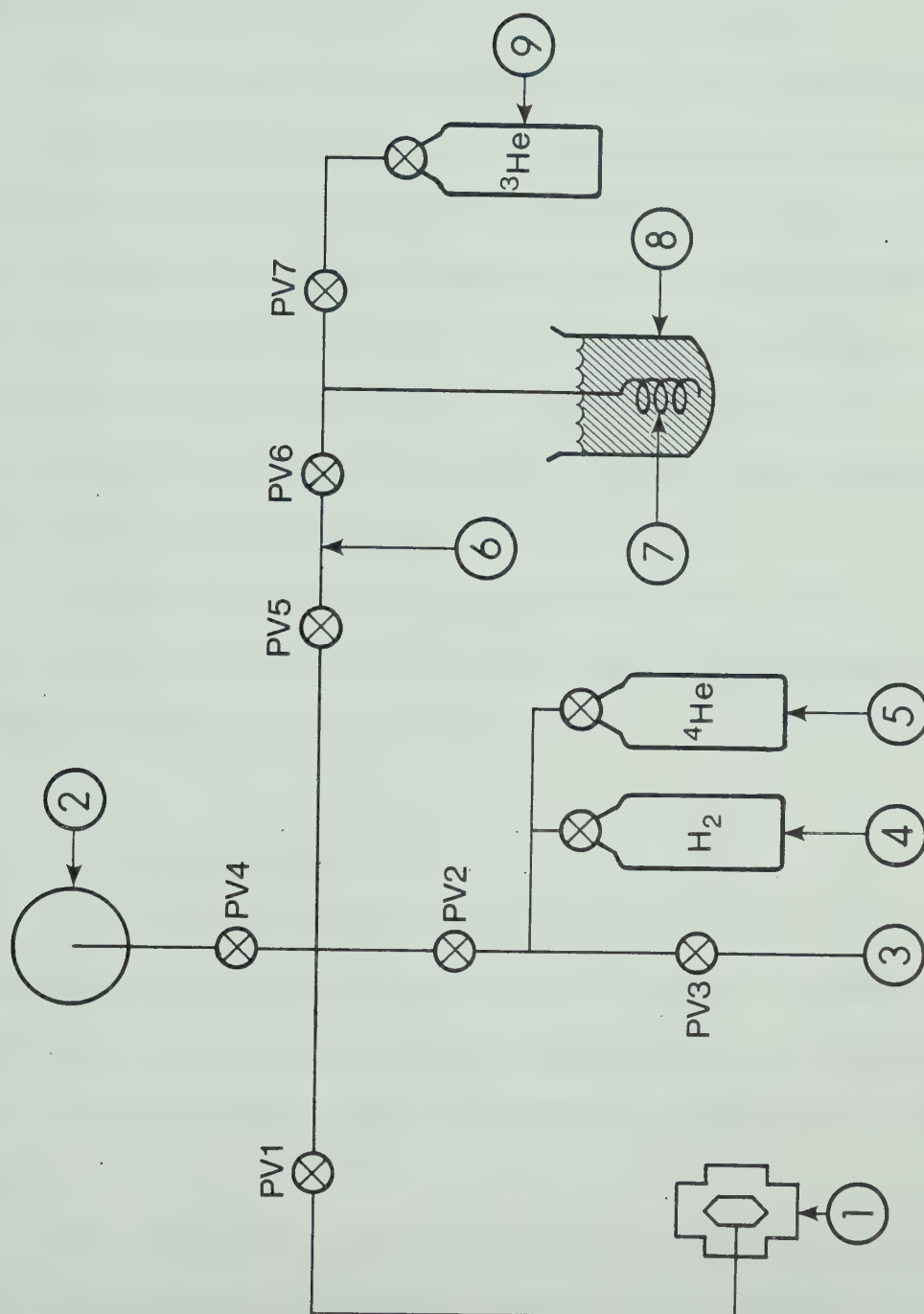
The primary sample of ^3He consisted of 0.56 moles of gas in a cylinder with a volume of 7.9 liters. In order to increase the pressure, the ^3He was condensed into a coil immersed in liquid ^4He . The condensing coil was made from 2.05 m of 1/4" stainless steel tubing giving an internal volume of $24.1 \pm 2 \text{ cm}^3$.

The internal volume of the pressure gauge ($13 \pm 5 \text{ cm}^3$) was used as ballast to keep the pressure in the cell

Figure 3.3

Pressure System

1. Ultrasonic cell
2. Pressure gauge (Heise, 0-200 bar)
3. Two vacuum pumps and partial pressure gauge
4. Hydrogen storage
5. ^4He storage
6. Calibrated volume (0.103 cm^3)
7. ^3He condensing coil
8. Helium dewar
9. Sample gas (^3He) storage



nearly constant during crystal growth. The volume between the valves PV6 and PV5 was measured to be $(0.103 \pm 0.005) \text{ cm}^3$ and was used to add known amounts of gas either to the cell or to the gas sample.

The pressure system also had a line which allowed the system to be pumped out and checked with the partial pressure gauge for impurities before admitting the ^3He . The cylinder of hydrogen shown was for flushing the cell to remove impurities since the size of the capillary prevented rapid evacuation. The ^4He cylinder shown contained ^4He at low pressure (~ 5 bar) and was used to add ^4He to the ^3He sample.

The sound cell was leak tested up to 900 bar, the condenser up to 600 bar and the rest of the system was tested to 200 bar before using it.

3.1-4 Ultrasonic Cell

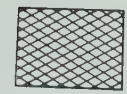
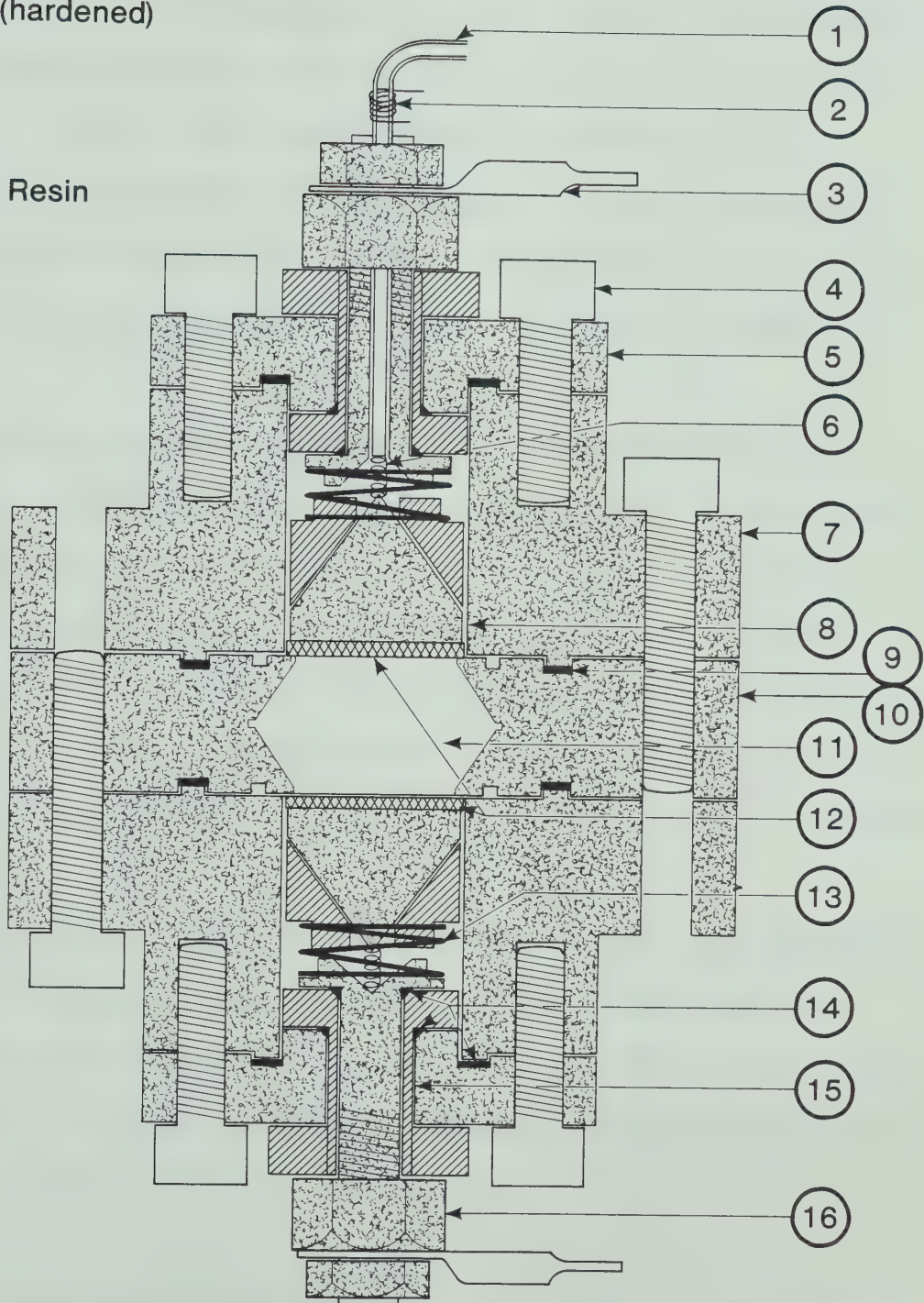
The ultrasonic cell is shown in figure 3.4. It consists basically of two parallel quartz transducers, one used as a pulse generator and the other as a receiver, with the helium crystal contained in the space between them.

For strength, the cell body was made from hardened beryllium copper. The two sides of the central body piece were polished flat and parallel to be used as a spacer for the transducers. The two main body pieces were sealed to the central spacer with an aluminum gasket and

Figure 3.4

Ultrasonic Cell

1. Helium pressure line
2. Pressure line heater
3. Electrical feedthrough connection
4. Stainless steel assembling screw
5. Cell end cap
6. Electrical connector (spring)
7. Cell body
8. Transducer backing piston
9. Aluminum gasket
10. Polished parallel transducer spacer
11. Helium sample space
12. Transducers (3 MHz, X-cut quartz)
13. Transducer retaining ring
14. Indium pressure seals
15. Electrical feedthrough insulation
16. Clamping nut

 Be-Cu (hardened) Quartz Vespel Resin

the end caps were sealed to the body with indium O-rings. The cell was assembled with stainless steel screws.

The two transducers were 1/2", 3 MHz, X-cut quartz transducers, overtone polished and gold plated (Valpey-Fisher). Their front surfaces were supported and electrically grounded by the central spacer. They were backed by polished Be-Cu pistons which were held in place by springs and insulated from the cell body by Vespel jackets.

The electrical feedthroughs through the end caps of the cell were Be-Cu pins, sealed with indium O-rings and insulated by Vespel jackets. In one of the feedthroughs, a hole was drilled and the pressure line was soldered into it. This pressure line was connected to the capillary by an electrically insulating fitting a few inches away. This isolated the electrical feedthrough from the grounded capillary.

In order to prevent the pressure line from freezing during crystal growth, a manganin wire heater (around 100 Ω) was wound around the pressure line where it entered the cell. In addition, the capillary could be heated by passing current directly through it.

3.1-5 Ultrasonic Electronics

A block diagram of the system used to measure the sound velocity and attenuation is shown in figure 3.5. The phase velocity was measured using a modulated pulse

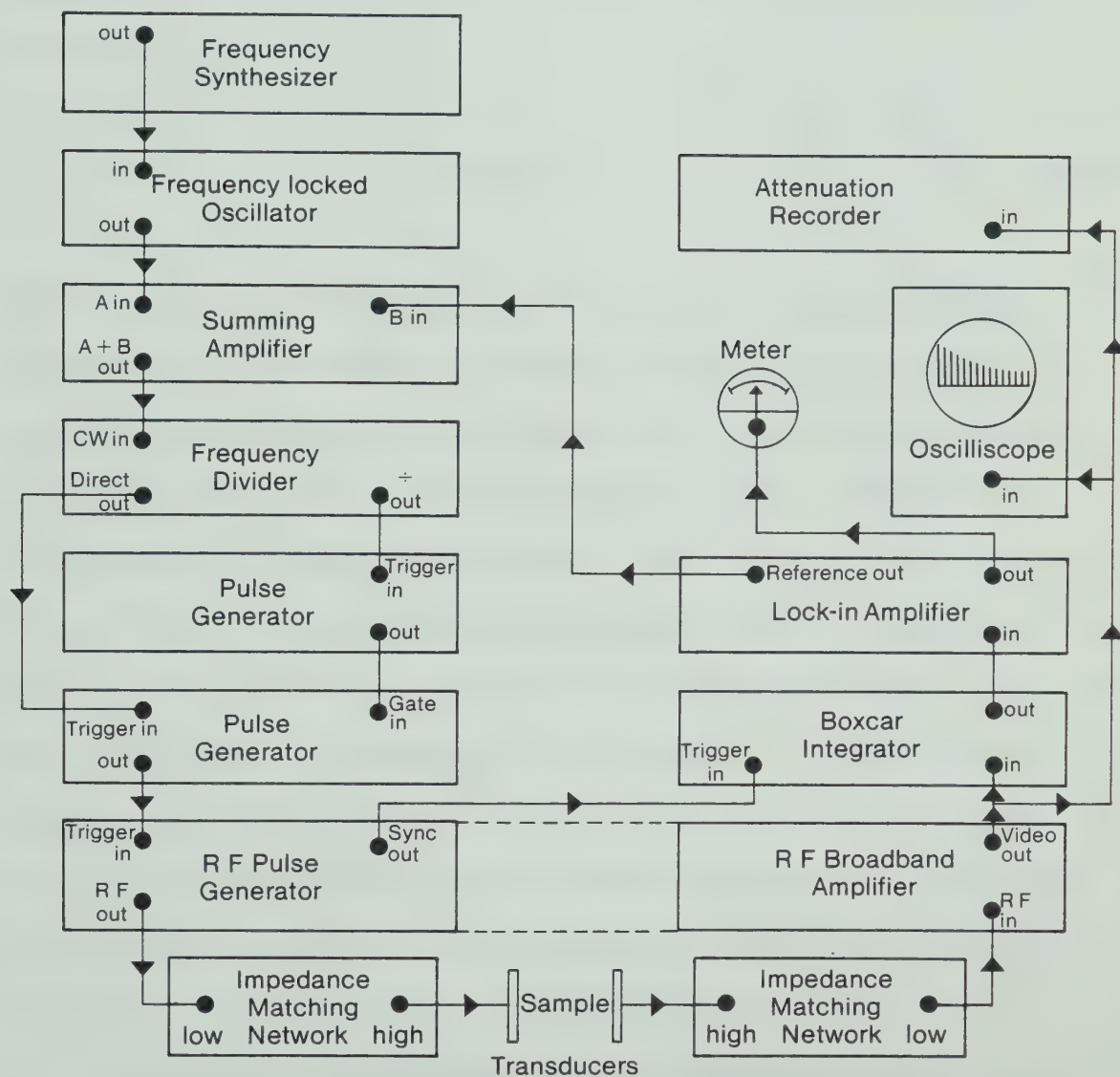


Figure 3.5 Block diagram of ultrasonic electronics

superposition method similar to that described by Holder (1970), and the attenuation was measured by comparing the heights of selected pulses in the echo train.

The phase velocity was determined by measuring the round trip time of a sound pulse in the cell. This is given by

$$\tau = 2D/v \quad (3.1-1)$$

where D is the transducer spacing and v is the sound velocity. If a single rf pulse is excited, a series of echoes is received which decays away due to attenuation in the crystal and to misalignment of the transducers. If a second rf pulse is excited, it either adds to the echo from the first one or subtracts from it depending on whether the rf components of the second pulse and the echo from the first are in or out of phase. If the second pulse is excited a time τ after the first, the first pulse will have just completed one round trip and the echo will be exactly in phase with the second pulse, resulting in a maximum amplitude of the combined signal.

The method for measuring the velocity then is to send widely spaced groups of two or more rf pulses separated by approximately τ and to vary the separation to get the maximum amplitude of ultrasonic signal, corresponding to a separation of exactly τ .

In practice, the value of τ is determined approxi-

mately from the echo train of a single pulse displayed in an oscilloscope. Then the frequency synthesizer (Rockland 5100) is set to a frequency $\nu \approx 1/\tau$. After passing through a frequency locked oscillator (EIC F34) to reduce the noise level, the continuous wave signal of frequency ν is converted to spikes by a decade frequency divider (Matec 122B). The frequency divider also converts the signal to a series of spikes of frequency $\nu \div 100$ or $\nu \div 1000$. The undivided series of spikes (frequency ν) is fed to a pulse generator (HP 8013A) which is equipped with a gate. The frequency divided signal meanwhile is fed to a second pulse generator (HP 222A) and the output pulses from this go to the gate of the first pulse generator. The result is a series of groups, separated by a time $\tau \times 100$ or $\tau \times 1000$, of several pulses separated by a time τ .

These groups of pulses are used to trigger the rf pulse generator (Matec 6600 with a 755 or 760 plug-in) which drives the transducer. The rf pulse generator is tuned to a resonant frequency of the transducer and its output pulses are sent to the transducer through an impedance matching network. The ultrasonic pulses which are excited travel back and forth in the sample. After going through another impedance matching network, the signal from the receiving transducer is amplified (by the combination pulse generator and broadband amplifier) and sent to the oscilloscope.

By adjusting the synthesizer frequency ν , the second pulse and the echo from the first can be brought into phase, resulting in a maximum ultrasonic amplitude. By observing the signal on the oscilloscope the time $\tau = 1/\nu$ can be adjusted to within about one one hundredth of an rf period. For a 3 MHz transducer and a sound velocity of 500 m/sec, this means that τ and hence ν can be measured to about 1 part in 10^4 .

A considerable improvement in sensitivity can be achieved by using a lock-in technique. The amplified and rectified signal from the receiver is fed into a boxcar integrator (PAR CW-1) whose gate is set on the first echo after the two pulses. The pulse separation time τ is modulated by the reference out signal from a lock-in amplifier (PAR HR-8) by adding the modulating signal (at around 300 Hz) to the signal from the frequency synthesizer using a stereo amplifier (Yamaha CA 610 II). This results in a modulation of the pulse separation τ and also of the signal from the boxcar integrator which is then sent to the lock-in amplifier. By adjusting the frequency of the synthesizer, the signal from the lock-in can be zeroed, indicating that the pulses are separated by exactly τ .

The sensitivity of the method depended on the strength of the ultrasonic signal and on the attenuation, but was generally around 1 part in 10^5 . The stability of all the electronics was such that the velocity was reproducible within 3 parts in 10^5 from day to day. The

absolute accuracy of the velocity measurements was limited by the accuracy with which the transducer separation was known and was about $\pm 0.5\%$.

The attenuation was measured with an automatic attenuation recorder (Matec 2470A). This compared the amplitudes of two selected echoes with a sensitivity of about .02 db under optimal conditions. The sensitivity dropped to about 0.1 db when the attenuation was highest. The accuracy of the attenuation measurements, however, was much lower and was limited by several factors.

First, in order to reduce the heat input to the crystal, the pulse amplitude had to be kept low. This meant that the noise level became comparable to the height of the second pulse and affected the attenuation measurements. In practice, if the attenuation was greater than 5 db/cm, the measured values were unreliable.

Secondly, the slight misalignment of the transducers resulted in a non-exponential decay of the pulse amplitude and so the relative heights of successive pulses did not provide an absolute measure of the attenuation. The shape of the echo envelope has been calculated for transducers tilted with respect to each other (Truell et al. (1969)) and for a simply curved reflector (Calder (1978)), allowing corrections to be made for these misalignments. The echo envelope in liquid helium is shown in figure 3.6A and does not resemble the pattern for either tilted or simply curved transducers and is quite different from

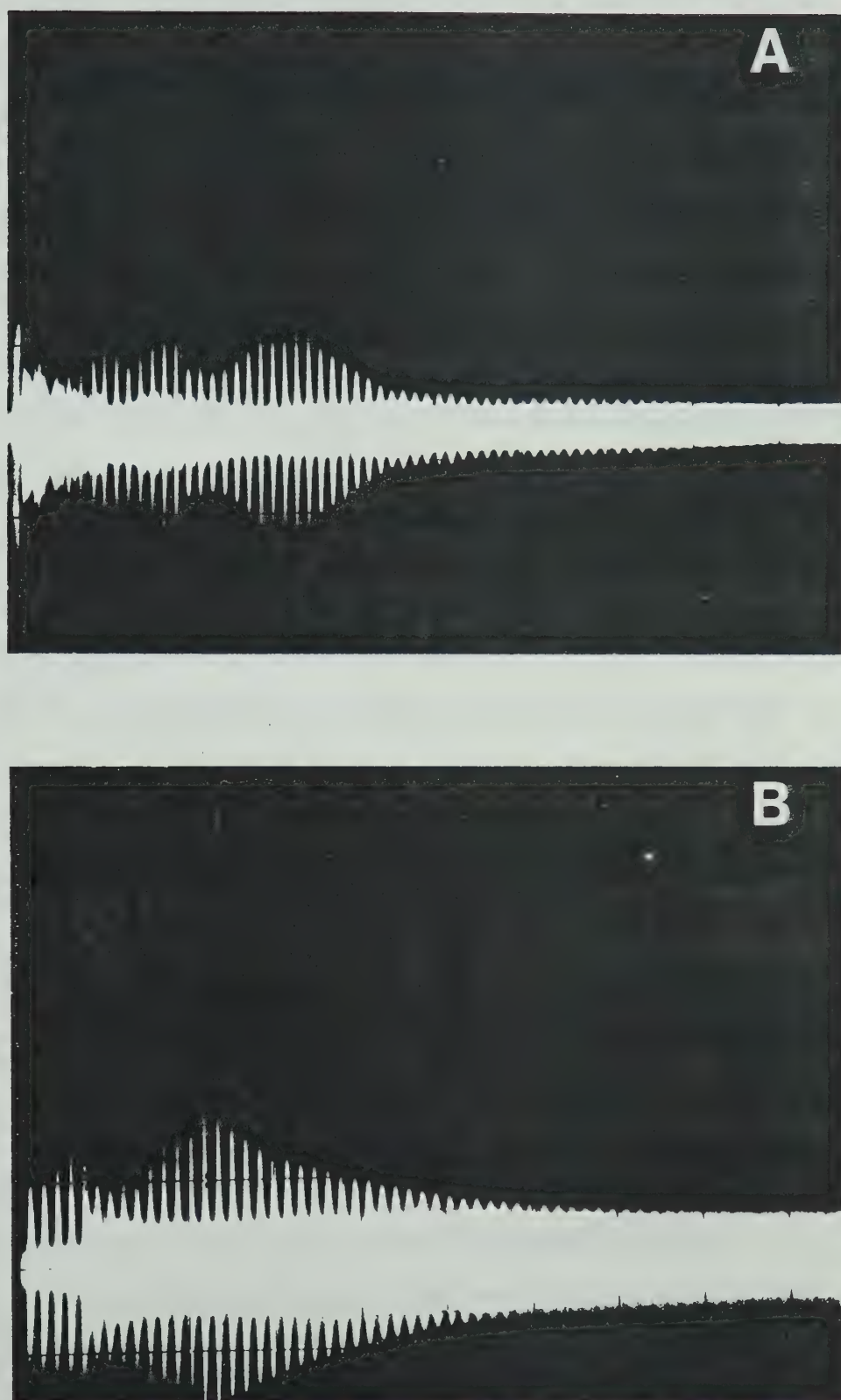


Figure 3.6 Echo Envelopes: (A) Liquid Helium
(B) Solid hcp Helium

the solid echo envelope (figure 3.6B). Also, the echo envelope for solid helium was apparently dependent on whether the pressure capillary blocked as the crystal was growing. It therefore seems that the non-exponential echo envelope resulted from a complicated distortion of the transducers due to the forces exerted by the spring loaded backing piston, the somewhat distorted spacer and the solid helium. Rather than attempt to correct the attenuation values for this distortion, only changes in the relative heights of two echoes were considered. The absolute values of the attenuation could only be estimated but in some crystals near melting as many as 100 echoes were observed, a path length of nearly two meters, indicating attenuation values as low as 0.3 db/cm.

Finally, the misalignment meant that the echo which was superimposed on the second pulse was not perfectly in phase with it over the entire surface of the transducer. This meant that the echo envelope was not quite the same for the double pulse case as for a single pulse. This effect was most noticeable when the envelope was very non-exponential and at higher ultrasonic frequencies when the misalignment was more significant. However, this did not seriously affect the relative measurements.

In order to check the validity of the modulated multiple pulse superposition method, some measurements were repeated using sets of two and of five pulses, and using a single pulse echo overlap method (PEO) as described

by Papadakis (1976). The absolute velocities measured by the three methods agreed within 2 parts in 10^4 and the changes in velocity agreed with each other within the sensitivity of the measurements (5-10 parts in 10^5 for the PEO method). The attenuation values, however, agreed only within about 25% although the sensitivity to attenuation changes was roughly the same in the different methods. For this reason, the attenuation measurements presented in this thesis should be regarded as being relative measurements and of very limited accuracy, particularly at high attenuations and high frequencies.

3.1-6 Sample Gas

The majority of the ^3He crystals were grown from ^3He with a nominal ^4He concentration less than 4 ppm (Monsanto Stable Isotopes). At the conclusion of the experiments, a sample was analysed by the U.S. Bureau of Mines and found to have 1.35 ± 0.05 ppm of ^4He .

Crystals were also grown with varying amounts of ^4He in order to study the effects of impurities. The gas used for this initially had a nominal ^4He concentration less than 0.1%. This gas was also analysed by the U.S. Bureau of Mines and found to contain only 47 ± 5 ppm of ^4He . Crystals grown from this gas are indicated with an asterisk (*) before their number.

By using the calibrated volume (0.103 cm^3) between PV5 and PV6, known amounts of ^4He could be admitted to the

gas sample. Samples were prepared in this way containing ^4He in concentrations of (430 ± 40) ppm (denoted by **) and $(0.53 \pm .05)\%$ (denoted by ***).

The ^4He crystals were grown from Matheson purity ^4He . The ^3He concentration was unknown but probably was ≤ 1 ppm. Known amounts of ^3He were added, resulting in ^3He concentrations of (10 ± 1) ppm (denoted by *), (105 ± 10) ppm (denoted by **) and (1400 ± 140) ppm (denoted by ***).

3.2 Experimental Procedures

This section describes the methods and procedures used in growing helium crystals and in making velocity and attenuation measurements.

3.2-1 Cooling Down

The most important consideration before cooling the cryostat was to thoroughly remove any contaminants, especially ^4He , from the cell. Since the fill capillary was so narrow this involved quite long pumping times. In order to clean the cell out more effectively, it was flushed repeatedly with high purity hydrogen at around 100 bar. The flushing and pumping of the cell and pressure system was repeated about three times and took about 3 days. The cell and pressure system were checked for remaining contaminants using the partial pressure gauge. The cell and pressure system were then pressurized to a few bar with the sample gas. By this time, the vacuum can, fridge

and ^4He pot had been pumped out and cooldown could begin.

A few torr of ^4He was admitted to the vacuum can to act as an exchange gas and liquid nitrogen (LN_2) was siphoned into the main dewar. When the cell had reached LN_2 temperature (in about 4 hours), the nitrogen was removed and replaced with liquid helium. After another 4 hours or so, the cell had reached about 6 K and the exchange gas was pumped out. When the can vacuum reached about 5×10^{-7} torr (after several hours), the pot needle valve, which was submerged in liquid helium, was opened and the ^4He pot filled.

By pumping on the pot, its temperature could be reduced to 1 K in about 1/2 hour. If left to cool, the cell would reach 1 K overnight but if more rapid cooling was desired, some of the ^3He - ^4He mixture could be circulated through the fridge. The cell then cooled to 1 K in about 15 minutes and a limiting temperature of about 0.5 K was reached in an hour or so.

To reach lower temperatures, the ^3He - ^4He mixture was completely condensed into the fridge (a process requiring about 2 hours) and circulation through the fridge begun. About half an hour after the still heater was turned on (to about 2 mW) the cell cooled below 0.5 K and continued cooling until it reached the ultimate temperature determined by the heat input to the cell.

The ^4He pot lasted about 2 days without filling but could be filled without stopping the fridge so that

temperatures below 200 mK could be maintained indefinitely.

3.2-2 Pressurizing and Cooling the Sound Cell

The procedure for increasing the ^3He pressure from its value in the storage cylinder of less than 2 bar to the pressure needed to grow a crystal (between 29 and 200 bar) was as follows. Once the sound cell had been cleaned, the ^3He was allowed into the cell and condensing coil at its storage pressure of about 2 bar. The condenser was then cooled to helium temperature. By pumping on the dewar containing the coil, the coil's temperature could be reduced to 1.6 K. At that temperature the vapour pressure of ^3He is about 0.09 bar and so about 95% of the ^3He sample was condensed into the coil. By shutting the valve PV7 to the storage cylinder and warming the condenser, the desired pressure could be generated. The system proved capable of generating pressures up to 200 bar with no difficulty.

The same system was used with the second ^3He sample (47 ppm of ^4He) which was stored at 30 bar and with ^4He . With these samples it was easier to generate the desired pressure since the necessary amount of gas could be condensed into the coil at 4 K.

Once a crystal had been grown and studied it was necessary to reduce the pressure below the melting pressure in order to grow another. This was done by cooling the condenser to LN_2 temperature and opening the valves PV5

and PV6 to the cell.

The ^3He crystals were grown between 29.6 and 185 bar, corresponding to melting temperatures between 0.48 K and 3.95 K. The cooling was achieved by circulating some of the ^3He - ^4He mixture through the dilution refrigerator. The gas tended to condense at the still at around 1 K and evaporate in the mixing chamber which was warmer. This resulted in undesirable bursts of cooling rather than steady crystal growth. By heating the still with about 1 mW, gas condensation was prevented and steady cooling resulted.

3.2-3 Crystal Growth

Since high quality helium crystals are best grown at constant pressure (Fraass et al. (1977)), that was the method chosen for these experiments. This involved two problems. First, when the helium froze, the pressure dropped and more helium had to be supplied by the pressure system. Secondly, when the crystal was partially grown, the capillary tended to freeze and the crystal would complete its growth isochorically. The crystal growth procedure used was an attempt to solve these problems.

To grow a crystal, the cell was first warmed above the desired melting temperature, T_M , and the pressure reduced below the melting pressure P_M . The fill capillary and the pressure line feedthrough into the cell were heated to prevent blockage and gas was circulated through the

fridge to cool the cell. The cell was allowed to cool nearly to T_M , then the power through the pressure line heater was increased to balance the cooling power of the fridge. By warming the condensing coil of the pressure system with the valves PV5 and PV6 closed, the pressure in the condenser was raised to well above P_M . The valves PV5 and PV6 were cracked to increase the pressure in the cell to P_M . At this point the pressure line heater power was reduced slightly and the cell began to cool slowly (at about 30 mK/min).

When the cell reached T_M , the cooling rate decreased as helium began to freeze. At the same time, the pressure in the cell and ballast volume (provided by the gauge PG1) began to drop slowly. By opening and shutting PV6 and then opening PV5, small amounts of gas from the volume between PV5 and PV6 (0.103 cm^3) could be admitted to the cell and ballast volume. In this manner the pressure in the cell was maintained constant to within 0.2 bar during crystal growth. The slight increase in the cell pressure and the influx of warm gas when the pressure was raised warmed the cell slightly and indicated that the fill line was open.

When the crystal first reached the near transducer, the liquid echoes deteriorated, then disappeared. As the helium froze, the cell temperature dropped slowly as the liquid-solid interface moved through the cell. After about 1 to 2 hours echoes began to appear, indicating that the solid had reached the second transducer.

The echoes grew over a period of about 10 minutes. The space behind the second transducer then froze and the temperature dropped quickly after the cell was completely filled with solid.

Often, especially at pressures greater than 50 bar, the pressure line blocked just before or just after the solid reached the second transducer. If the solid had not yet reached the second transducer, this was indicated by a drop in the temperature of the cell while the pressure measured on PGI remained constant. If the crystal had reached the second transducer, the echo envelope was also observed to deteriorate when the fill line blocked. To free the fill line, the heater power was increased until the temperature suddenly increased and/or the ultrasonic signal changed, indicating that more helium had entered the cell.

The last stage of crystal growth seemed to be the most important in determining the quality of the ultrasonic signal, particularly in hcp crystals. If the fill line blocked after solid echoes were visible, they deteriorated quickly and usually did not recover completely when the fill line was unblocked. If the fill line remained frozen, the signal deteriorated until only a few very small and messy echoes were visible.

In a few cases a solid echo envelope containing several minima was observed just after the crystal reached the second transducer. This pattern was similar to that

expected for transducers tilted with respect to each other and, after the capillary had blocked, the minima moved closer to the first echo, indicating an increase in the tilt angle. In some other cases, the capillary was unblocked after the signal had nearly disappeared and the signal recovered almost to its original form. The quality of the ultrasonic signal therefore did not appear to reflect so much the quality of the crystal as the alignment of the transducers.

The best ultrasonic signals occurred in hcp and high density bcc crystals. Up to 100 echoes were observed near melting with nearly exponential echo envelopes. In bcc ^3He crystals grown at 35.5 bar, the best signals consisted of about 30 echoes. The signal in an hcp ^3He crystal grown at 145 bar is shown in figure 3.6B.

There were also differences in the strengths of the received signals. Some crystals with relatively low attenuation had only very weak signals, making it difficult to make accurate measurements without heating the crystal. This may have been due to problems of bonding to the transducer or due to beam deviations since in anisotropic crystals the ultrasonic beam does not propagate normal to the transducer but rather at an angle (Musgrave (1970)). In helium, which is very anisotropic, the longitudinal sound beam may deviate from the normal by up to 15% (Wanner (1970)). In this sound cell, this would mean that only 75% of the beam would be reflected

by the second transducer, reducing the signal strength.

A total of about 60 bcc ^3He and 20 hcp ^3He crystals were grown. Those with strong ultrasonic signals, an echo envelope indicating good transducer alignment and moderate or low attenuation were studied in detail. At pressures above 50 bar this resulted in a rejection rate of about 50%. At pressures below 50 bar where no problems with capillary blockage were encountered, only about 20% were rejected. A few attempts were made to anneal the crystals near the melting temperature but no improvement in ultrasonic signal was observed.

The low values of attenuation near melting indicated that there was little scattering from defects such as grain boundaries. The signal in each crystal studied consisted of a single set of echoes with a well-defined velocity. In a few crystals there appeared to be two sets of echoes corresponding to different velocities superimposed. The signal in these samples (presumably consisting of a few large crystals) became unstable near melting and the crystals were not studied in detail. The velocities measured at some densities varied from sample to sample by as much as 15%, which is comparable to the range of velocities expected from crystal anisotropy. These observations indicated that the crystals grown were either single crystals or crystals with only small angle grain boundaries.

3.2-4 Ultrasonic Measurements

All of the measurements reported here were made using the methods described in 3.1-5. The number of pulses superimposed, the pulse repetition rate and the input pulse amplitude all varied somewhat but the general procedure is described below.

Once a crystal had been selected for its strong ultrasonic signal, the rf frequency, pulse length and tuning networks were adjusted to give the minimum apparent attenuation. The velocity was then measured using the oscilloscope and 2 to 5 pulses were superimposed to give the maximum amplitude. The pulse amplitude was reduced to the lowest value which allowed reasonable sensitivity, using either the amplitude control on the pulse generator or a 12 db variable attenuator inserted in the output line from the generator. The gate of the boxcar integrator was adjusted to enclose one echo (usually the first echo after the last transmitted pulse) and two echoes were selected for the attenuation recorder (usually the first and second echoes). It was not necessary to adjust any of these settings except when the rf frequency was changed.

The whole tuning procedure could be repeated with the resulting velocity measurement agreeing with the first to within about 1 part in 10^4 . The attenuation measurements were much more sensitive to the tuning, varying by up to 25% for different tuning.

Once the ultrasonics had been tuned, the crystal was cooled and measurements of v and α were taken every 0.1 or 0.2 K. If desired, the crystal could be warmed and cooled repeatedly. The crystals were generally kept at least 0.2 K below melting during measurements.

The amplitude of the pulses could be increased by using the variable attenuator. The attenuator was always returned to its original setting before further measurements were taken as it affected the tuning. Further increases in pulse amplitude involved using the amplitude control on the pulse generator. It too was returned to the original amplitude (within about 1%) before taking measurements.

Once sufficient data had been collected at one frequency, the system was retuned to one of the harmonics (9, 15 or 21 MHz) and the crystal studied at the higher frequency. Most crystals had enough echoes (more than about 5) at 9 MHz to permit measurements but at higher frequencies only a few crystals had good enough signals to be studied.

Once all the desired measurements had been made, the crystal was warmed and melted while measuring the velocity and attenuation. The start of melting was observed as a very sudden increase in the attenuation, accompanied by a change from decreasing to increasing sound velocity. This allowed the melting temperature to be determined within about 10 mK. The values of T_M thus

obtained agreed with the known melting temperatures for each pressure and were used to determine the molar volume.

The onset of melting, as determined both from the ultrasonic properties and from chart records of the temperature as a function of time, occurred suddenly, indicating that no large unannealed pressure gradients were present in the solid.

The transducer spacing in the cell was determined using the known velocity of sound in liquid ^4He (Vignos and Fairbank (1966) and Abraham et al. (1970)). The velocity was measured in liquid ^4He between 23 and 120 bar. The average value obtained for the transducer spacing was 0.933 cm with an estimated uncertainty of 0.5%.

The stress amplitudes in the sound waves could be roughly estimated from the voltage V_p produced by the rf pulse generator and the received signal voltage V_s . At 3 MHz the ratio V_p/V_s was about 10^4 indicating a matching loss of about 40 db at each transducer. Equating the fraction $1/10^4$ of the electrical power which is actually transmitted into the crystal to the acoustic power gives

$$\frac{1}{2} \frac{\sigma^2}{c^2 \rho} = \frac{1}{2} \frac{V_p^2}{R} \div 10^4 \quad (3.2-1)$$

where R is the output impedance of the pulse generator (50 Ω) and σ is the stress amplitude in the sound pulse. At 3 MHz, output voltages were around 8 volts corresponding

to a stress amplitude of about 100 N/m^2 . At higher frequencies, the matching was even poorer and, as a result, the stress amplitudes at 9 and 21 MHz were 20 N/m^2 or less.

CHAPTER 4

EXPERIMENTAL RESULTS AND ANALYSIS

4.1 Introduction

In this chapter, the results of the experiments are presented and analysed in terms of the expected features of sound propagation as discussed in Chapter 2. This introductory section briefly describes the important experimental results and outlines the sequence in which the data are presented.

The first observation to be made is that, when cooled below about one half of the melting temperatures, both hcp and bcc crystals of pure ^3He (1.35 ppm of ^4He) showed an anomaly in the sound velocity and attenuation similar to that previously seen in hcp ^4He . The anomaly took the form of a deviation of the velocity from the adiabatic form

$$v_a(T) - v_a(0) = aT^4 + bT^6, \quad (2.2-6)$$

accompanied by a large increase in attenuation. At the lowest frequency of 3 MHz the velocity deviation was usually negative and the magnitude of the relative deviation $\Delta v/v_0$ varied from less than 10^{-4} to more than 2×10^{-3} . The attenuation at 3 MHz increased down to temperatures below 0.5 K. In crystals with large velocity anomalies, the attenuation was also large, so that in many cases the ultrasonic signal disappeared, making measurements at

temperatures below about 1 K impossible.

At higher frequencies, the character of the anomaly changed somewhat. The velocity anomaly at 9 MHz was generally positive and smaller than the 3 MHz anomaly. The 9 MHz attenuation increased with decreasing temperature, usually reaching a maximum around 0.5 K. In crystals in which measurements could be made at 21 MHz, the velocity anomaly was positive and smaller than that at 3 or 9 MHz while the attenuation usually was lower and had a maximum at a higher temperature.

These features are essentially the same as those previously observed in hcp ^4He (e.g. Calder and Franck (1977), Suzuki et al. (1979)). As a check on the ^3He results, several hcp ^4He crystals were studied and these too showed an anomaly.

In hcp ^3He the magnitude of the anomaly varied by about two orders of magnitude at a given density. Crystals were grown at two densities (18.6 and 17.8 cm³/mole) with crystals at both densities showing anomalies.

In bcc ^3He , most of the crystals were grown at a density of 20.1 cm³/mole. These showed much less variation in the size of the anomaly. Several crystals were studied at lower densities. At 22.3 cm³/mole, the anomalies were considerably smaller and barely within the resolution of the velocity measurements. At 24.2 cm³/mole, no velocity anomaly was observed and the attenuation remained small.

When the ^3He crystals with anomalies were cooled to

below about 300 mK, the attenuation at 3 MHz decreased while the 3 MHz velocity changed. This proved not to be an equilibrium feature of the crystal since the velocity and attenuation upon warming did not agree with their cooling values but rather showed some hysteresis. If the crystal was warmed to near melting and then re-cooled, the original behaviour was repeated, resulting in a reproducible hysteresis on thermal cycling.

The amount of hysteresis depended on the minimum temperature reached (below about 300 mK) and on the length of time the crystal remained at the low temperature. At the high temperature end, the crystal had to be warmed above about one half the melting temperature and held there for some time in order for the original cooling behaviour to be repeated. Both the low and high temperature ends of the hysteresis loop were studied in detail.

The reduction of the attenuation and change in velocity at low temperatures was found to be caused by the sound pulses themselves. The ultrasonic pulses were turned off before cooling the crystal below 300 mK. The crystal was then held at its minimum temperature of about 100 mK for 20 hours. When the crystal was then warmed to above 300 mK before turning the pulses back on, no hysteresis was observed in either the velocity or attenuation. On the other hand, if the ultrasonic pulses were turned on at temperatures below 300 mK, the attenuation immediately began to decrease and the velocity to change. A significant

hysteresis was apparent after only a few minutes of exposure to the pulses. Further study showed that the amount and rate of change of the velocity and attenuation were greater at lower temperatures (below 300 mK), for larger amplitude 3 MHz sound pulses, and for higher pulse repetition rates.

The changes in the velocity and attenuation caused by the 3 MHz pulses could be considerable. In some cases, the anomaly was completely eliminated with the sound velocity approaching the adiabatic velocity while the attenuation decreased from a value so high that no ultrasonic signal was visible ($>>10$ db/cm) to a low value comparable to that near melting (<1 db/cm and up to 100 echoes visible).

No such effect was observed at frequencies of 9 or 21 MHz. At these frequencies, there was no hysteresis even when high amplitude 9 or 21 MHz pulses were applied at the lowest temperatures. However, applying high amplitude 3 MHz pulses at low temperatures did affect the 9 and 21 MHz velocity and attenuation. By measuring v and α at 9 or 21 MHz during cooling, applying high amplitude 3 MHz pulses at low temperature then measuring the 9 or 21 MHz velocity and attenuation during warming, the hysteresis could be studied at higher frequencies. The essential effect of the high amplitude 3 MHz pulses was to change an initially positive velocity anomaly to a smaller but negative one, while reducing the attenuation. By warming

above about one half the melting temperature, the 9 and 21 MHz velocity and attenuation also recovered to their original values.

The region in which v and α recovered was studied. The velocity and attenuation changed with time in this region and the recovery rate increased rapidly with temperature. By measuring this rate as a function of temperature, the recovery process was found to be thermally activated and the activation energy was determined. The activation energies thus found agreed well with those for mobile vacancies as measured by other techniques (Sullivan et al. (1975)).

The anomalous velocity and attenuation during cooling were compared to the predictions of the theory of dislocations as described in section 2.3 and as applied to hcp ^4He by Wanner et al. (1976) and by Iwasa et al. (1979). It proved possible to fit the velocity data quite well. The attenuation predicted using the dislocation parameters from the velocity fits agreed at least qualitatively with the measured attenuation.

The effect of the high amplitude 3 MHz pulses in reducing the anomaly could be accounted for by assuming that the pulses shortened the average lengths of the dislocation lines. The dislocations thus pinned remained so until the crystal was warmed sufficiently for thermally activated vacancies to unpin them.

Since impurities are expected to pin dislocations,

^4He was added to the ^3He in concentrations of 47 ppm, 430 ppm and 0.53%. At 47 and 430 ppm of ^4He , little or no effect was observed. With 0.53% ^4He , the anomaly was completely absent in hcp ^3He and, in bcc ^3He , only a small 3 MHz anomaly remained which was easily eliminated by relatively low amplitude pulses.

Concentrations of 10, 105 and 1400 ppm of ^3He were also added to the ^4He . Similar effects were observed with the anomaly almost completely suppressed by 1400 ppm of ^3He .

In the hcp ^3He crystals with 0.53% ^4He , several interesting features were observed. First, with the anomalous contribution to the velocity and attenuation eliminated, the attenuation from other sources could be studied. The attenuation increased with temperature and with sound frequency and, at low temperatures, was well described by the zero sound formula

$$\alpha \sim \omega T^4. \quad (2.2-11)$$

At low temperatures (below about 1 K), the 3 MHz velocity and attenuation were amplitude dependent in this crystal. As the pulse amplitude was increased, the velocity deviated from the adiabatic form and the attenuation increased. The critical amplitude at which the attenuation started to rise decreased as the temperature was increased. By measuring the critical amplitude as a function of temperature and interpreting the results in terms of stress

induced breakaway from impurity pinning points, the binding energy between ^4He atoms and dislocations in hcp ^3He could be estimated.

A check on the impurity concentration was provided by the observation of the isotopic phase separation in bcc ^3He (0.53% ^4He) at $24.2 \text{ cm}^3/\text{mole}$. The phase separation appeared as an increase in the attenuation at a temperature of about 125 mK.

The experimental results are presented in the following sequence. First, in section 4.2, the results for hcp ^3He are given. The data from the crystal hcp ^3He 5 ($18.6 \text{ cm}^3/\text{mole}$) are shown in detail, including the anomaly on cooling, the hysteresis, the effects of high amplitude 3 MHz pulses and the fits of dislocation theory to the velocity and attenuation anomaly observed during cooling. Then, for comparison, the anomalous velocity and attenuation are shown, together with the dislocation fits, for two more pure hcp ^3He crystals at the same density. Next, the results from an hcp crystal at a higher density ($17.8 \text{ cm}^3/\text{mole}$) are shown. Finally, the results of adding ^4He impurities are presented. At the lower concentrations of 47 and 430 ppm, the impurities have little effect so the anomalies and dislocation fits are shown. At 0.53% ^4He , the low amplitude data are presented, showing no anomaly. The amplitude dependence of the velocity and attenuation is also shown and analysed.

In section 4.3 the results for bcc ^3He are similarly

presented. First, a typical crystal (bcc ^3He 43) is shown in detail. Other crystals at the same density, crystals at lower densities, and finally crystals with ^4He added are then shown.

The results from hcp ^4He are given in section 4.4 for comparison, including the effects of ^3He impurities.

In section 4.5 the adiabatic (high temperature) region is discussed. The coefficients a and b from the high temperature fits are tabulated.

In section 4.6 the thermally activated recovery is studied in detail. The data on the temperature dependence of the recovery rate are shown for one hcp and two bcc ^3He crystals together with the activation energies.

The dislocation parameters from hcp and bcc ^3He and for hcp ^4He are collected in section 4.7.

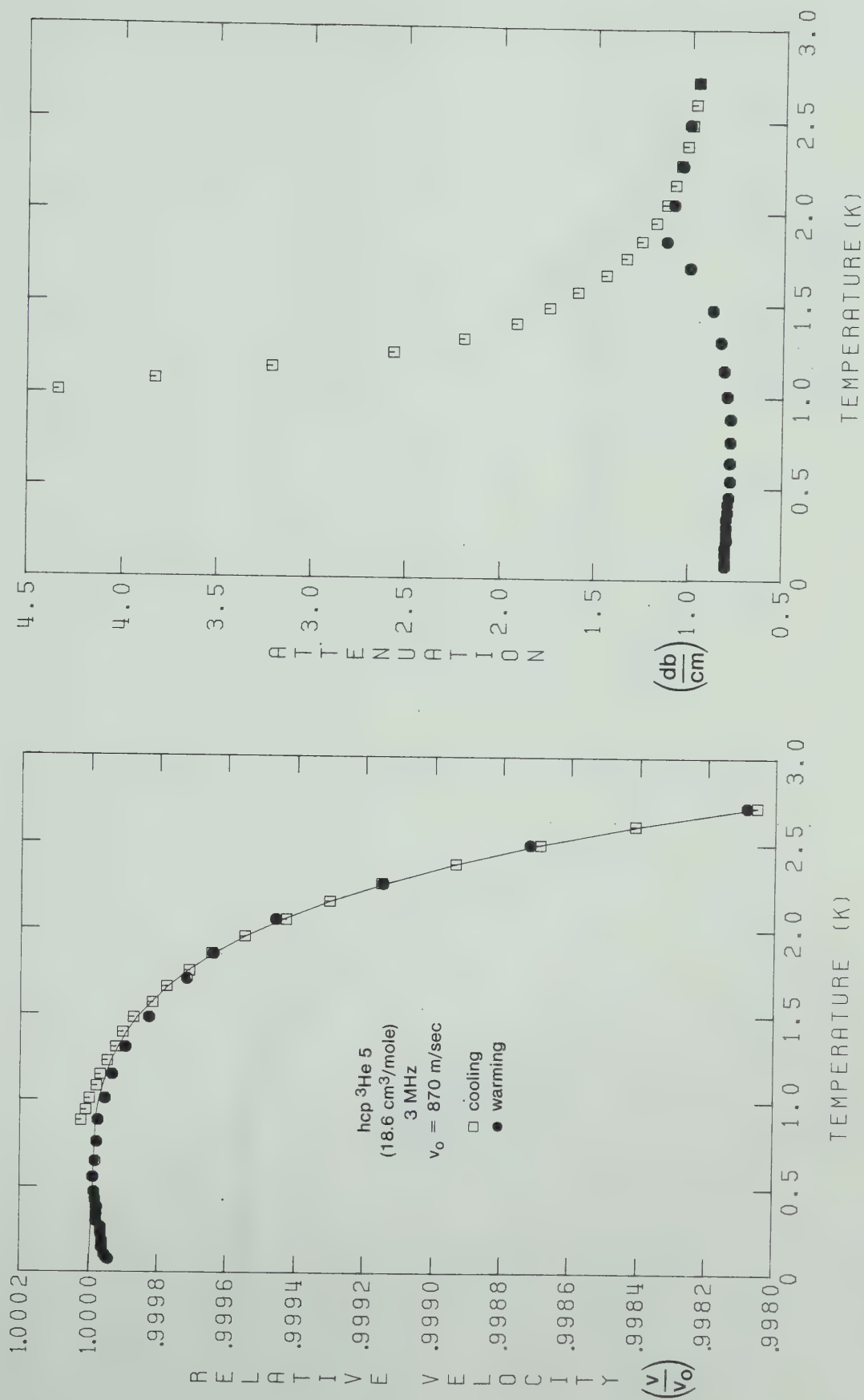
Finally, in section 4.8, the comparison is given between the zero sound predictions and the attenuation in hcp ^3He containing 0.53% ^4He .

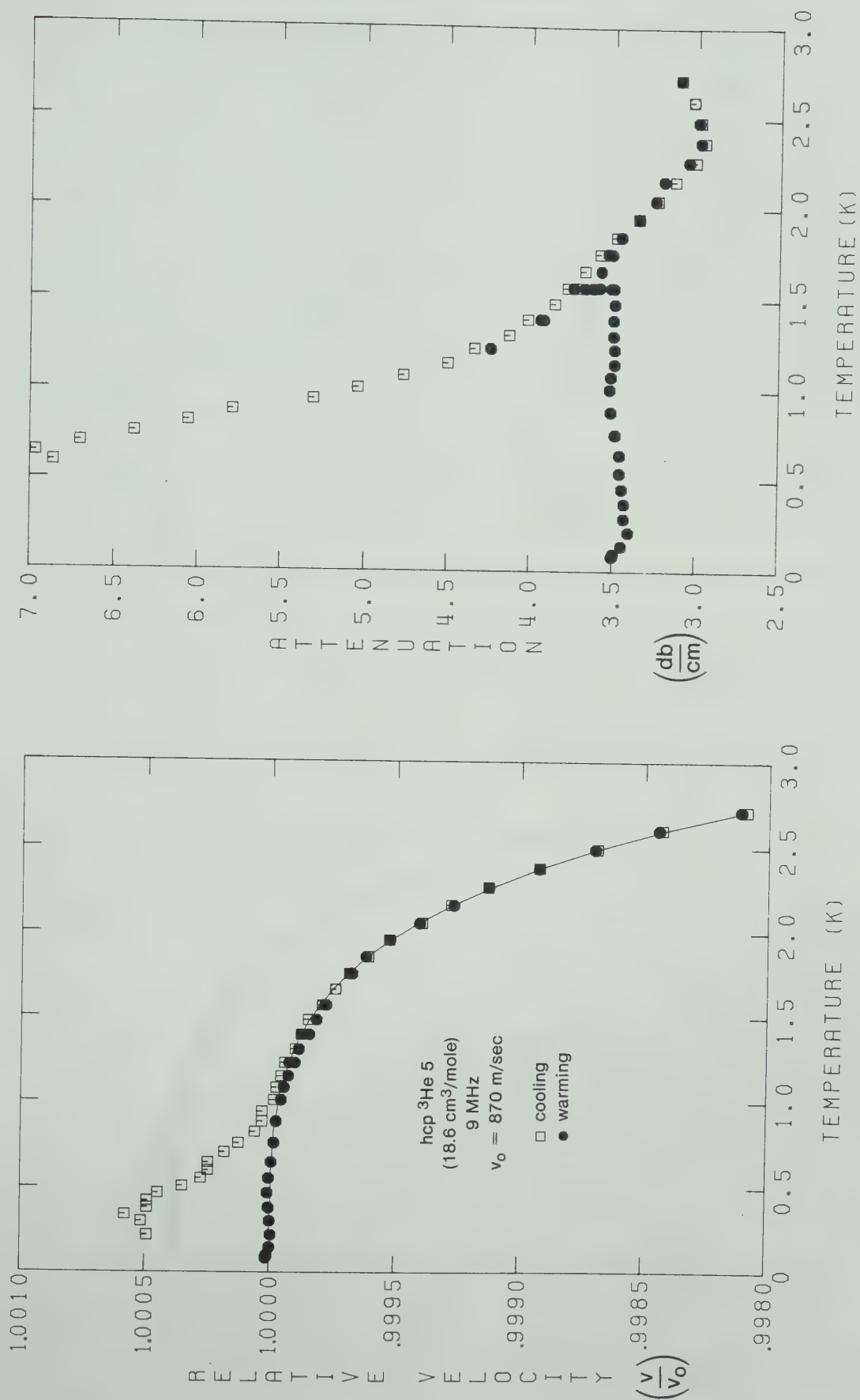
4.2 hcp ^3He

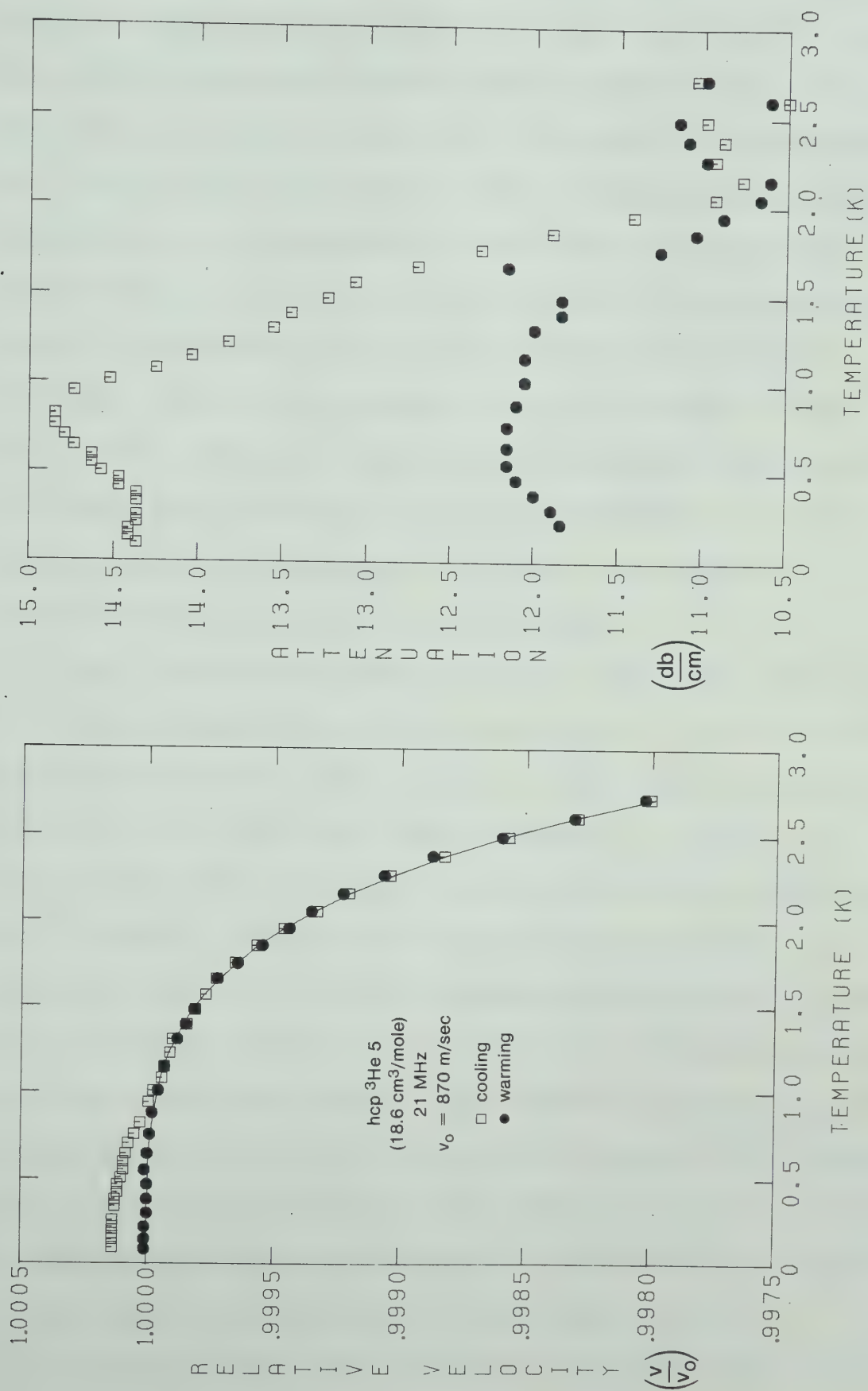
4.2-1 hcp ^3He 5 (@ 18.6 cm³/mole).

This crystal was studied in considerable detail and showed clearly all the features observed in other hcp ^3He crystals.

Figures 4.1, 4.2 and 4.3 show the actual velocity and attenuation data both on cooling (open squares) and

Figure 4.1 v and α in hcp ^3He @ 3 MHz

Figure 4.2 v and α in hcp ^3He 5 @ 9 MHz

Figure 4.3 v and α in hcp ^3He 5 @ 21 MHz

on warming (solid symbols). The line in the velocity plots is a fit of the adiabatic form $v - v_a(0) = aT^4 + bT^6$ to the velocity measured during cooling (above about 1.5 K). Note that the cooling velocities show positive deviations from the adiabatic form below 1.5 K, accompanied by large increases in the attenuation. The 3 MHz velocity could not be measured below 1 K due to the very large attenuation. Between 9 and 21 MHz the size of the velocity anomaly decreased. The 21 MHz attenuation had a maximum around 0.8 K. Note that only changes in attenuation are significant since the misalignment of the transducers resulted in a large apparent attenuation which was independent of temperature but increased with frequency.

The signal amplitude used during the 3 MHz measurements corresponded to a stress amplitude of about 100 Nt/m^2 . When the crystal was first cooled to the lowest temperature ($\sim 80 \text{ mK}$), no 3 MHz signal was observable. The pulse amplitude was then increased by about 12 db for 5 minutes (7×10^4 pulses). After this treatment, which warmed the crystal to about 160 mK, the attenuation had fallen to the low value shown in figure 4.1 (with about 40 echoes visible). When the crystal was warmed, the velocity was very near the adiabatic velocity and the attenuation remained low. Above about 1.3 K, the attenuation rose somewhat until by 2 K it had returned to its original value. The whole cycle could be reproduced by cooling again from above 2 K.

An attempt was made to observe the same effect at 9

and 21 MHz. The 9 and 21 MHz pulses used for measuring had stress amplitudes of about 20 Nt/m^2 which could only be increased by about 6 db without heating the crystal above 200 mK. No change in the attenuation or velocity was observed after the 9 or 21 MHz pulses were applied. By applying high amplitude 3 MHz pulses at low temperature, however, the attenuation and velocity at 9 and 21 MHz were changed to the values shown in figures 4.2 and 4.3. Both at 9 and 21 MHz the attenuation was greatly reduced and the velocity anomaly eliminated. After warming above 2 K, the 9 and 21 MHz velocity and attenuation recovered to their original values.

The effect of high amplitude pulses at low temperatures was studied systematically. By increasing the pulse amplitude by only 6 db above the measuring value, the change from high to low attenuation occurred slowly enough that it could be followed in detail. Figure 4.4A shows the sound velocity at 140 mK (as relative deviation from the adiabatic velocity) as a function of time. The solid symbols show the results for a repetition rate of 230 pulses per second while the open symbols are for 2300 pulses per second. In figure 4.4B the same data are plotted as a function of the number of pulses. The change in velocity is seen to depend on the total number of pulses with only a slight dependence on repetition rate. When the attenuation had decreased sufficiently for the velocity to become measurable ($t = 0$ in figure 4.4), the velocity

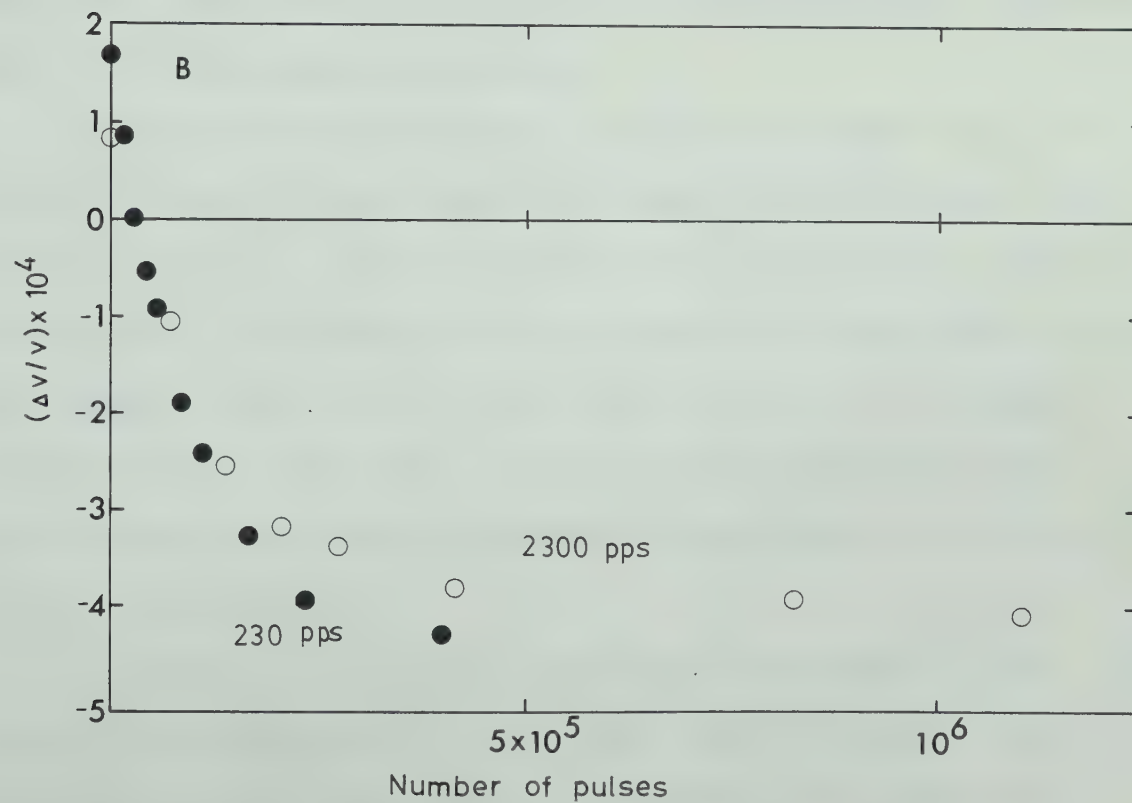
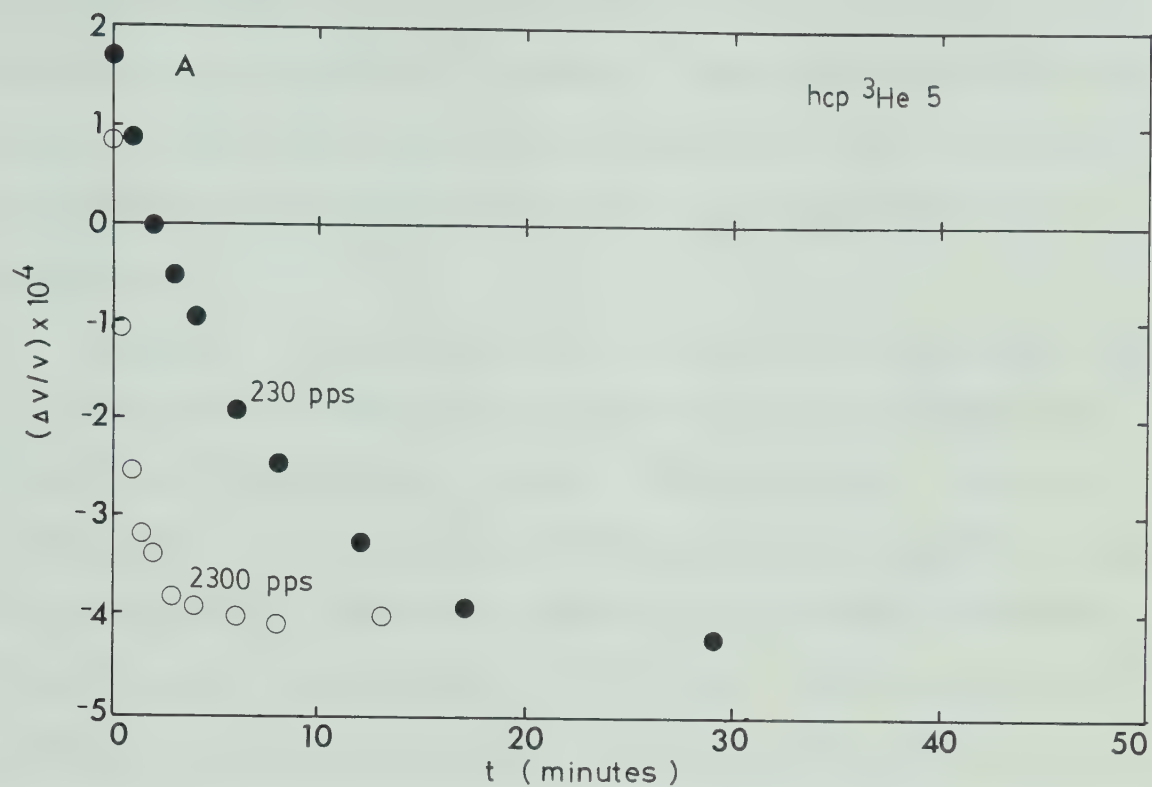


Figure 4.4 Time and Pulse number dependence of high amplitude 3 MHz pulse effect.

was larger than the adiabatic velocity. The deviation quickly became negative and reached a minimum after the application of about 10^6 pulses. The pulse amplitude was then increased by a further 6 db whereupon the velocity increased, reaching the adiabatic velocity after a few minutes.

Figure 4.5 shows the sound velocity and attenuation as functions of time (at a pulse rate of 230 pulses per second) at temperatures of 90, 140 and 255 mK. At each temperature, the initially positive anomaly decreased and became negative while the attenuation steadily decreased. At the lowest temperature (90 mK), the velocity started to increase toward the adiabatic velocity after about 15 minutes. The rate at which the process occurred decreased as the temperature was raised.

Although no systematic measurements were made, the effect of the pulses increased when the pulse amplitude was increased. With no pulses being transmitted through the crystal, no hysteresis was observed, even after leaving the sample below 100 mK overnight, while at the highest amplitude (~ 12 db above the measuring amplitude) the attenuation and velocity anomaly were greatly reduced in just a few minutes.

In order to better understand the effect of the pulses, measurements of the 3 MHz sound velocity and attenuation were made after subjecting the crystal to various numbers of high amplitude pulses. The results are

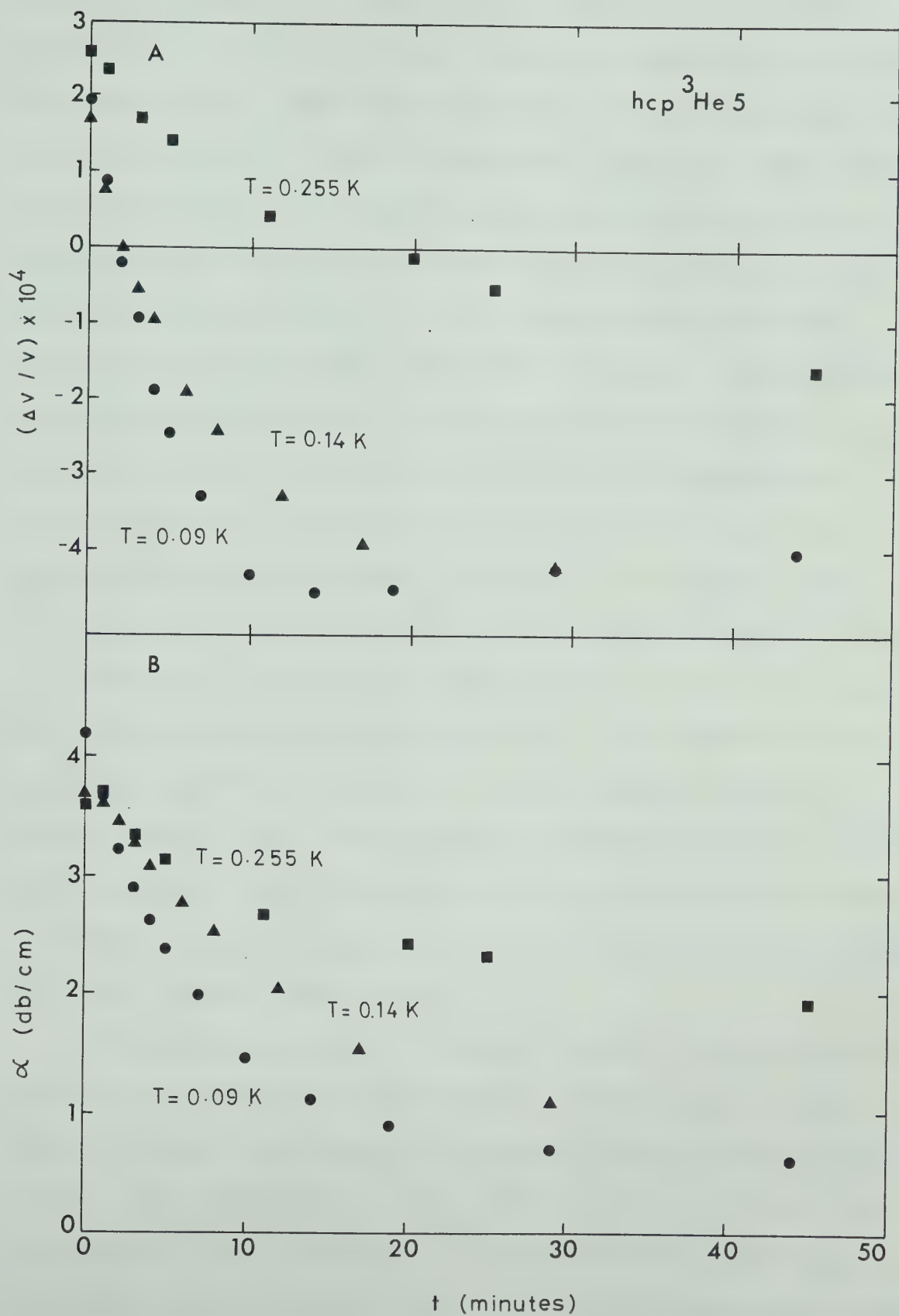


Figure 4.5 Temperature dependence of high amplitude 3 MHz pulse effect.

shown in figure 4.6. The crystal was cooled from near melting to around 100 mK and the pulse amplitude increased by about 6 db. When the attenuation dropped sufficiently that the velocity could be measured, the pulse amplitude was reduced and the crystal warmed while measuring the velocity and attenuation. The results are shown by the triangles in figure 4.6. Only the relative deviation $\Delta v/v_0$ from the adiabatic velocity is shown. The velocity anomaly was positive at low temperatures and became slightly negative above 0.6 K while the attenuation decreased. After reaching 1.3 K, the crystal was cooled and a few more high amplitude pulses applied. The velocity and attenuation dropped somewhat to the values shown by circles in figure 4.6. On warming, the velocity and attenuation behaved much as in the previous run. The procedure was repeated twice more, with the crystal being cooled to around 100 mK from near melting and high amplitude pulses being applied. The data shown as open squares and crosses in figure 4.6 correspond to the application of successively more and larger 3 MHz pulses.

Comparing the data in figure 4.6 to the curves shown in figure 2.5 for the dislocation contributions to the sound velocity and attenuation reveals remarkable similarities. The four solid lines shown in figure 4.6 are the dislocation contributions to v and α for an exponential distribution of loop lengths with different average lengths. The dislocation parameters are chosen as density

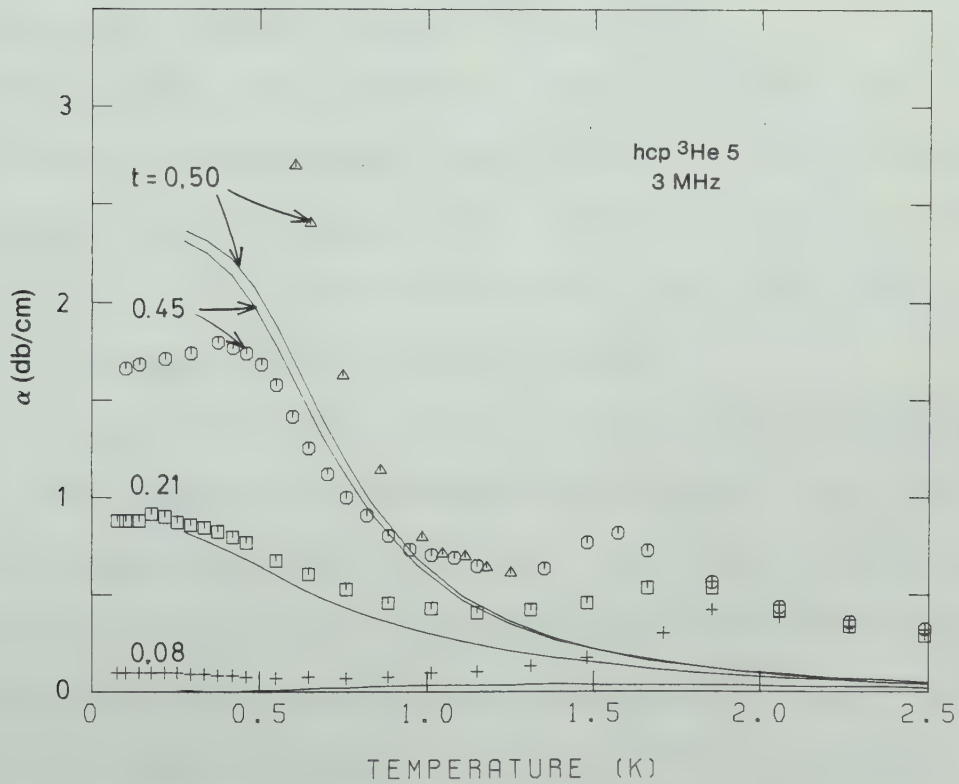
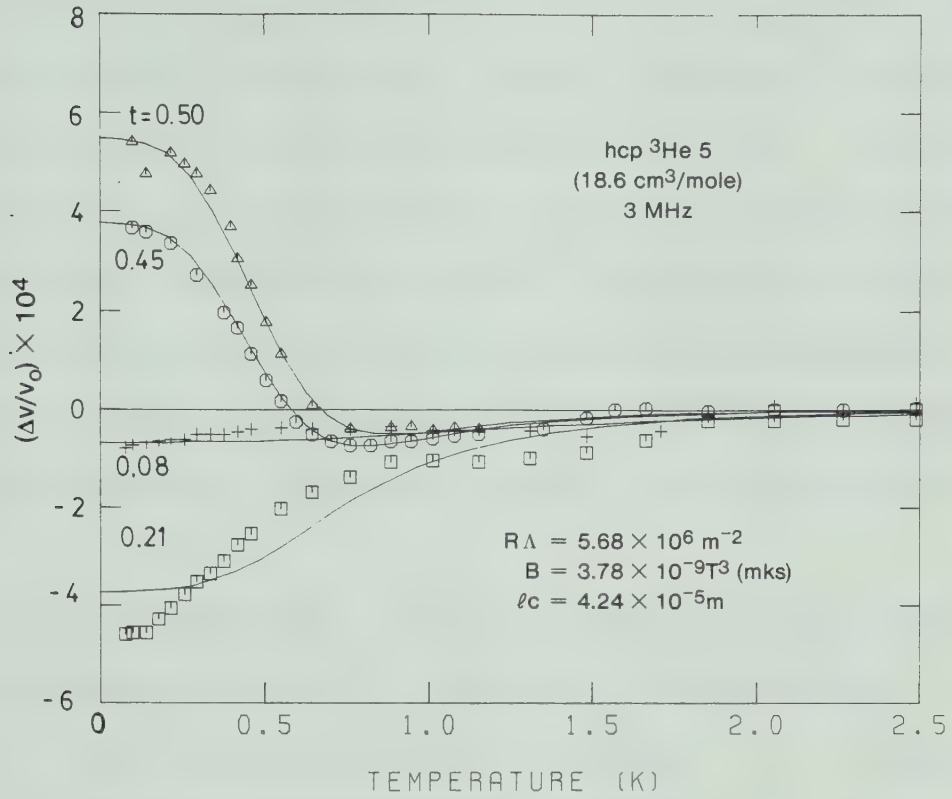


Figure 4.6 Dislocation pinning by high amplitude 3 MHz pulses (effect on v and α)

$RA = 5.68 \times 10^6 \text{ m}^{-2}$, damping $B = 3.78 \times 10^{-9} \text{ T}^3 \text{ mKs}$ and the values of t ($= L/\ell_c$) are 0.50, 0.45, 0.21 and 0.08. The choices of B and RA were made to give the best fit to the velocity data shown as open circles ($t = 0.45$). Only the parameter t was then changed in order to fit the velocity for the other three sets of data. The agreement of the measured velocity with the other curves is fairly good. The curves shown for the attenuation were then calculated from the parameters derived from the fit to the velocity data.

It thus seems that, if the velocity anomaly and the high attenuation are due to vibrating dislocations, the effect of applying high amplitude pulses at low temperature is to shorten the average loop length (i.e. pin the dislocations) and thus reduce the anomaly.

For comparison, figure 4.7 shows the same velocity data fitted to dislocation theory with a damping term B proportional to T^2 (figure 4.7A) and to T^4 (figure 4.7B). The fit using $B \propto T^2$ is considerably worse but that using $B \propto T^4$ is almost as good as the T^3 fit.

In order to further relate the anomaly to dislocations, its frequency dependence was studied. For this, only the data taken during cooling were used so that the length distribution was not affected by the large 3 MHz pulses. The existence of a positive anomaly at 9 MHz, reduced in size at 21 MHz, is in qualitative agreement with dislocation theory (cf. figure 2.6).

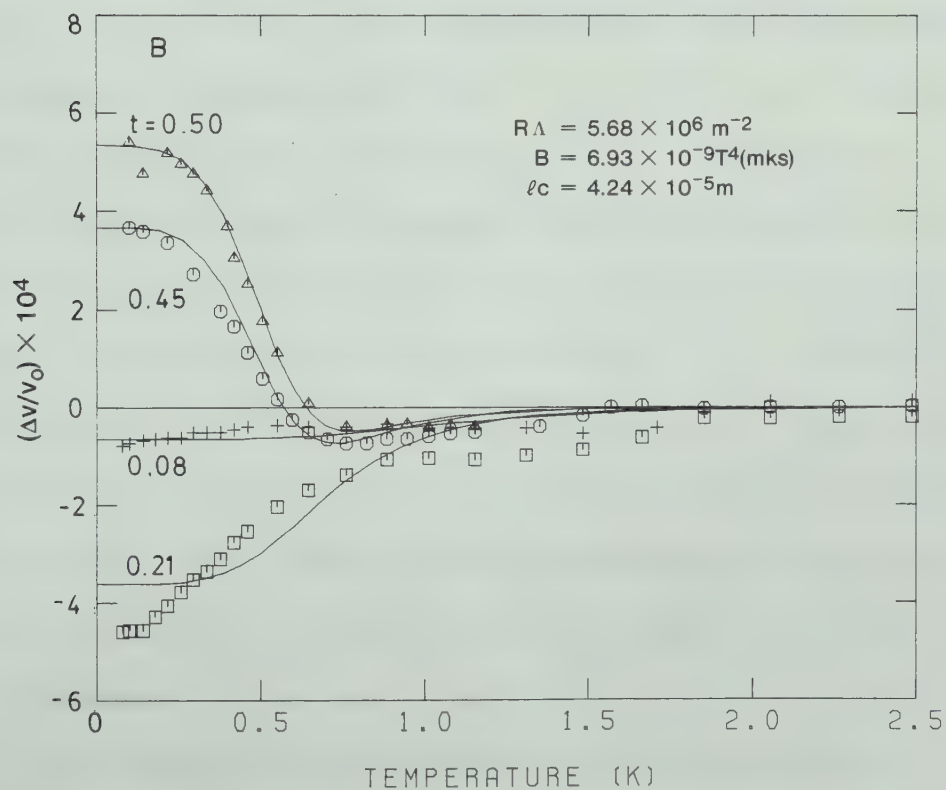
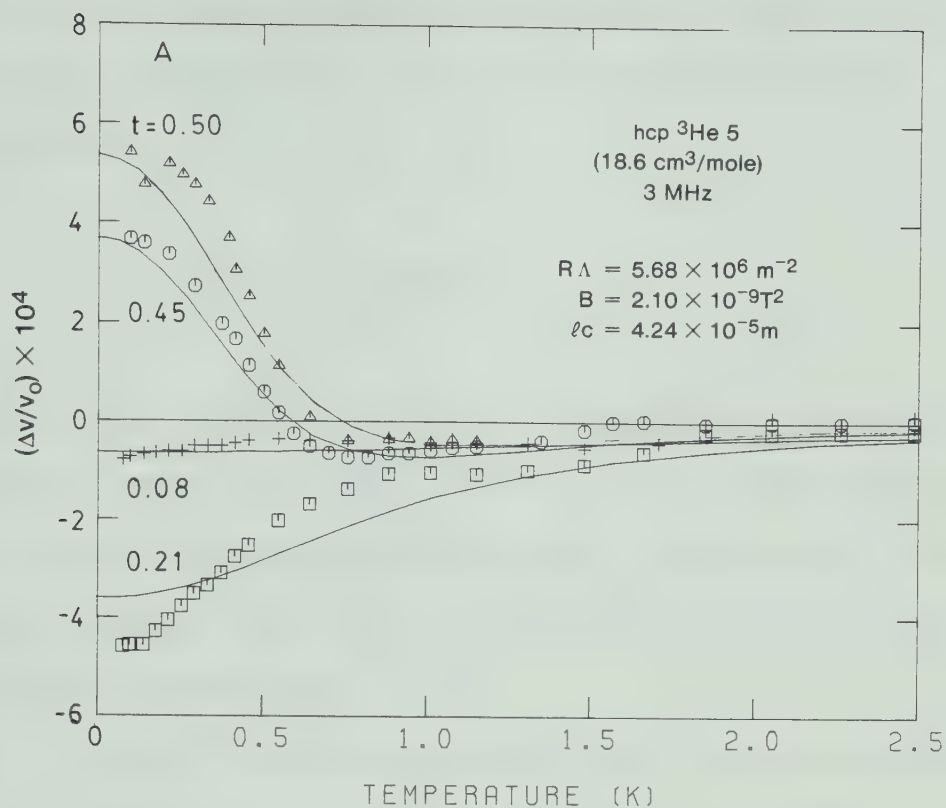


Figure 4.7 Effect of temperature dependence of dislocation damping on velocity fits.

The data were fitted to the Granato-Lücke theory outlined in section 2.3 with the exponential length distribution

$$N(\ell) = \frac{\Lambda}{L^2} \exp \frac{-\ell}{L} . \quad (2.3-9)$$

The fits were made on a graphics computer terminal by choosing a value of L that gave the best qualitative agreement with the velocity data and then varying $R\Lambda$ to match the magnitude of the anomaly and B to best match the temperature dependence.

In figure 4.8 the anomalies found during cooling at 3, 9 and 21 MHz are compared to dislocation theory (solid curves). Due to the high attenuation, the 3 MHz data (open squares) extend only down to 0.88 K, not low enough to see a significant velocity anomaly. The data at 9 MHz (open circles) show the largest velocity anomaly and the dislocation parameters are determined using this anomaly. The resulting values are $R\Lambda = 1.84 \times 10^7$, $B = 1.41 \times 10^{-8} \text{ T}^3 \text{ mks}$, $L = 6.37 \times 10^{-5} \text{ m}$. The dependence $B \propto T^3$ was chosen in view of the results shown in figures 4.6 and 4.7 and gives a reasonable fit. Using these parameters to calculate the velocity at 21 MHz gives an anomaly slightly smaller than that observed.

The attenuation predicted by these parameters, however, is considerably less than that measured. On the other hand, the qualitative features of the dislocation predictions and

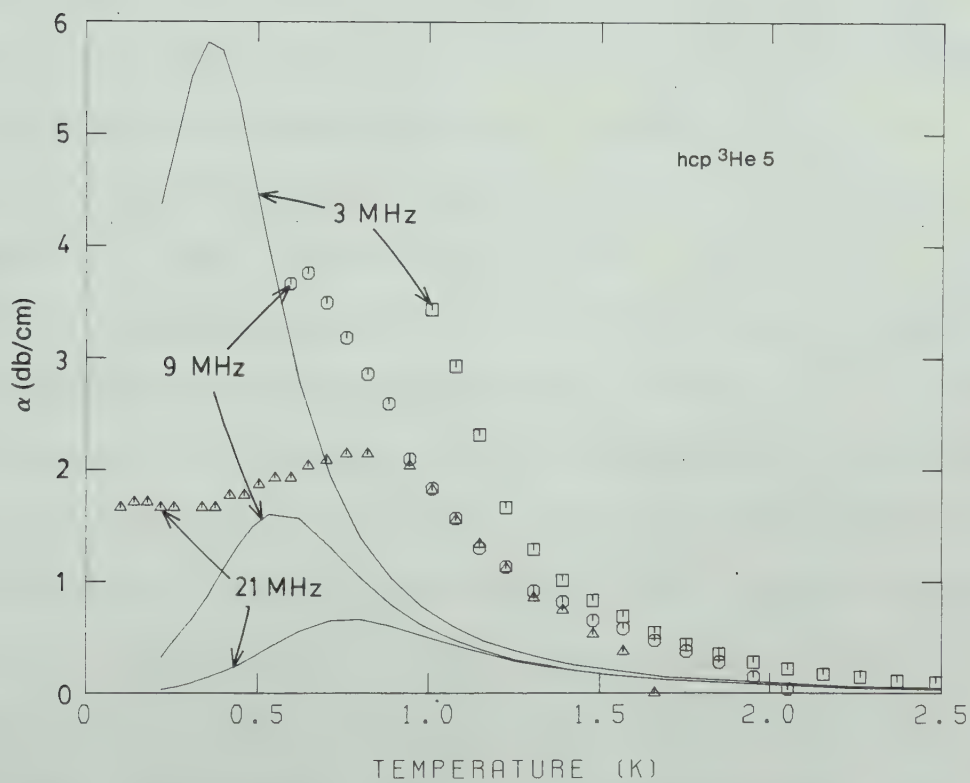
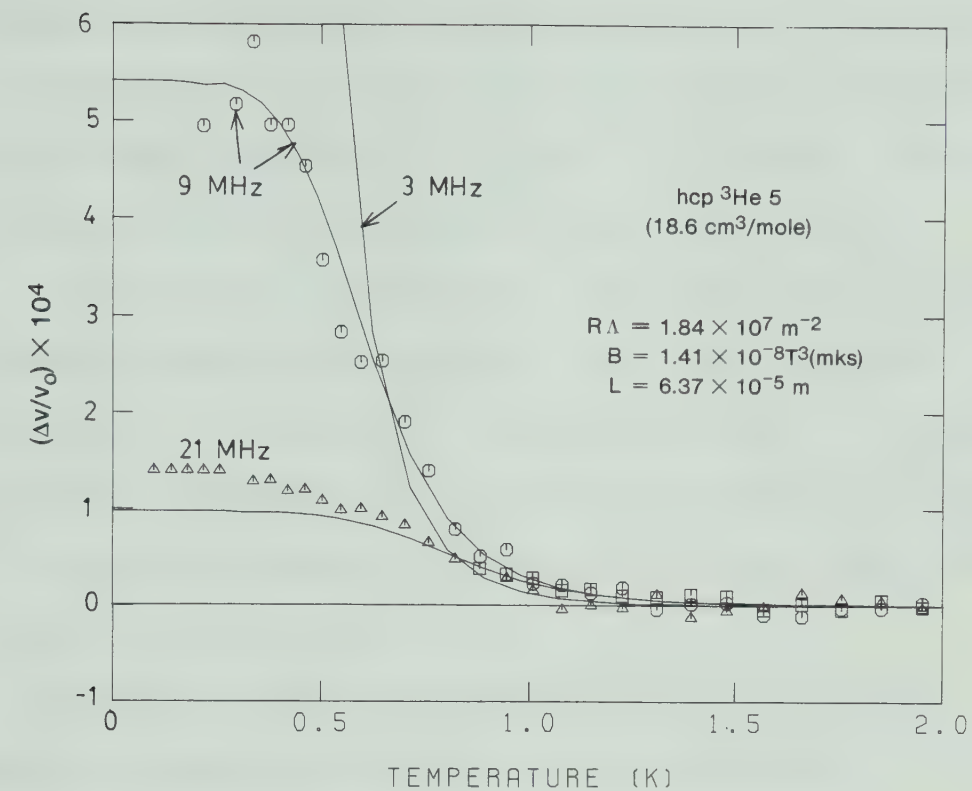


Figure 4.8 Dislocation fits of v and α for hcp ^3He 5 using 9 MHz velocity data.

experiment are similar. Both show a rising attenuation as the temperature is lowered with the largest attenuation at 3 MHz and the smallest at 21 MHz. In addition, both show a maximum in the 21 MHz attenuation around 0.8 K.

Figure 4.9 shows the same data with the dislocation parameters found by fitting to the 21 MHz velocity. The parameters thus found ($RA = 2.63 \times 10^7$ and $B = 1.71 \times 10^{-8} \text{ T}^3 \text{ mks}$) differ somewhat from those found using the 9 MHz data but the general features of the dislocation contributions to v and α are the same.

Unfortunately, the parameters found by fitting the frequency dependent velocity anomaly on cooling do not agree with those found at 3 MHz after applying high amplitude pulses ($RA = 5.68 \times 10^6 \text{ m}^{-2}$, $B = 3.78 \times 10^{-9} \text{ T}^3 \text{ mks}$). Since the fitting parameters at 9 and 21 MHz do not agree, some of this discrepancy may be due to the difference in frequency (3 MHz instead of 9 or 21). Also, both the frequency dependence predicted for the anomaly and the relationship between the velocity anomaly and the attenuation depend on the choice of an exponential distribution of dislocation lengths. If the high amplitude pulses do pin dislocations, the distribution of loop lengths should change. The choice of distribution also affects the values found for RA and B . Iwasa et al. (1979) found that, in hcp ^4He , the velocity anomaly did not decrease with frequency as rapidly as dislocation theory predicted for an exponential length distribution. They were able to get a

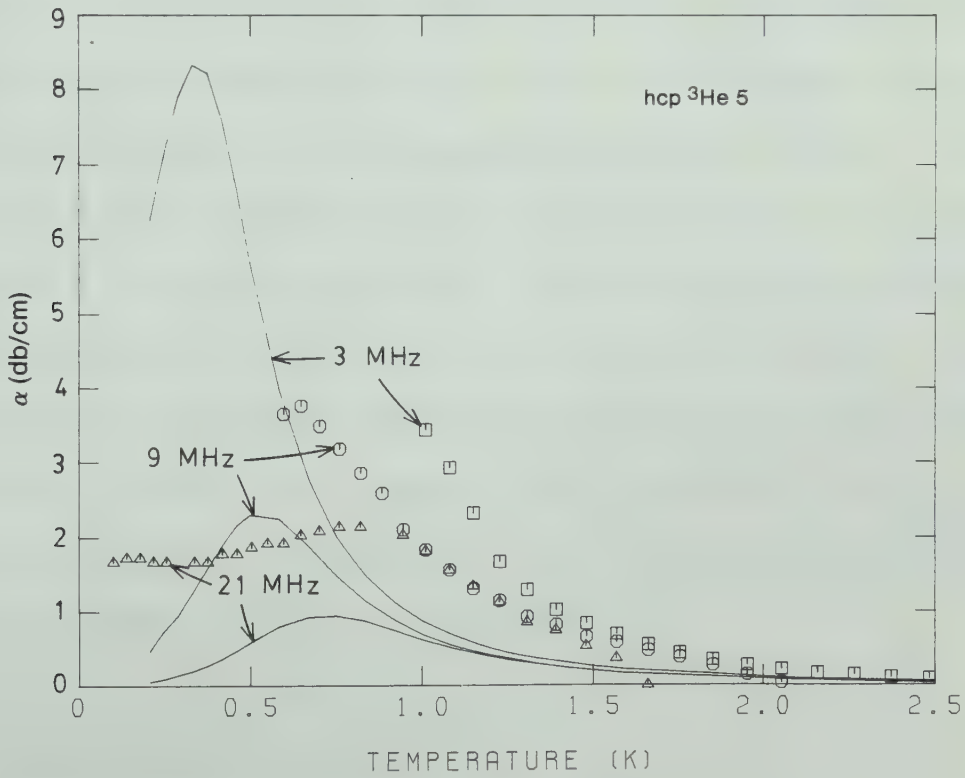
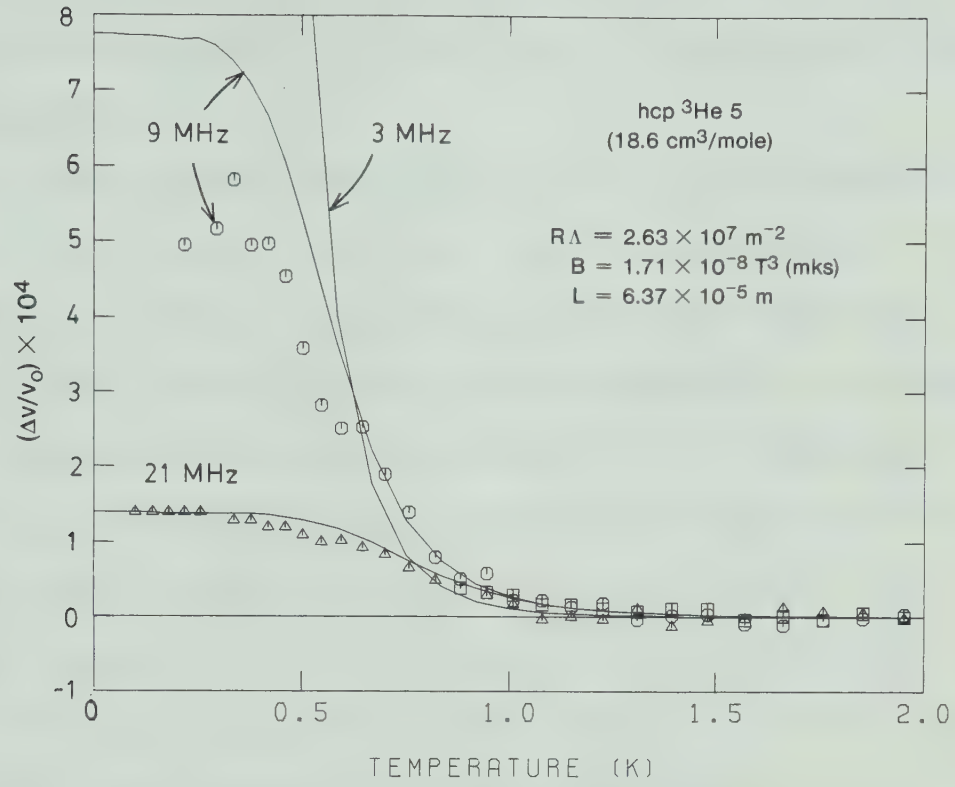


Figure 4.9 Dislocation fits of v and α for hcp ^3He 5 using 21 MHz velocity data.

better fit by choosing a Gaussian distribution of loop lengths at the expense of introducing an additional adjustable parameter.

It thus appears that the velocity and attenuation of sound in this crystal can be at least qualitatively explained in terms of vibrating dislocations which are pinned at low temperatures by high amplitude 3 MHz pulses. Before leaving the discussion of hcp ^3He 5, something should be said about the high temperature recovery of v and α to their original values. In this crystal, the recovery occurred in the temperature range between 1.3 and 1.8 K. In this region the dislocations are so strongly damped that the velocity is very nearly equal to the adiabatic velocity and no change with time was observed. The attenuation, however, still has a significant dislocation contribution at this temperature and in figure 4.2, for example, the effect can be seen of holding the crystal at around 1.5 K during warming. The attenuation returned (over a period of 10 minutes) to its cooling value. This time dependent recovery during warming was observed between 1.3 and 1.8 K with the recovery rate increasing rapidly with temperature. It is discussed in detail in section 4.6 for this crystal as well as for bcc ^3He .

4.2-2 hcp ^3He (@ 18.6 cm³/mole)

Several other crystals were grown at this density. Of these, two had sufficiently complete data for an analysis

in terms of dislocations.

The general behaviour of the velocity and attenuation in these crystals was the same as for hcp ^3He 5. At high temperatures, the velocity was adiabatic and the attenuation low. When the crystal was cooled below about one half the melting temperature, the attenuation rose and the velocity deviated from the adiabatic form.

In these crystals the 3 MHz velocity anomaly was negative. This corresponds to a shorter average dislocation loop length than that observed in hcp ^3He 5. In figure 4.10, the data and fit for hcp ^3He 2 are shown. Since the poor 9 MHz signal only allowed measurements to be made down to about 0.8 K, the fitting was done using the 3 MHz velocity data. Again, there is at least qualitative agreement between the predicted and measured attenuation.

Figure 4.11 shows the anomaly in hcp ^3He 3. It is similar to that in figure 4.10 except that it is an order of magnitude smaller. The fit is again made to the 3 MHz data and gives good agreement, both with the 9 MHz velocity and the attenuation.

The values of B ($1.00 \times 10^{-8} \text{ T}^3 \text{ mks}$ for both) and of L (5.94×10^{-6} and $1.02 \times 10^{-5} \text{ m}$ for hcp ^3He 2 and hcp ^3He 3, respectively) are comparable but the dislocation density ρ is quite different. This difference (between $4.28 \times 10^7 \text{ m}^{-2}$ and 1.70×10^6) could either be due to a real difference in the dislocation density Λ or to a difference in the

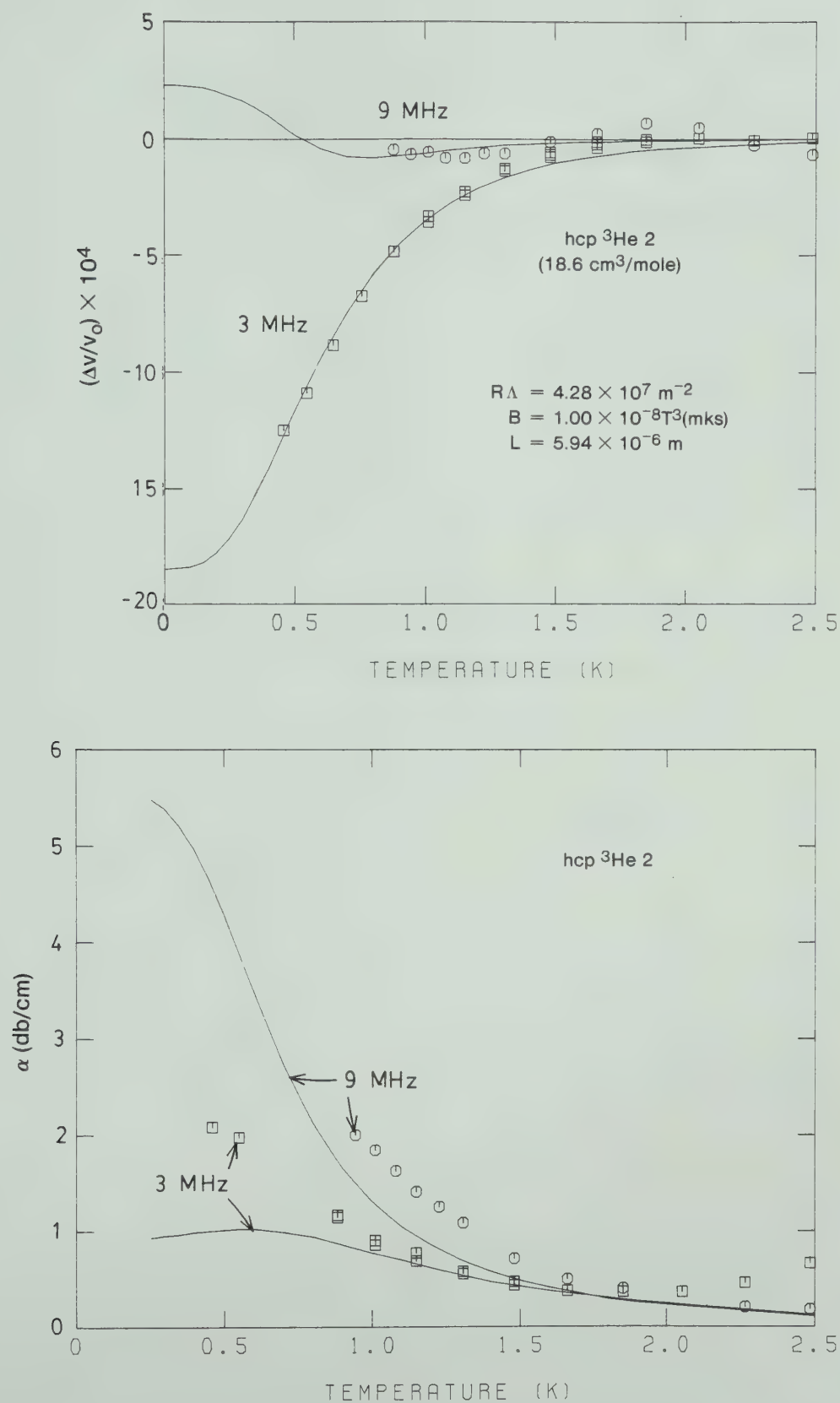


Figure 4.10 Dislocation fits (3 and 9 MHz) of v and α for hcp $^3\text{He 2}$.

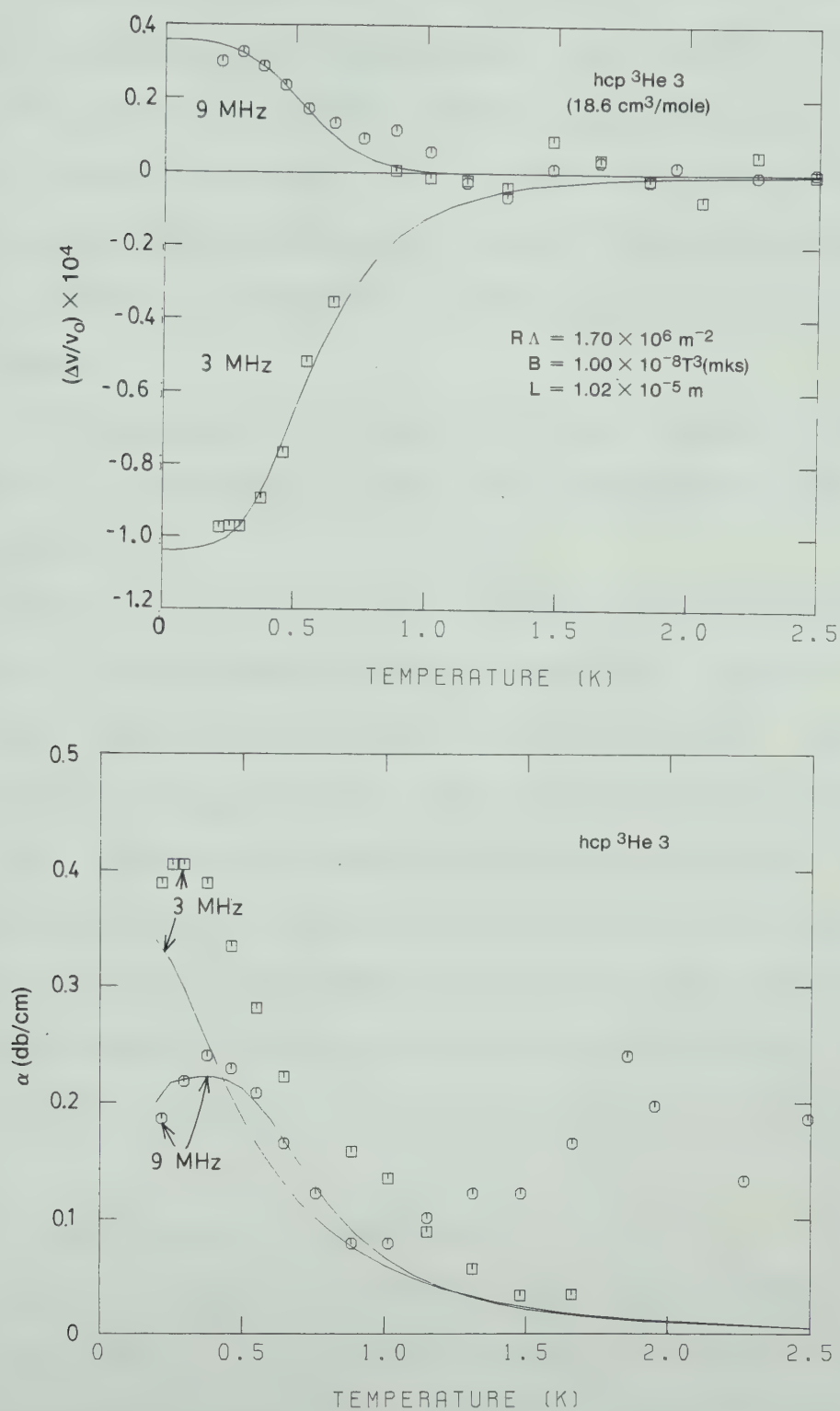


Figure 4.11 Dislocation fits (3 and 9 MHz) of v and α for hcp $^3\text{He 3}$

orientation factor R (cf. figure 2.2).

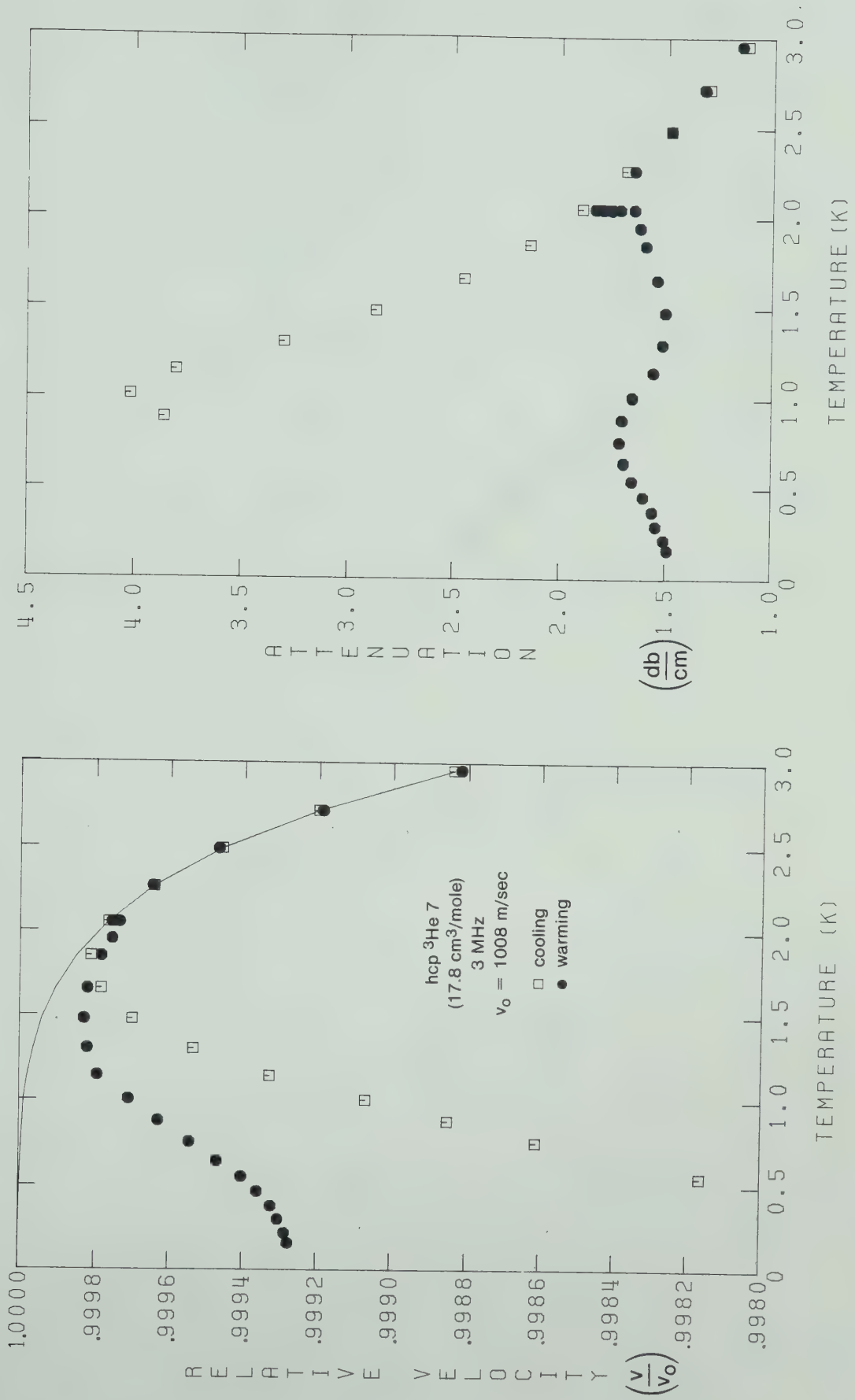
When high amplitude 3 MHz pulses were applied to these crystals at low temperatures, the negative 3 MHz velocity anomalies became smaller while the positive 9 MHz anomaly became negative. At the same time, both the 3 and 9 MHz attenuation decreased. In the dislocation model, these features correspond to a shortening of the dislocation loops.

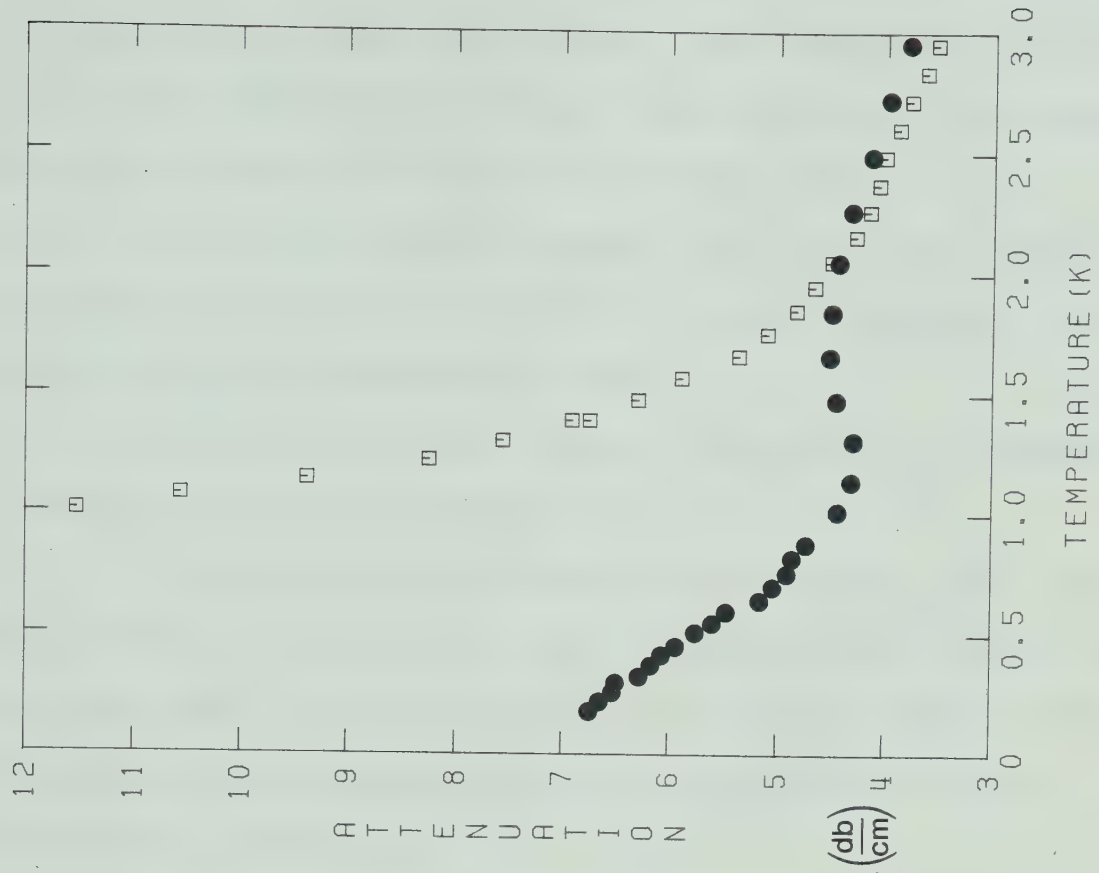
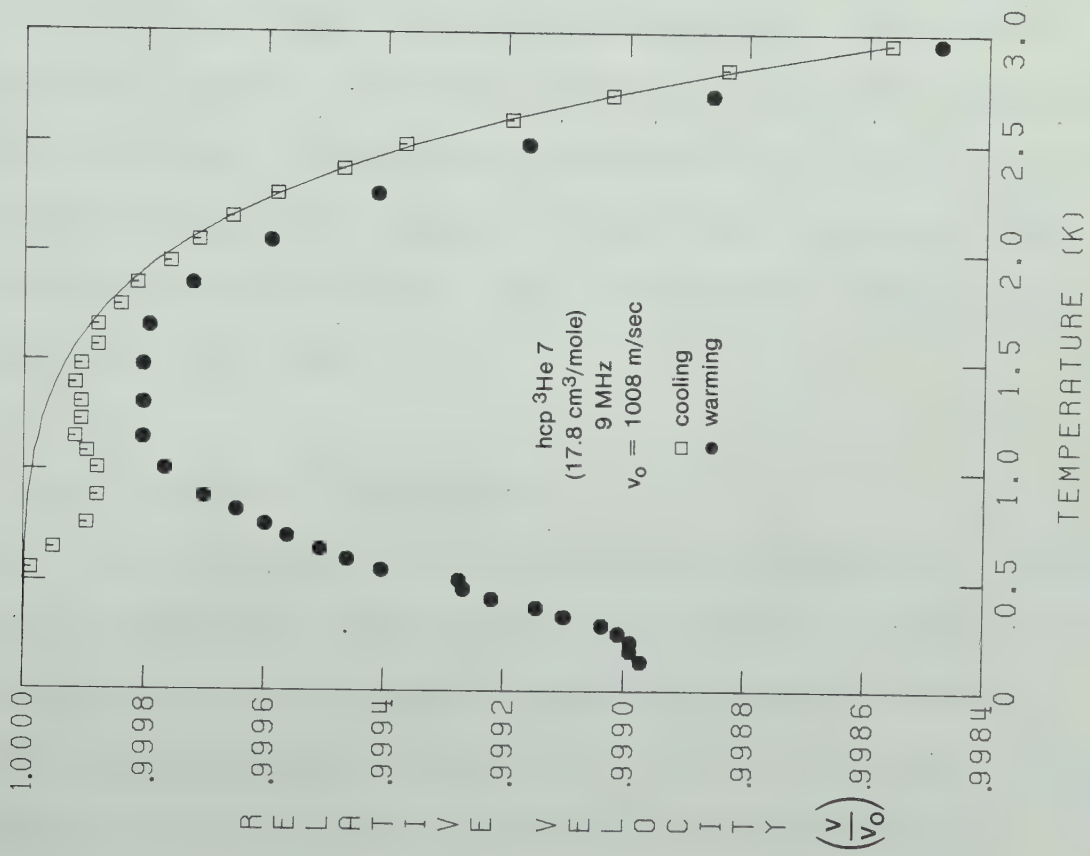
The recovery of v and α to their original values occurred in the range 1.3 to 1.8 K for both of these crystals.

Although several other crystals of pure hcp ^3He were grown at $18.6 \text{ cm}^3/\text{mole}$, none of them had a complete set of data. What measurements were made, however, were in qualitative agreement with the crystals already described. That is, there was a negative velocity anomaly at 3 MHz and a positive one at 9 MHz accompanied by high attenuation. By applying high amplitude 3 MHz pulses these were changed to small negative anomalies with low attenuation. Warming above 1.8 K returned the anomalies to their original form.

4.2-3 hcp ^3He (@ $17.8 \text{ cm}^3/\text{mole}$)

Only two hcp ^3He crystals were grown at this density. The data taken at 3 and 9 MHz on one of these (hcp ^3He 7) are shown in figures 4.12 and 4.13. The open symbols are data taken on cooling, the solid ones are on warming after applying high amplitude 3 MHz pulses.

Figure 4.12 v and α in hcp $^3\text{He } 7$ ($17.8 \text{ cm}^3/\text{mole}$) @ 3 MHz

Figure 4.13 v and α in hcp $^3\text{He } 7$ ($17.8 \text{ cm}^3/\text{mole}$) @ 9 MHz

Due to a rather poor signal, the measuring amplitude had to be quite high and itself affected the 3 MHz anomaly when the crystal was cooled below about 400 mK. The anomaly was not as greatly reduced as in the less dense crystals but the "high amplitude" pulses were only 4 db greater than the measuring pulses.

The recovery in this crystal occurred at a somewhat higher temperature of about 2 K.

In figure 4.14 the anomaly during cooling and the dislocation fit are shown. The velocity is fit fairly well but again the measured attenuation is larger than, although in qualitative agreement with, that predicted from the dislocation parameters.

The other hcp ^3He crystal grown at $17.8 \text{ cm}^3/\text{mole}$ had an anomaly an order of magnitude smaller. Since this velocity anomaly was barely resolvable at 3 MHz and not at all at higher frequencies, no attempt was made to fit the data to dislocation theory. Again, the effects of high amplitude pulses and the high temperature recovery were the same as in hcp ^3He 7.

4.2-4. Effects of Impurities

One technique for studying dislocations is to remove their effects by completely pinning them. In conventional solids this can be done by introducing point defects, either by radiation damage or by adding impurities. The only practical method in helium is to add isotopic

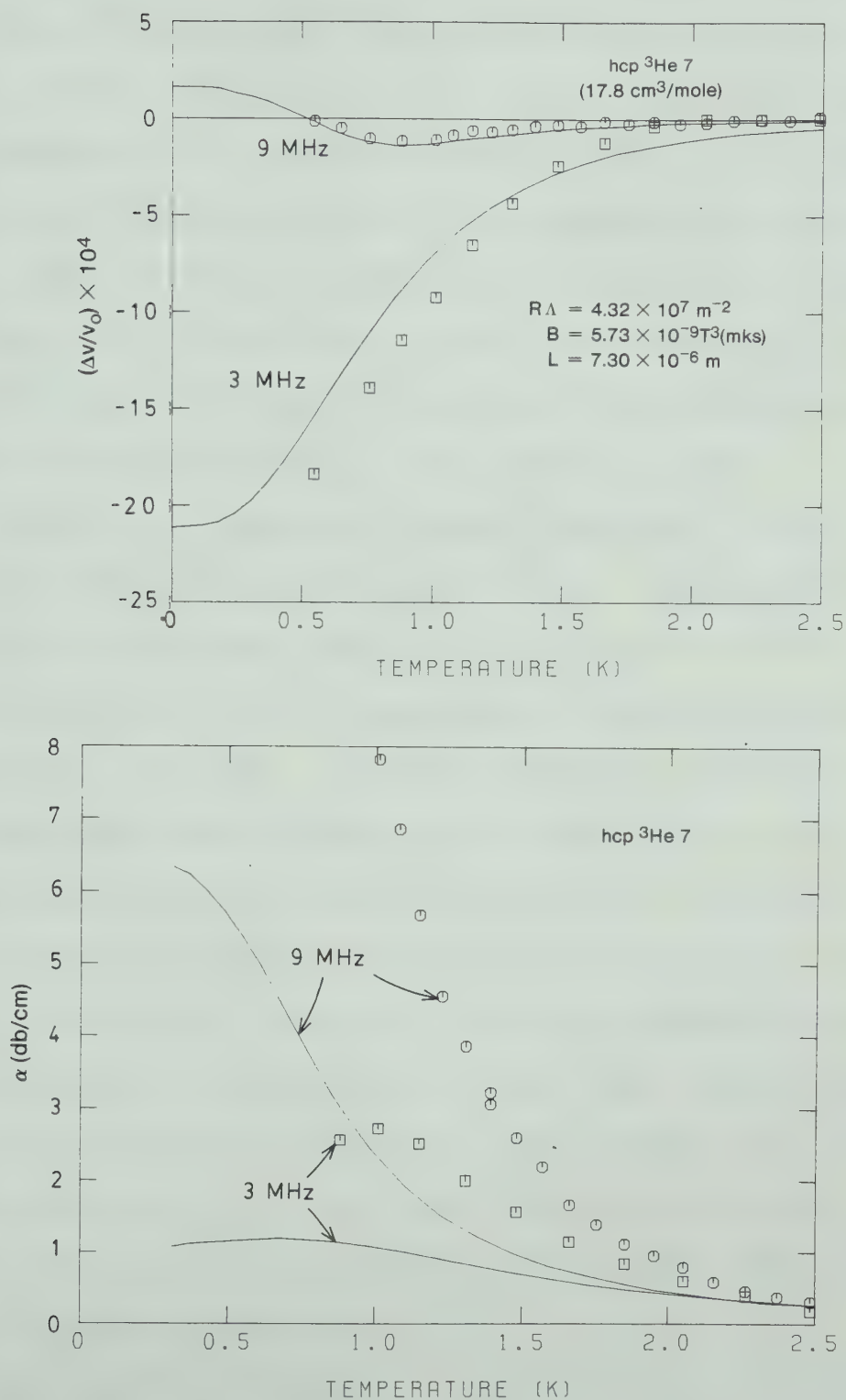


Figure 4.14 Dislocation fits (3 and 9 MHz) of v and α for hcp $^3\text{He 7}$.

impurities.

The crystals described up to this point were all grown from ^3He which was analysed as containing 1.35 ppm of ^4He . This is a rather small concentration but, in hcp ^4He , Paalanen et al. (1981) observed large effects on dislocation mobilities due to ^3He concentrations as low as 0.3 ppm. To check the effect of impurities, crystals were grown at $18.6 \text{ cm}^3/\text{mole}$, from ^3He containing ^4He in concentrations of 47 ppm, 430 ppm and 0.53% (denoted by *, ** and ***, respectively, in the crystal's name).

Figure 4.15 shows the anomaly observed during cooling in *hcp ^3He 12 (47 ppm of ^4He). Although there are only limited data, the quality of the fit and the values of the dislocation parameters found are comparable to those for pure ^3He . The other features involving the high amplitude 3 MHz pulses and the recovery at high temperature showed no influence due to the ^4He impurities.

Figure 4.16 shows the anomaly in **hcp ^3He 13 (430 ppm). The velocity fit is good but the attenuation fit shows the 3 MHz attenuation as larger than that at 9 MHz, in contrast to the measurements. The changes in v and α due to high amplitude 3 MHz pulses occurred somewhat more quickly than in the pure crystal but no other effects due to the impurities were seen.

The next two figures 4.17 and 4.18 show the data from ***hcp ^3He 17 which contained 0.53% ^4He . The anomaly was completely absent and applying high amplitude pulses

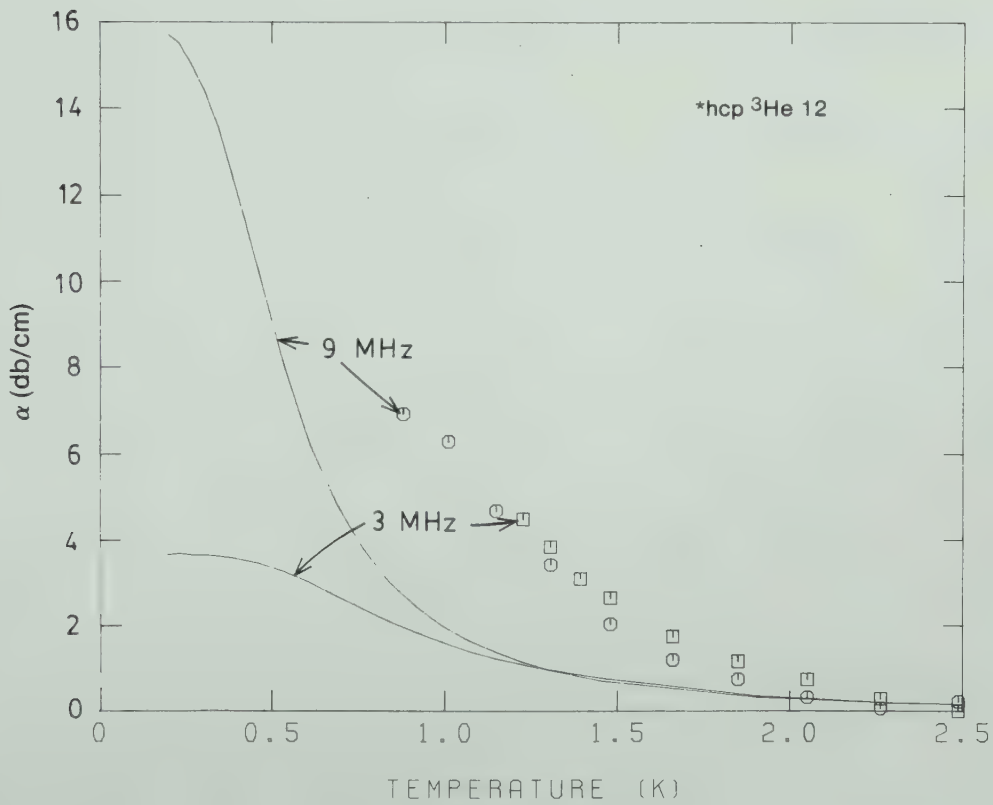
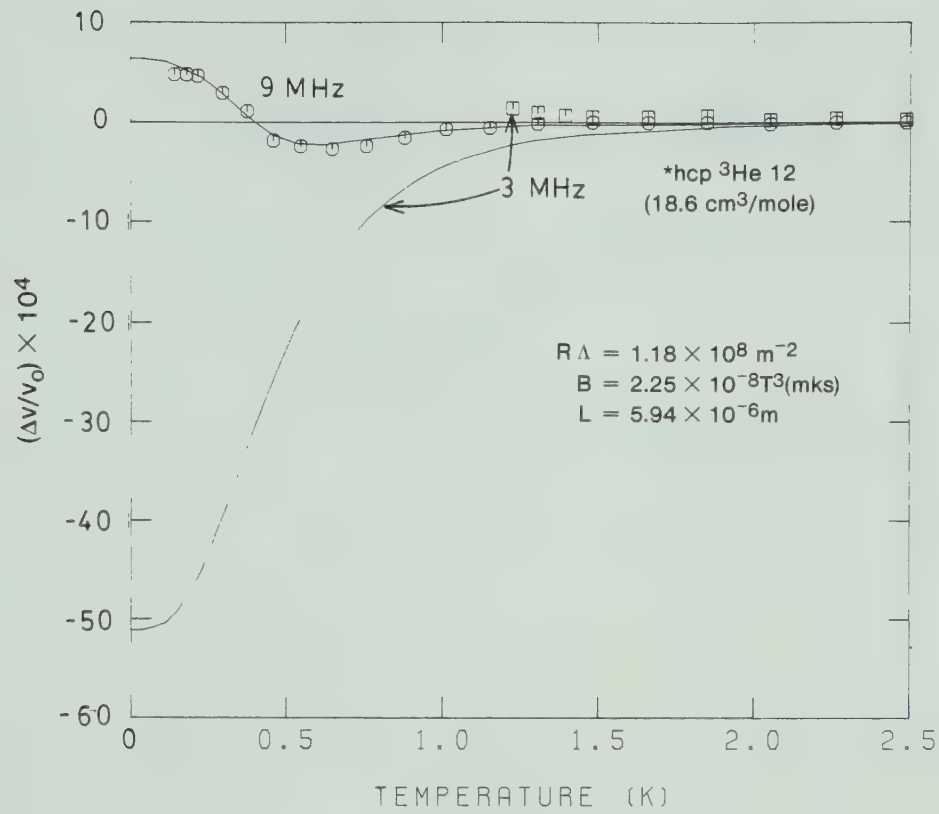


Figure 4.15 Dislocation fits (3 and 9 MHz) of v and α for *hcp ^3He 12 (47 ppm ^4He).

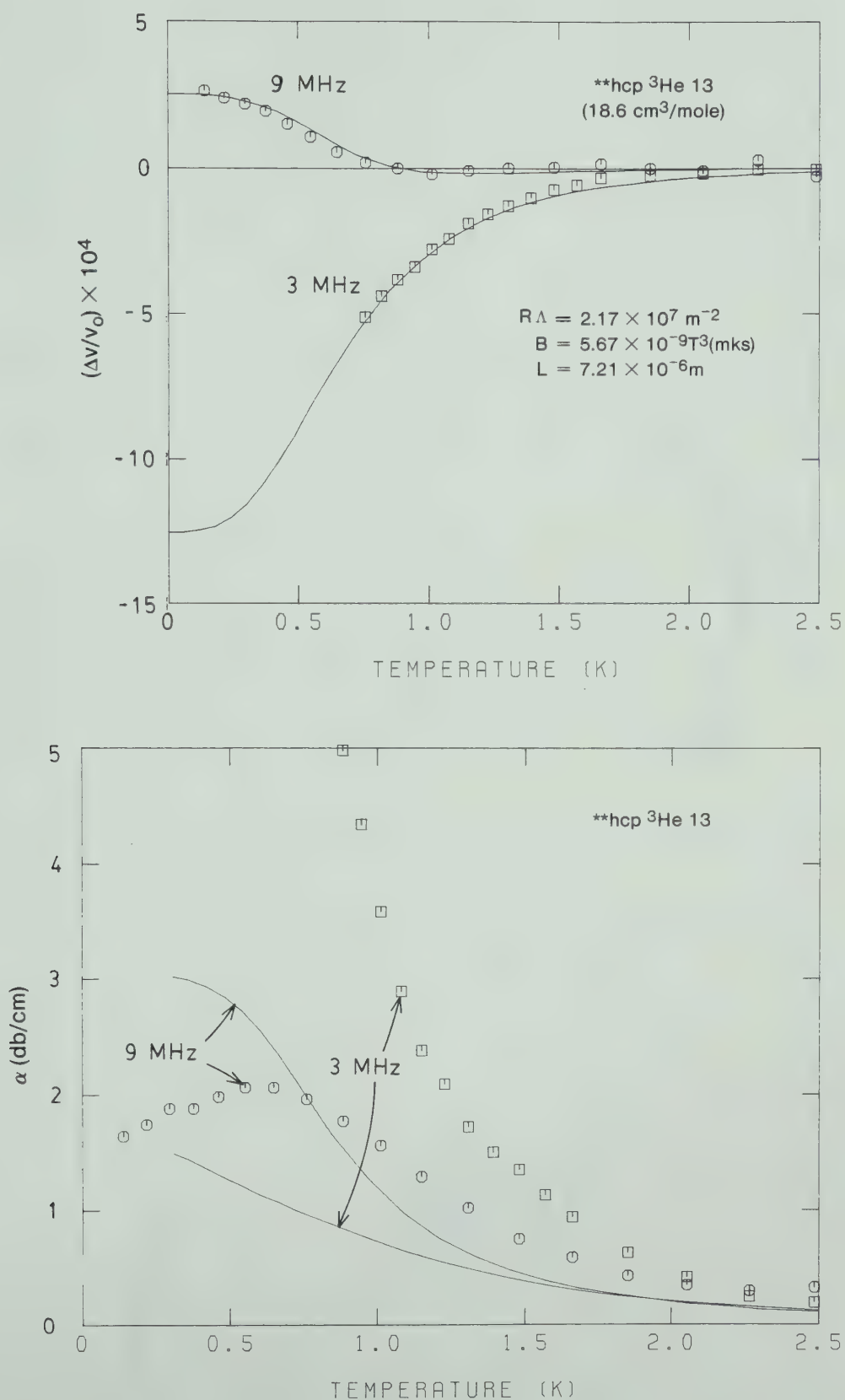
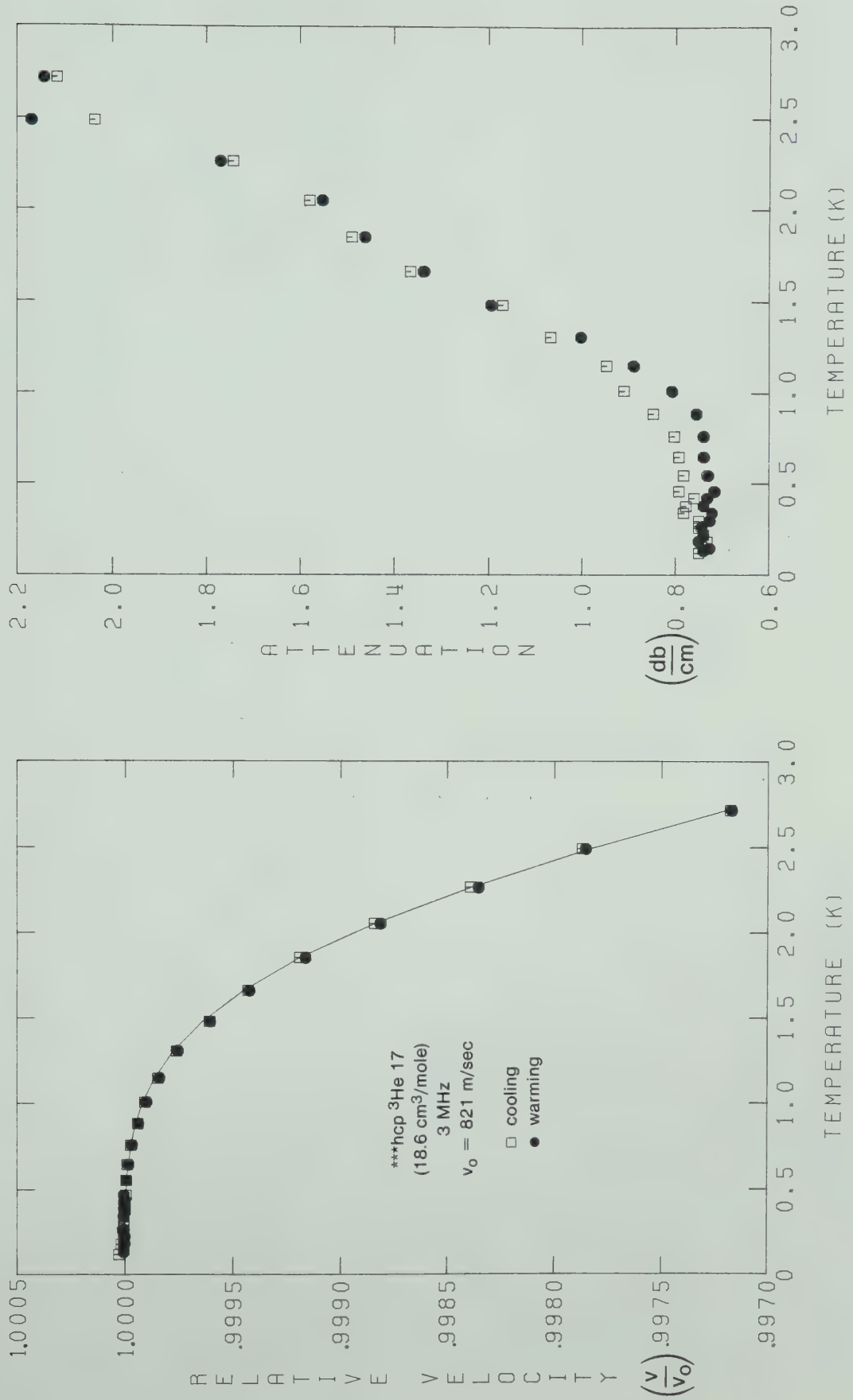


Figure 4.16 Dislocation fits (3 and 9 MHz) of v and α for ****hcp $^3\text{He } 13$ (430 ppm ^4He)**

Figure 4.17 v and α in ***hcp ^3He 17 (0.53% ^4He) @ 3 MHz

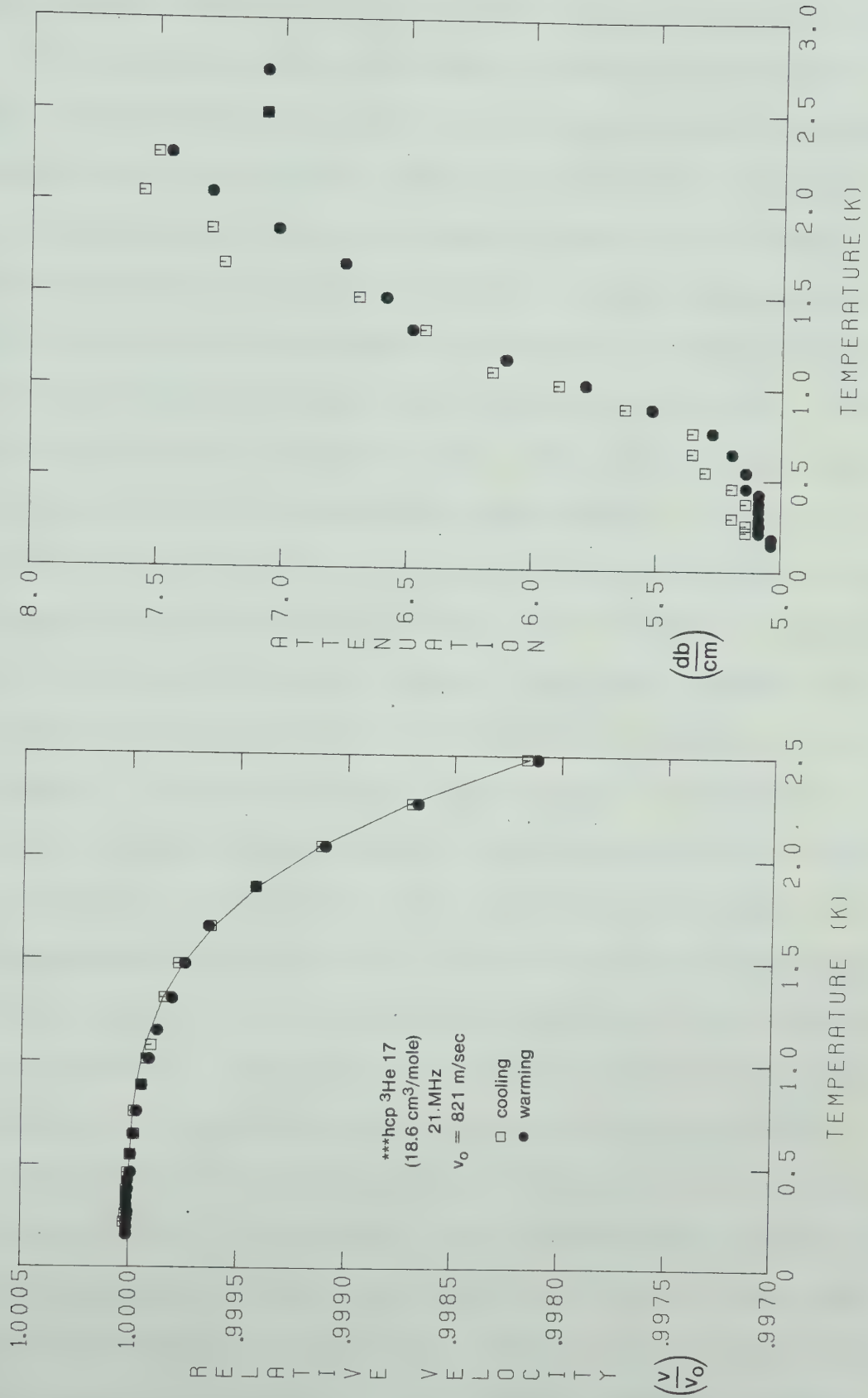


Figure 4.18 v and α in ***hcp ^3He 17 (0.53% ^4He) @ 21 MHz

did not result in any hysteresis. The remaining attenuation due to other processes is discussed further in section 4.8.

Although the high amplitude pulses did not affect v or α at the measuring amplitude, a reversible amplitude dependence of the velocity and attenuation was observed. The 3 MHz data of figure 4.17 were taken at the lowest stress amplitude of about 200 Nt/m^2 . These measurements were repeated at three higher amplitudes corresponding to stress amplitudes of about 400, 1600 and 4000 Nt/m^2 . The results are shown in figure 4.19. The data at the lowest amplitude (-6 db, indicated by open squares), showed no velocity anomaly and an attenuation rising with temperature, corresponding to complete pinning. At the next amplitude (0 db, indicated by open circles) there was a small negative velocity anomaly below 1 K and the attenuation had increased. At the two higher amplitudes, the negative velocity anomaly became larger, then became positive while the attenuation increased. The increase in attenuation and appearance of a velocity anomaly at high stress amplitude is typical of stress induced breakaway from impurity pinning points. The high amplitude attenuation is usually attributed to the hysteresis loss due to the unpinning and repinning of the dislocations during a half cycle of the sound wave. If, however, the dislocations are unpinned at the beginning of the sound pulse and are not repinned during the pulse because of the inertia of the dislocation line, then the attenuation and velocity anomaly at high

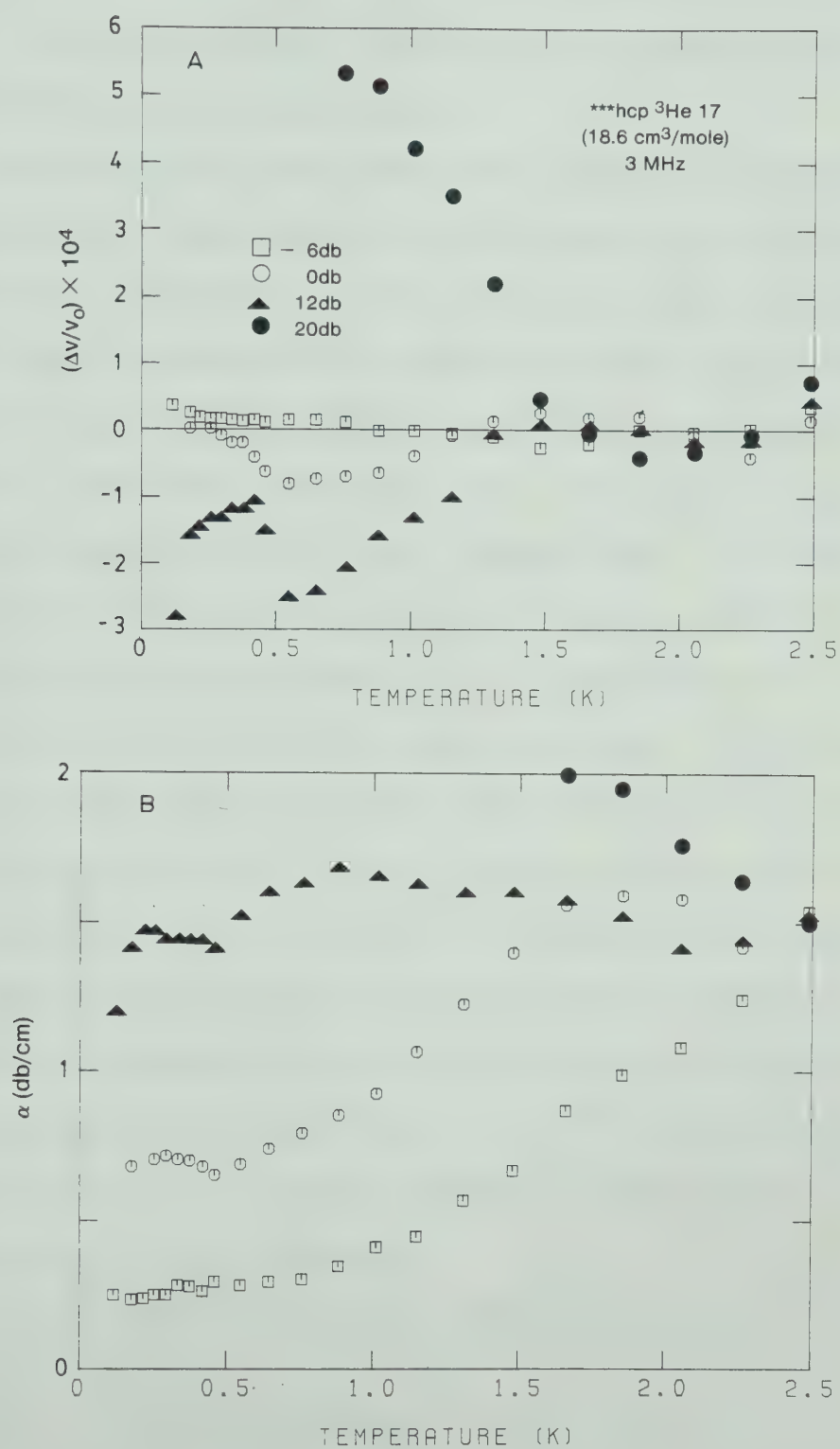


Figure 4.19 Amplitude dependence in ***hcp ^3He 17 (0.53% ^4He).

amplitude are the same as for the unpinned case.

Similar effects were seen in hcp ^4He with 30 ppm of ^3He by Iwasa and Suzuki (1980) who also attributed them to breakaway from impurities.

The amplitude dependence was further examined by measuring the attenuation as a function of pulse amplitude at various temperatures. The results, shown in figure 4.20A show an attenuation roughly constant up to some critical amplitude (marked by an arrow). Above the critical amplitude the attenuation increased. The critical amplitude was higher at lower temperature. The very similar results found by Iwasa and Suzuki (1980) were attributed to the condensation at low temperature of the ^3He impurities onto the dislocation lines. The average pinning length depends on the exact shape of the dislocation (Gerold, 1979). For an ideally straight dislocation, the average pinning length is inversely proportional to the impurity concentration c while for a completely flexible dislocation free to move in its glide plane, the pinning length is proportional to $c^{-1/2}$. The true concentration dependence of the impurity pinning length probably lies between these extremes.

If the impurities are in thermal equilibrium, then

$$c = c_0 e^{-W_B/T} \quad (4.2-1)$$

where c_0 is the impurity concentration in the bulk and W_B

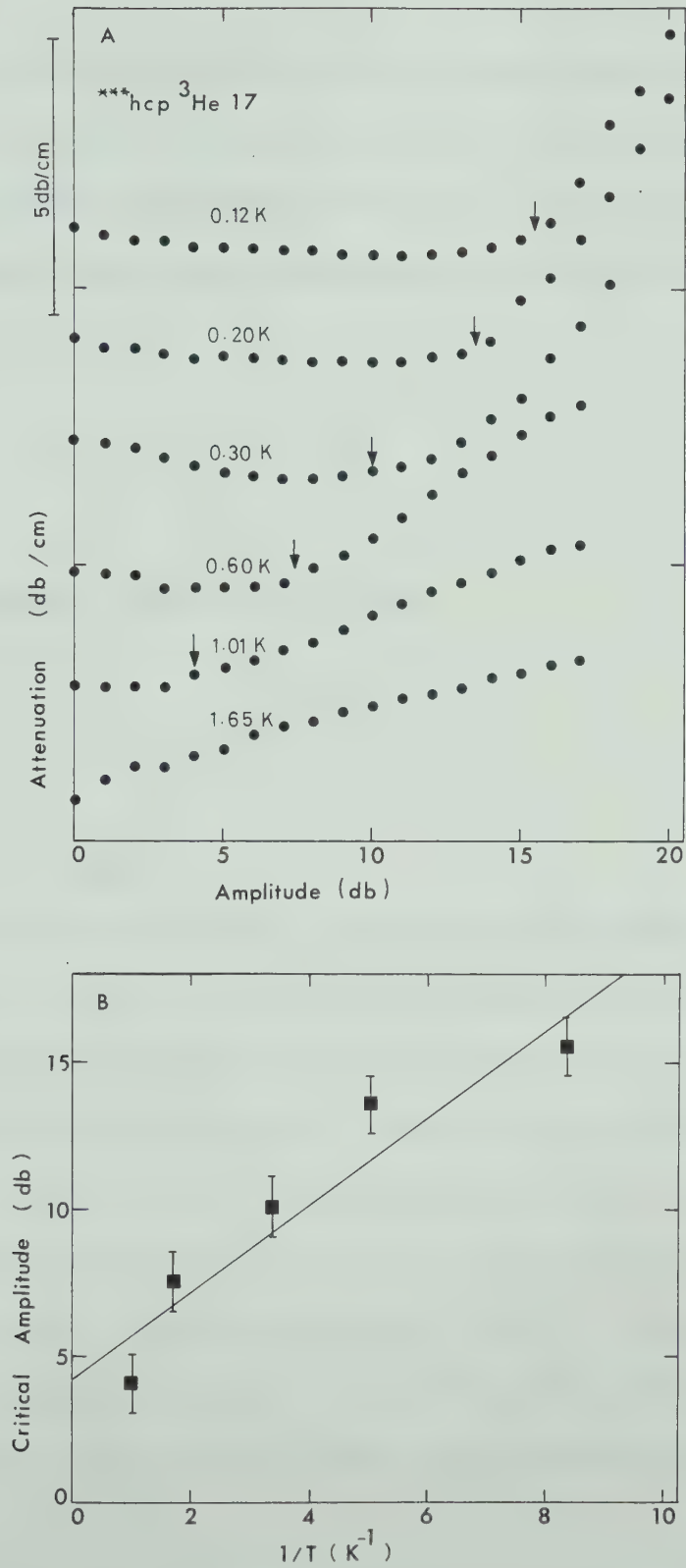


Figure 4.20 Amplitude dependence of attenuation and critical stress in ***hcp ^3He 17.

is the binding energy between the dislocation and impurities.

The breakaway stress is inversely proportional to the pinning length (Granato and Lücke (1956)) and so has a concentration dependence between $c^{1/2}$ and c . Using (4.2-1), the temperature dependence of the breakaway stress lies between

$$\sigma_c \propto c_o^{1/2} e^{-\frac{W_B}{2T}} \quad (4.2-2)$$

for a zigzagging dislocation and

$$\sigma_c \propto c_o e^{-W_B/T} \quad (4.2-3)$$

for a straight one.

In figure 4.20B, the critical pulse amplitudes (in db) are plotted against $1/T$. Although the data are not sufficiently precise to be sure that a linear relationship exists, simply taking a straight line fit gives a slope of 1.5 db-K which corresponds to a binding energy $W_B \approx 170$ mK if equation (4.2-2) is used and $W_B \approx 340$ mK if (4.2-3) is used. Iwasa and Suzuki (1980) found a binding energy for ^3He impurities in hcp ^4He of around 300 mK, assuming that the pinning length was proportional to $c^{-2/3}$.

4.3 bcc ^3He

4.3-1 bcc ^3He 43 (@ 20.1 cm³/mole)

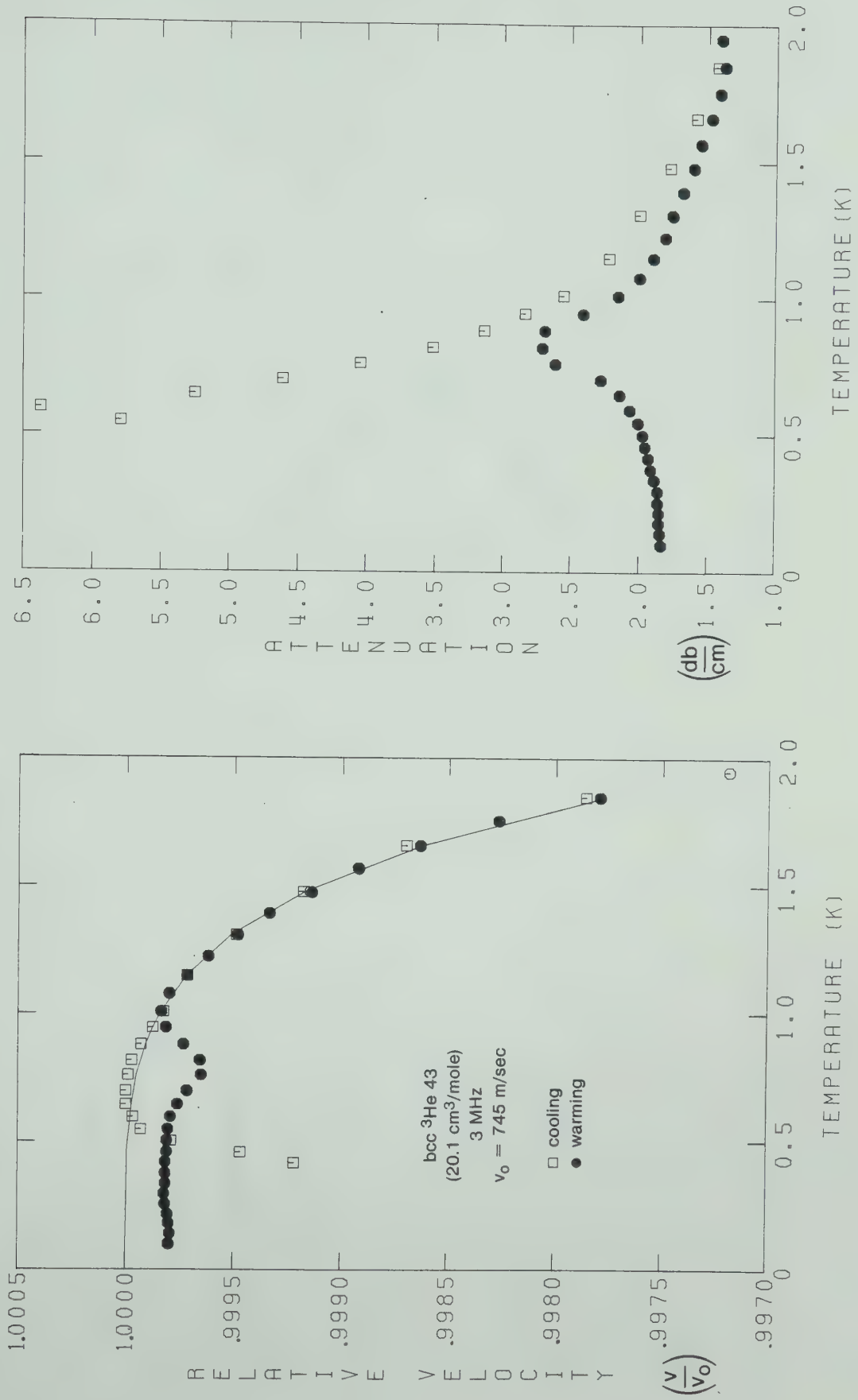
Most of the bcc crystals were grown from pure ^3He (1.35 ppm of ^4He) at 20.1 cm³/mole. As in section 4.2 on hcp ^3He , the results for bcc ^3He are introduced by showing the data from a typical bcc crystal.

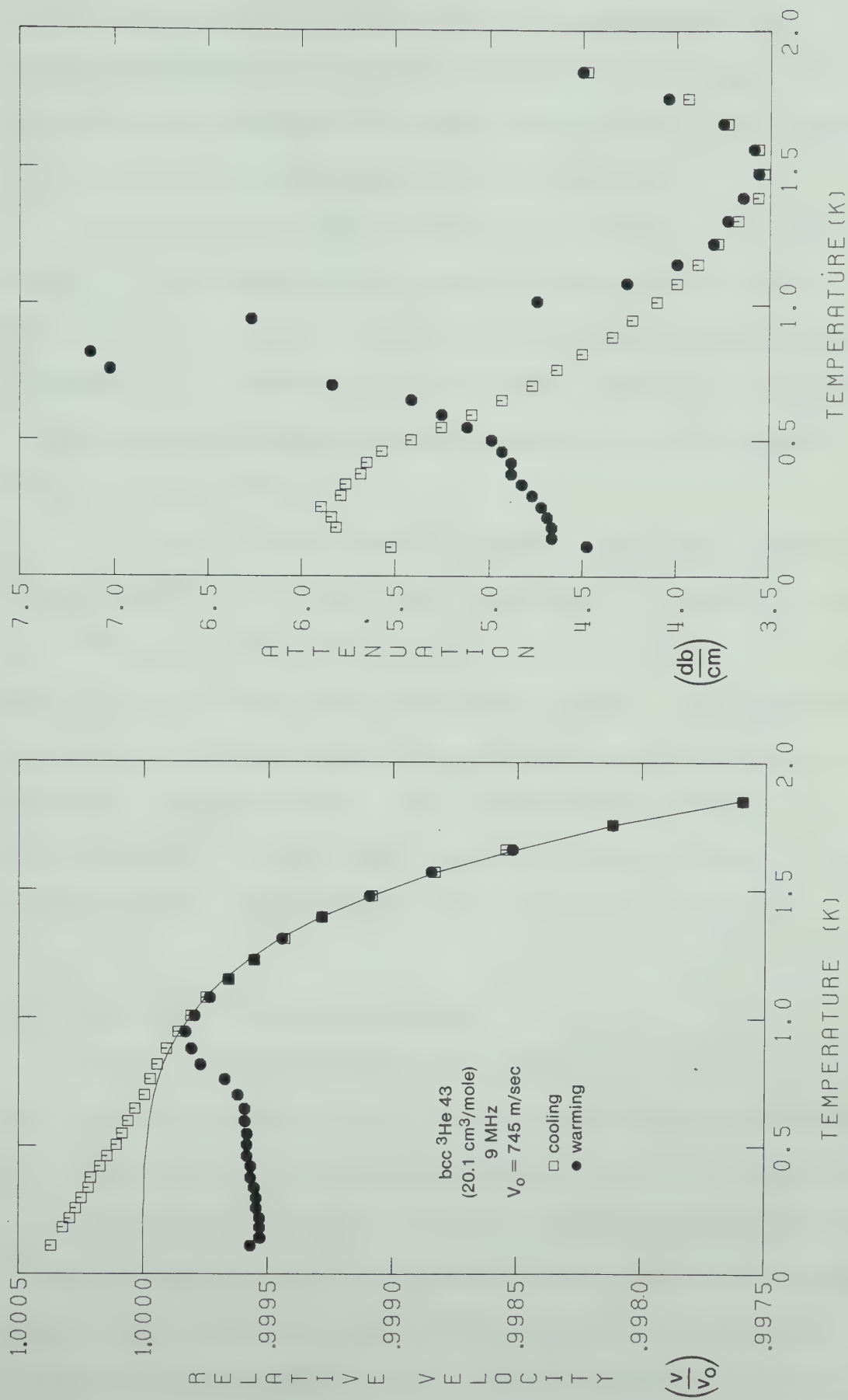
Figures 4.21 and 4.22 show the velocity and attenuation measured in the crystal bcc ^3He 43 at 3 and 9 MHz. Again, open symbols indicate the cooling data while the solid symbols are the warming data.

The data during cooling showed an anomaly very much like that seen in hcp ^3He . The velocity anomaly was negative at 3 MHz, positive at 9 MHz and at both frequencies was accompanied by an increase in attenuation.

Before the warming data were taken, the crystal was held at about 200 mK and the 3 MHz pulse amplitude was increased by 12 db (from its measuring amplitude which corresponded to a stress of about 200 Nt/m²). About 6×10^4 high amplitude pulses were applied before the amplitude was reduced. The result was that the size of the negative 3 MHz velocity anomaly decreased as did the attenuation. As in hcp ^3He , applying 9 MHz pulses to the crystal had no effect but the large 3 MHz pulses changed the 9 MHz velocity anomaly from positive to negative and reduced the attenuation.

Although no systematic study was made of the effects

Figure 4.21 v and α in bcc $^3\text{He } 43$ @ 3 MHz

Figure 4.22 v and α in bcc $^3\text{He } 43$ @ 9 MHz

of the high amplitude pulses at low temperature, the general features were similar to the hcp ^3He case. That is, the effect was greater for lower temperatures, for larger pulses and for higher pulse repetition rates.

On warming, v and α recovered to their original values in the temperature range between 0.6 and 0.9 K. This recovery was also thermally activated and is discussed in section 4.6. Note that the 9 MHz attenuation overshoot its cooling value during the recovery, an effect never observed in hcp ^3He .

In view of the almost complete similarity between hcp and bcc ^3He , the data were analysed in the same manner.

Figure 4.23 shows the results of fitting the anomaly found on cooling to the dislocation theory. The velocity fit is fair and the resulting attenuation is in qualitative agreement with the data. The values of $RA(1.96 \times 10^7 \text{ m}^{-2})$ and $L(9.38 \times 10^{-6} \text{ m})$ are comparable to those in hcp ^3He and the damping $B(2.70 \times 10^{-8} \text{ T}^3 \text{ mks})$ is slightly larger.

4.3-2 bcc ^3He (@ $20.1 \text{ cm}^3/\text{mole}$)

Only one other crystal of pure ^3He at this density had a complete set of data, although partial measurements on several others agreed qualitatively with this crystal.

Figure 4.24 shows the anomaly and dislocation fits in the crystal bcc ^3He 36. The fit was made to the 9 MHz data and the fits at 3 and 21 MHz are qualitatively in agreement with the data as are the attenuation curves using

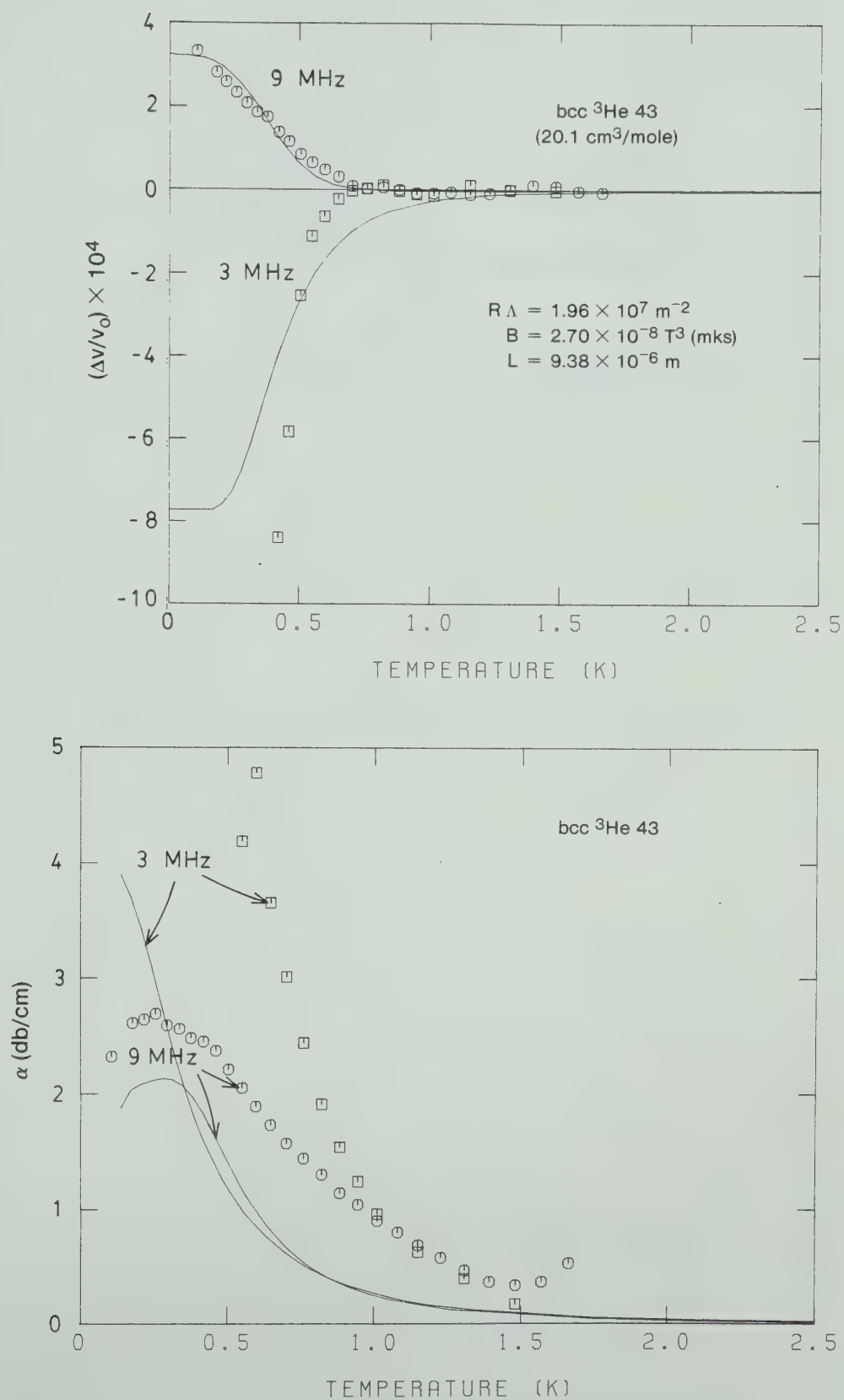


Figure 4.23 Dislocation fits (3 and 9 MHz) of v and α for bcc ^3He 43.

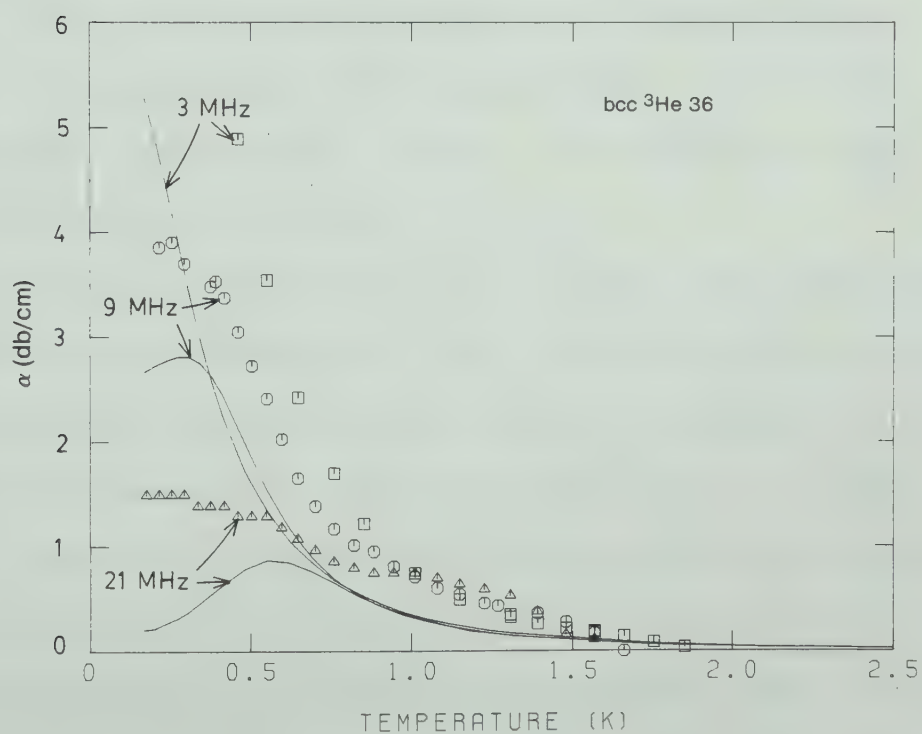
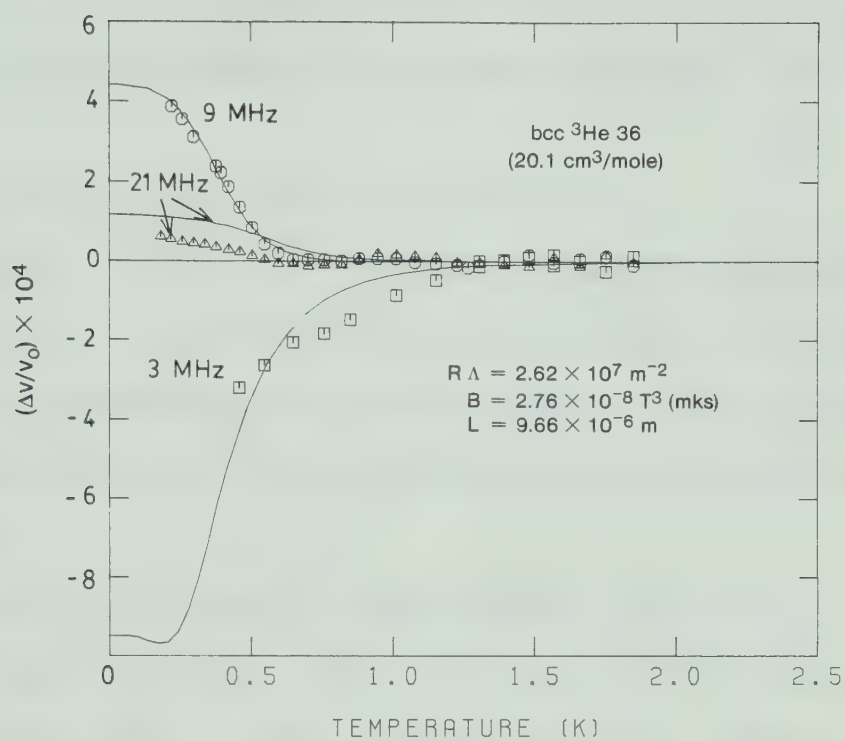


Figure 4.24 Dislocation fits (3, 9 and 21 MHz) of v and α for bcc ^3He 36.

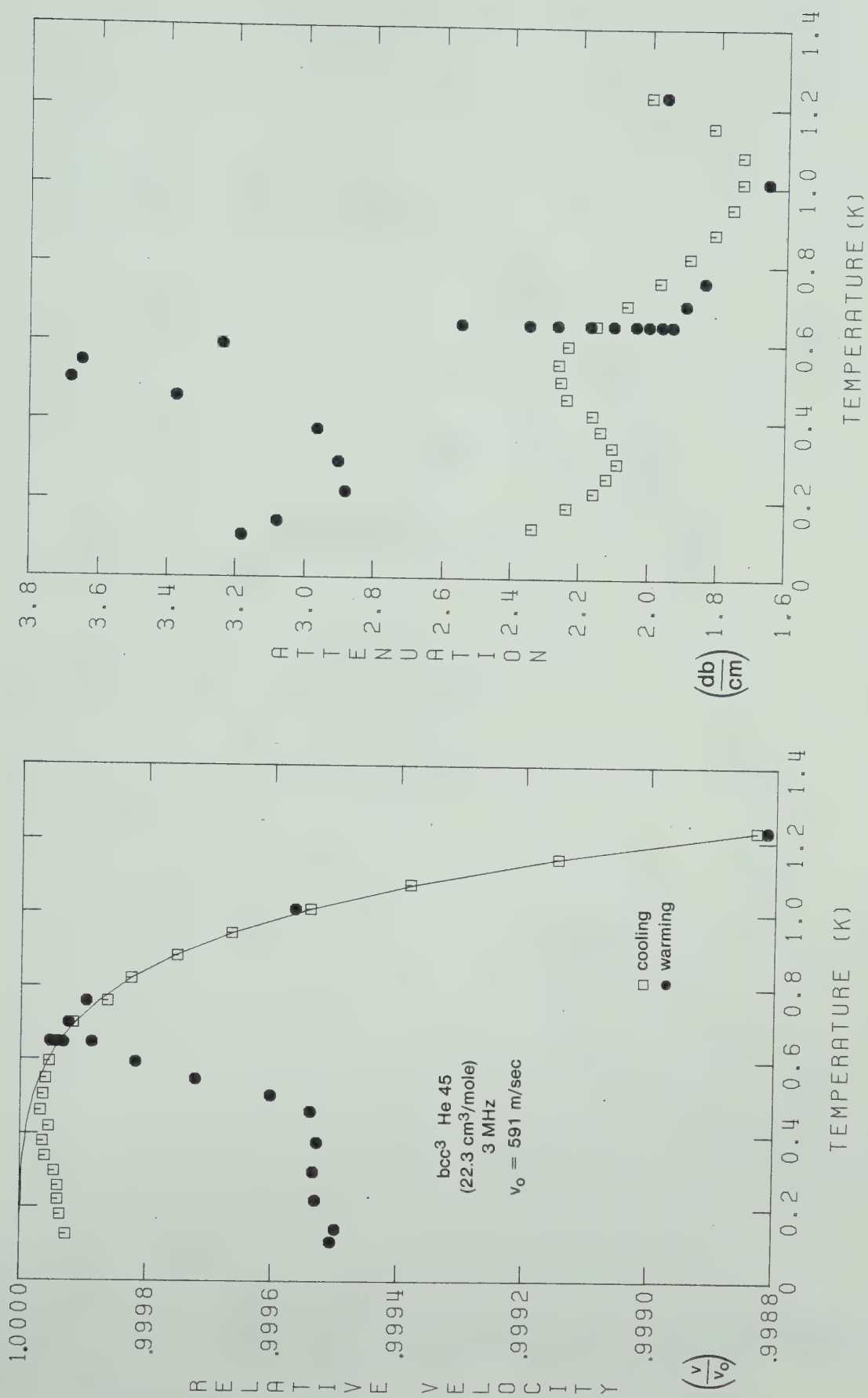
the parameters from the velocity fit. The values of RA ($2.62 \times 10^7 \text{ m}^{-2}$), B ($2.76 \times 10^{-8} \text{ T}^3 \text{ mks}$) and L ($9.66 \times 10^{-6} \text{ m}$) are in excellent agreement with those from bcc ^3He 43.

4.3-3 bcc ^3He (@ 22.3 and 24.2 cm^3/mole)

Crystals of pure bcc ^3He were grown at two lower densities of 22.3 and 24.2 cm^3/mole . At 22.3 cm^3/mole , the anomaly observed during cooling was smaller than in bcc ^3He at 20.1 cm^3/mole and at 24.2 cm^3/mole it had essentially disappeared.

Figure 4.25 shows the data taken on bcc ^3He 45 (22.3 cm^3/mole) at 3 MHz. The data taken during cooling (open symbols) show a small negative velocity anomaly below about 0.6 K. The cooling velocity at 9 MHz (figure 4.26) shows no anomaly within the experimental resolution. Due to the small size of the anomaly, no attempt was made to fit to dislocation theory.

At a temperature of about 120 mK, the 3 MHz pulse amplitude was increased by 10 db. When the pulse amplitude was increased, the attenuation began to increase and the velocity to decrease. After the application of about 10^5 pulses, the amplitude was reduced and the crystal warmed (solid symbols). At around 0.6 K, the velocity and attenuation recovered to their cooling values and when the crystal was cooled again the cycle was reproduced. The large 3 MHz pulses had a similar effect on the 9 MHz velocity (figure 4.26).

Figure 4.25 v and α in bcc ³He45 (22.3 cm³/mole) @ 3 MHz

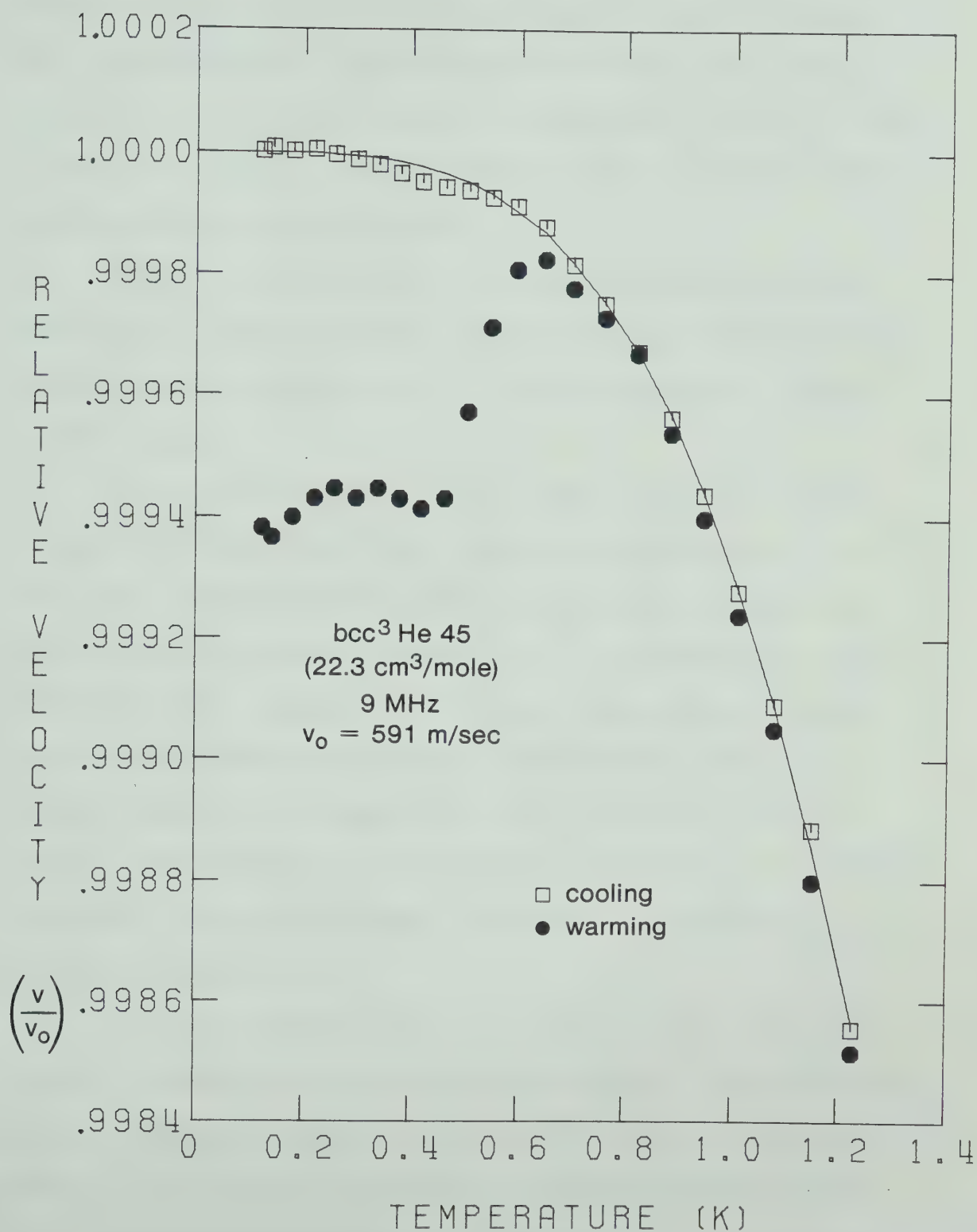


Figure 4.26 v in bcc ³He (22.3 cm³/mole) @ 9 MHz

This creation of a larger velocity and attenuation anomaly by the high amplitude pulses is quite different from the results at higher densities where the anomaly always decreased when pulses were applied. It may be due to the low density of the crystals since a similar effect was observed at $24.2 \text{ cm}^3/\text{mole}$.

Whatever the effect of the large pulses at this density, it also exhibited a thermally activated recovery, in this case at about 0.6 K. This is examined in detail in section 4.6.

The results for a crystal grown at $24.2 \text{ cm}^3/\text{mole}$ (figures 4.27 and 4.28) are similar to those at $22.3 \text{ cm}^3/\text{mole}$. The total velocity changes were quite small and, within the experimental resolution, no anomaly was observed during cooling. Again, the large 3 MHz pulses created a negative velocity anomaly and increased the attenuation. Warming above 0.5 K restored v and α to their original values. The effect of large 3 MHz pulses on the 9 MHz data was small, with only a small hysteresis appearing in α between 150 and 500 mK.

Although no velocity anomaly was observed at 3 MHz and the attenuation decreased below 400 mK, the measuring pulses themselves may have been sufficient to eliminate any anomaly. When the crystal was cooled from near melting with the ultrasonic pulses off and then, at the lowest temperature of around 100 mK the pulses were turned on, the attenuation was initially about 1 db/cm higher than the

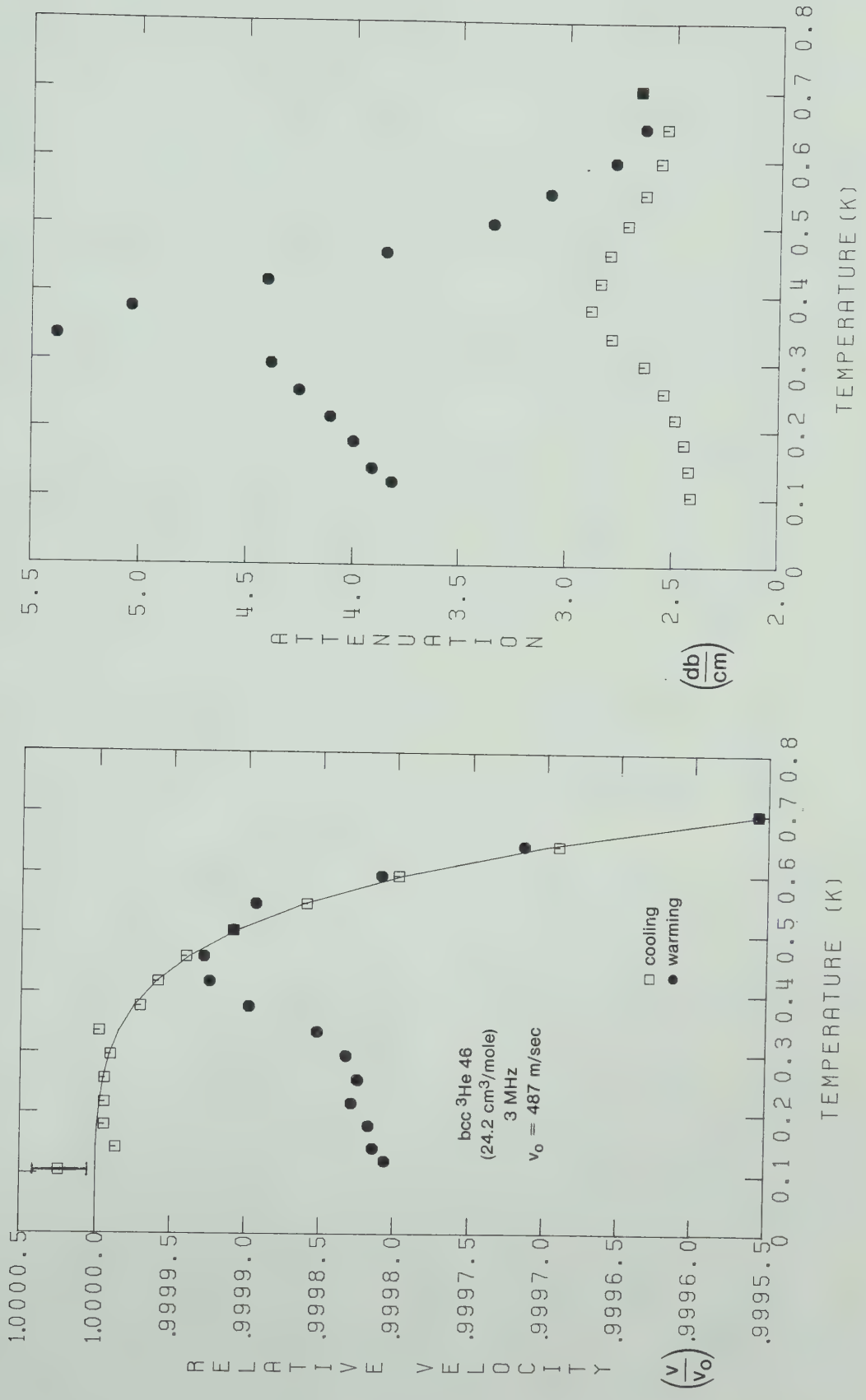
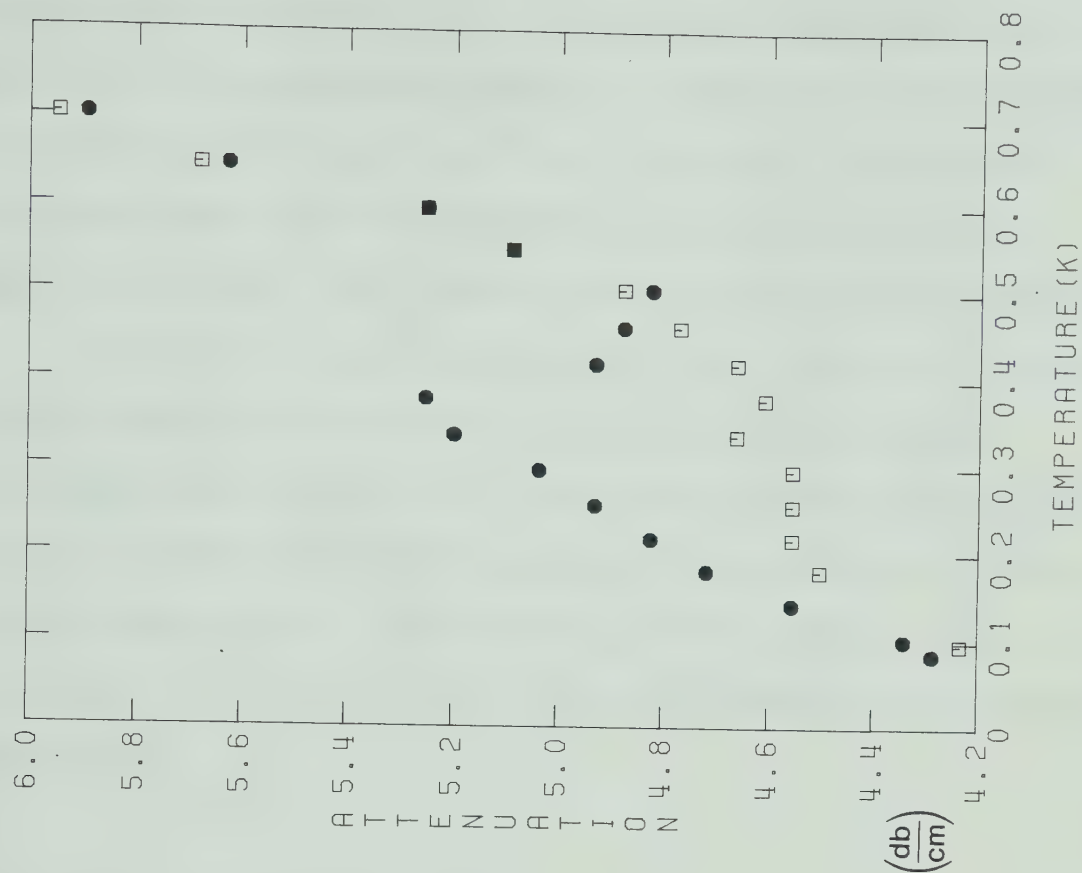
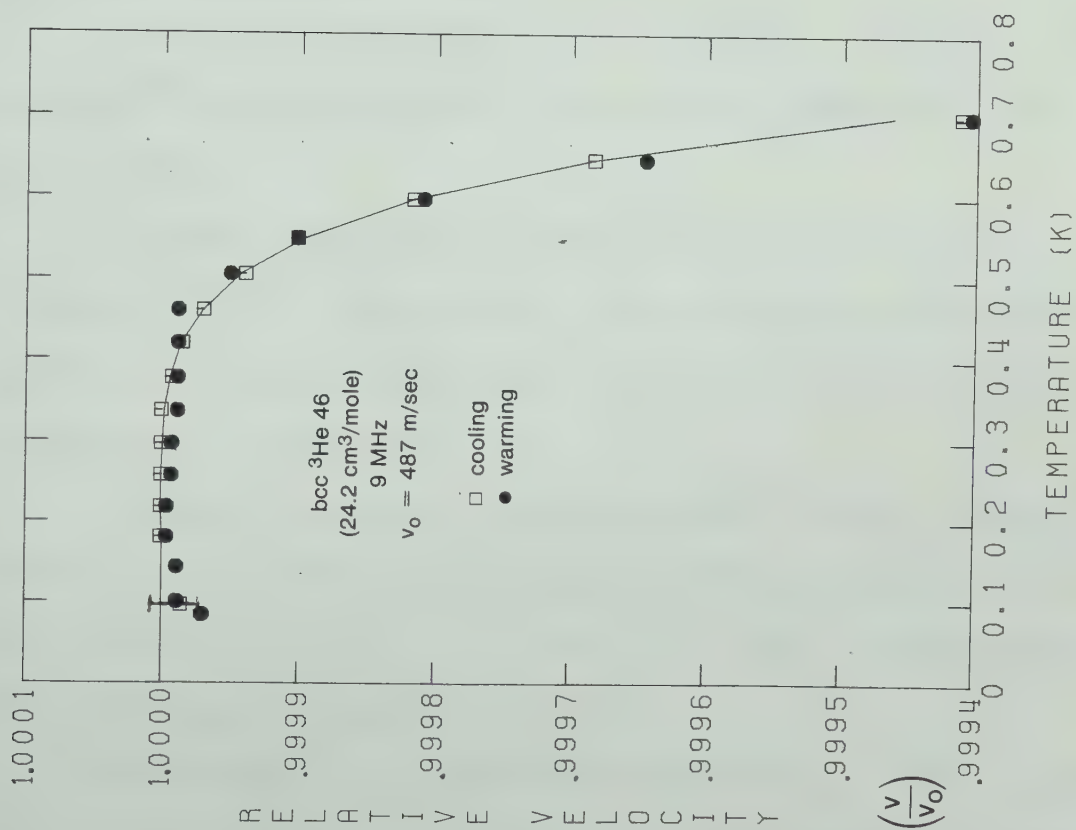


Figure 4.27 v and α in bcc ^3He 46 (24.2 cm³/mole) @ 3 MHz

Figure 4.28 v and α in bcc ^3He 46 (24.2 cm^3/mole) @ 9 MHz

value when the crystal was cooled with the pulses on. As soon as the pulses were turned on, the attenuation started to decrease, reaching its final value in a few minutes. This indicates that measurements at much lower pulse amplitudes might have shown an anomaly due to dislocations.

Incomplete measurements on a few crystals at intermediate densities (around 21 and 23 cm³/mole) also indicated that the size of the cooling anomaly decreased as the density decreased, until at 22.3 cm³/mole it was barely resolvable. The increase in the anomaly at low densities due to the high amplitude pulses is not presently understood.

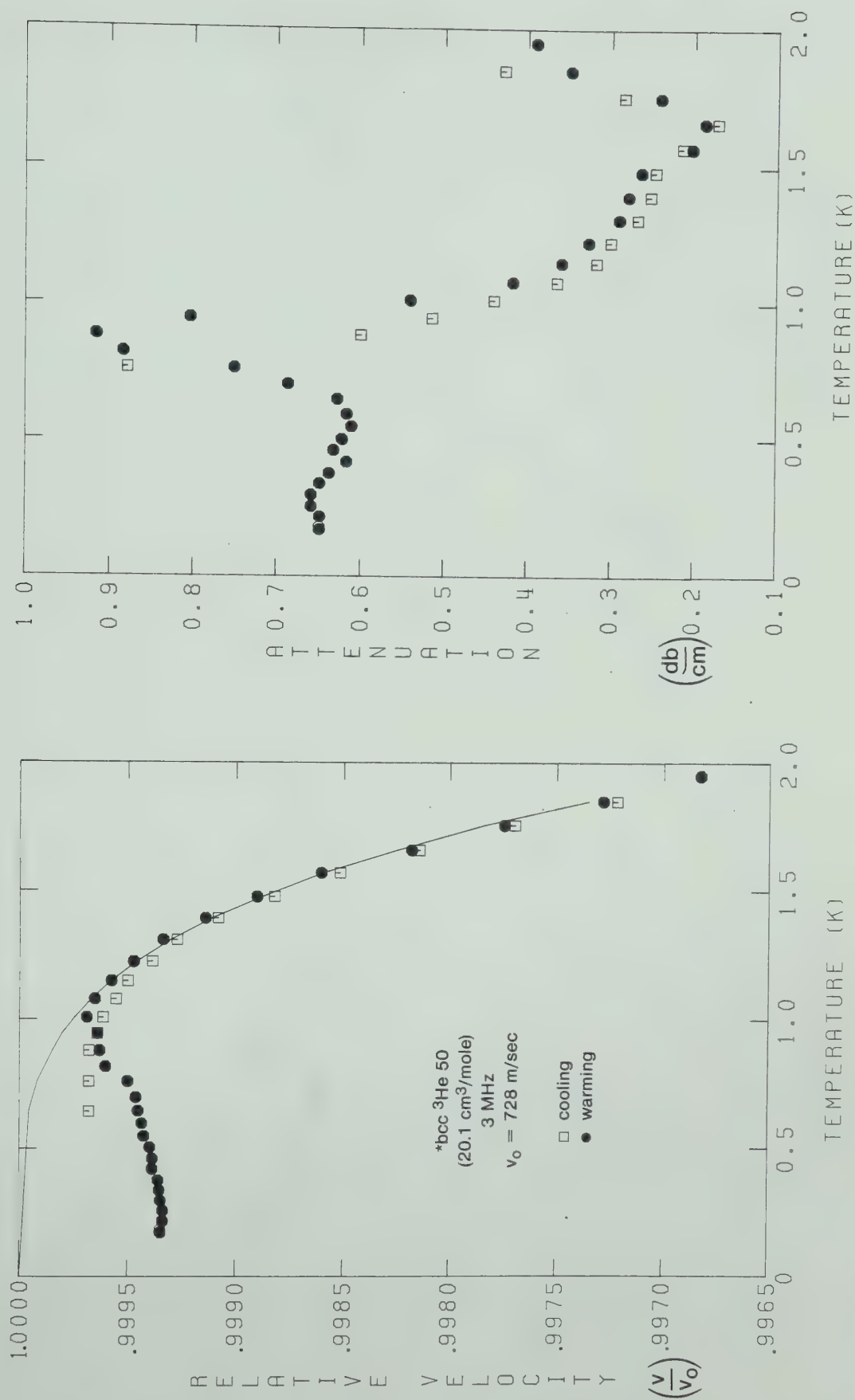
4.3-4 Effects of Impurities

Crystals were grown at 20.1 cm³/mole from gas with the same ⁴He concentrations (47 ppm, 430 ppm and 0.53%) as for hcp ³He.

Figures 4.29 and 4.30 show v and α in *bcc ³He 50 (47 ppm of ⁴He). The anomaly, the effect of high amplitude pulses and the high temperature recovery were essentially the same as in pure bcc ³He.

Figure 4.31 shows the dislocation fit to the cooling anomaly. The dislocation parameters ($RA = 5.86 \times 10^7 \text{ m}^{-2}$, $B = 2.21 \times 10^{-8} \text{ T}^3 \text{ mks}$, $L = 7.18 \times 10^{-6} \text{ m}$) are in good agreement with those for pure crystals.

The results of adding 430 ppm of ⁴He to the crystals are shown in figures 4.32 and 4.33. The anomaly on cooling

Figure 4.29 v and α in ***bcc ^3He 50 (47 ppm ^4He) @ 3 MHz

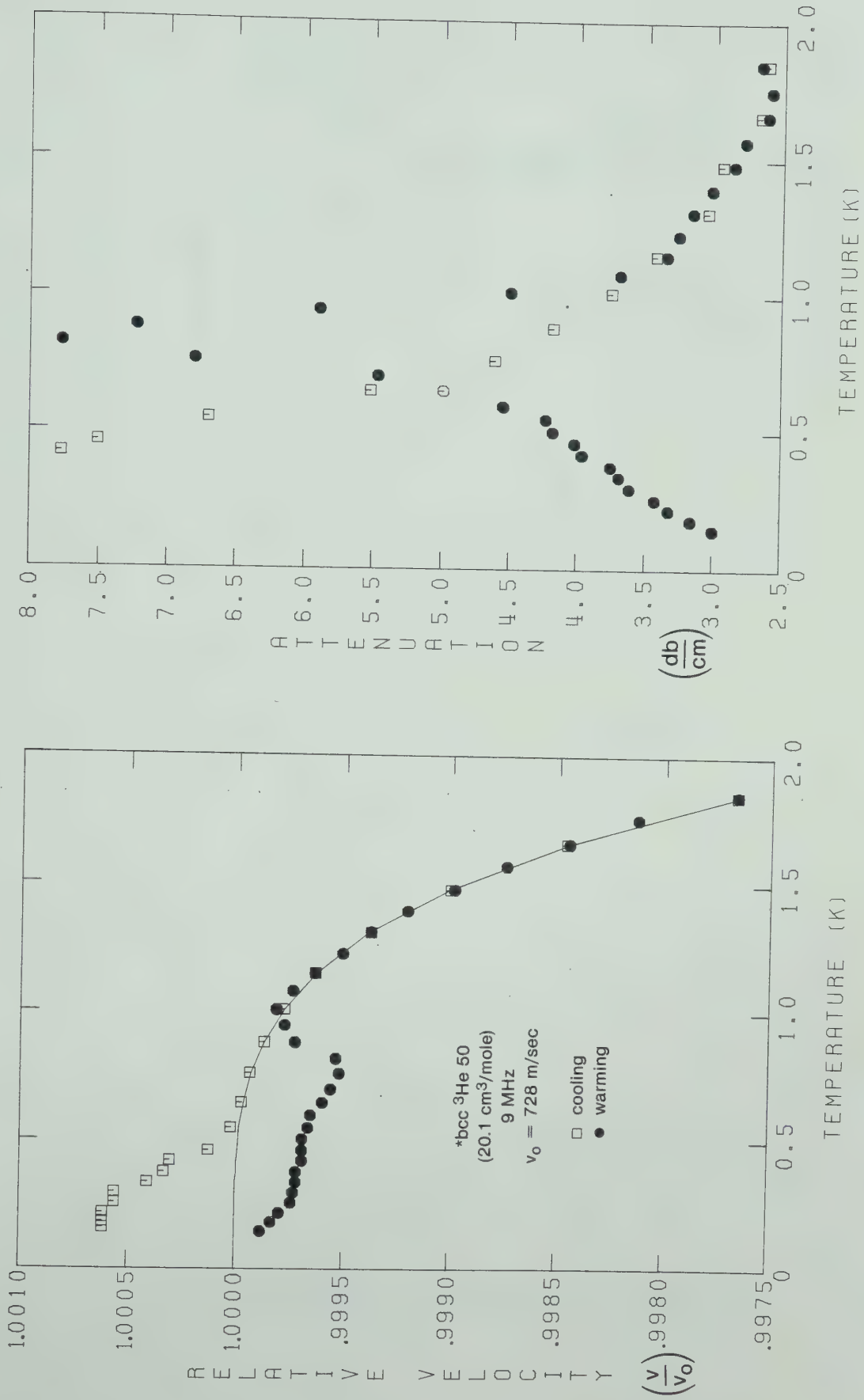


Figure 4.30 v and α in *bcc ^3He 50 (47 ppm ^4He) @ 9 MHz

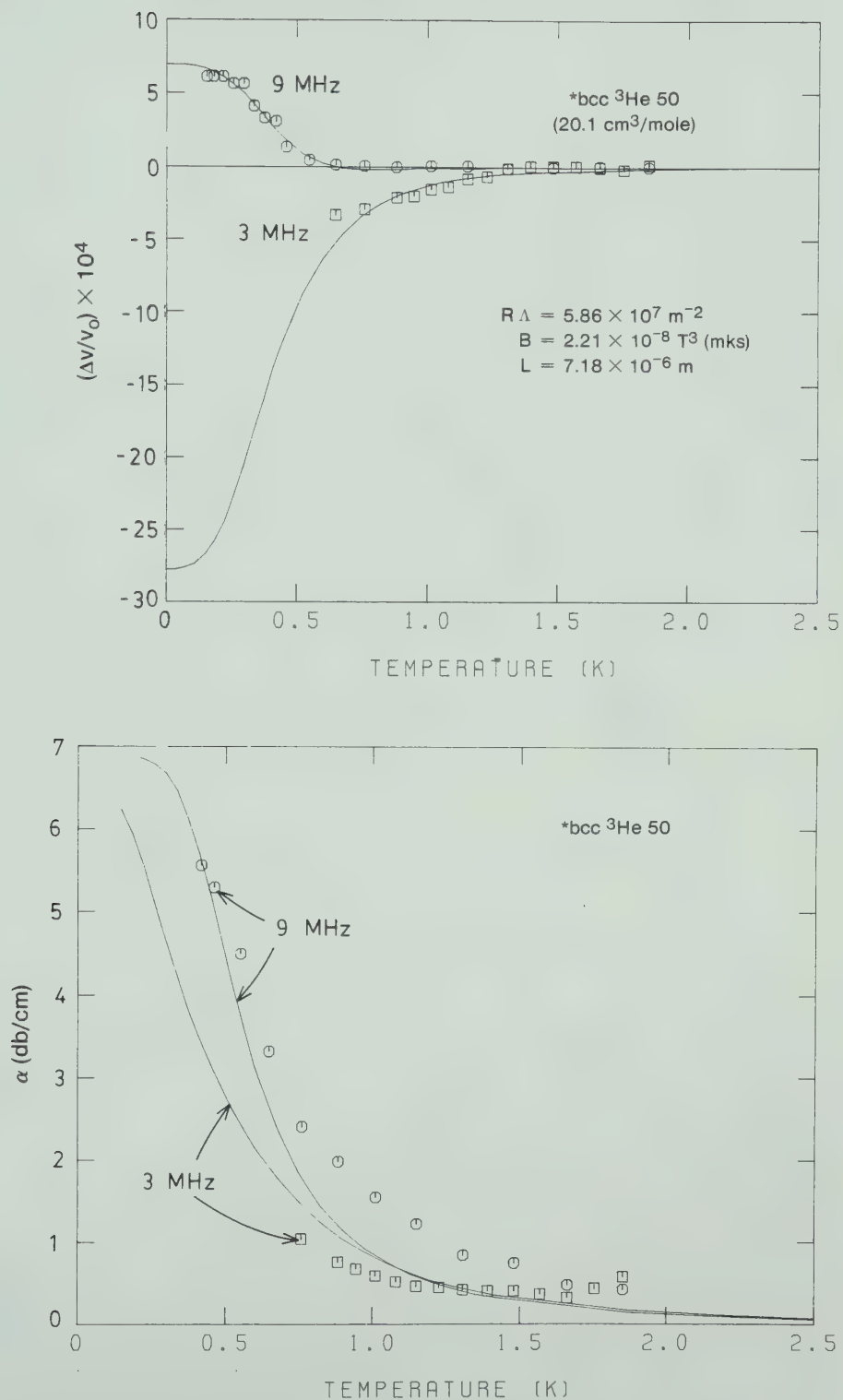
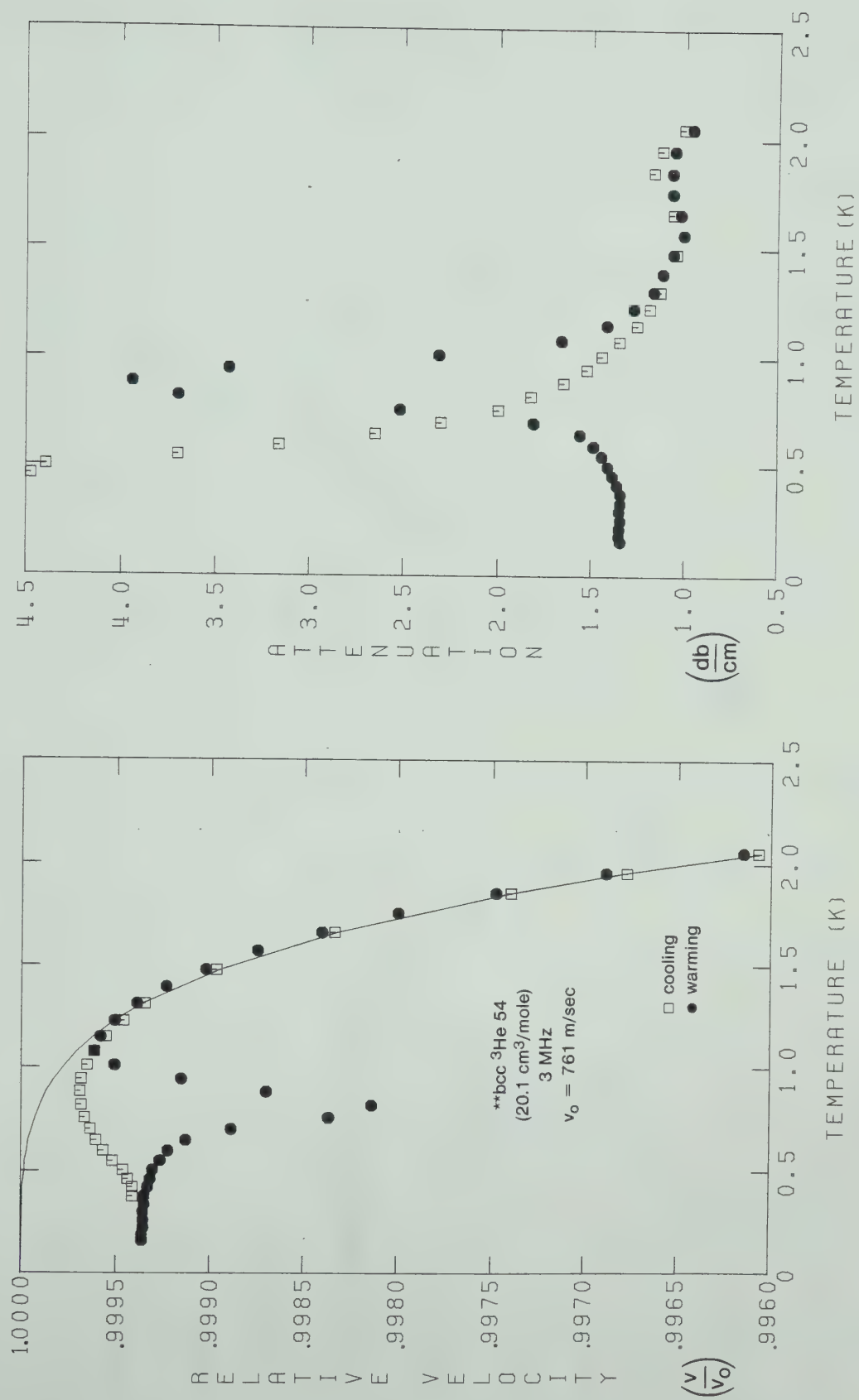
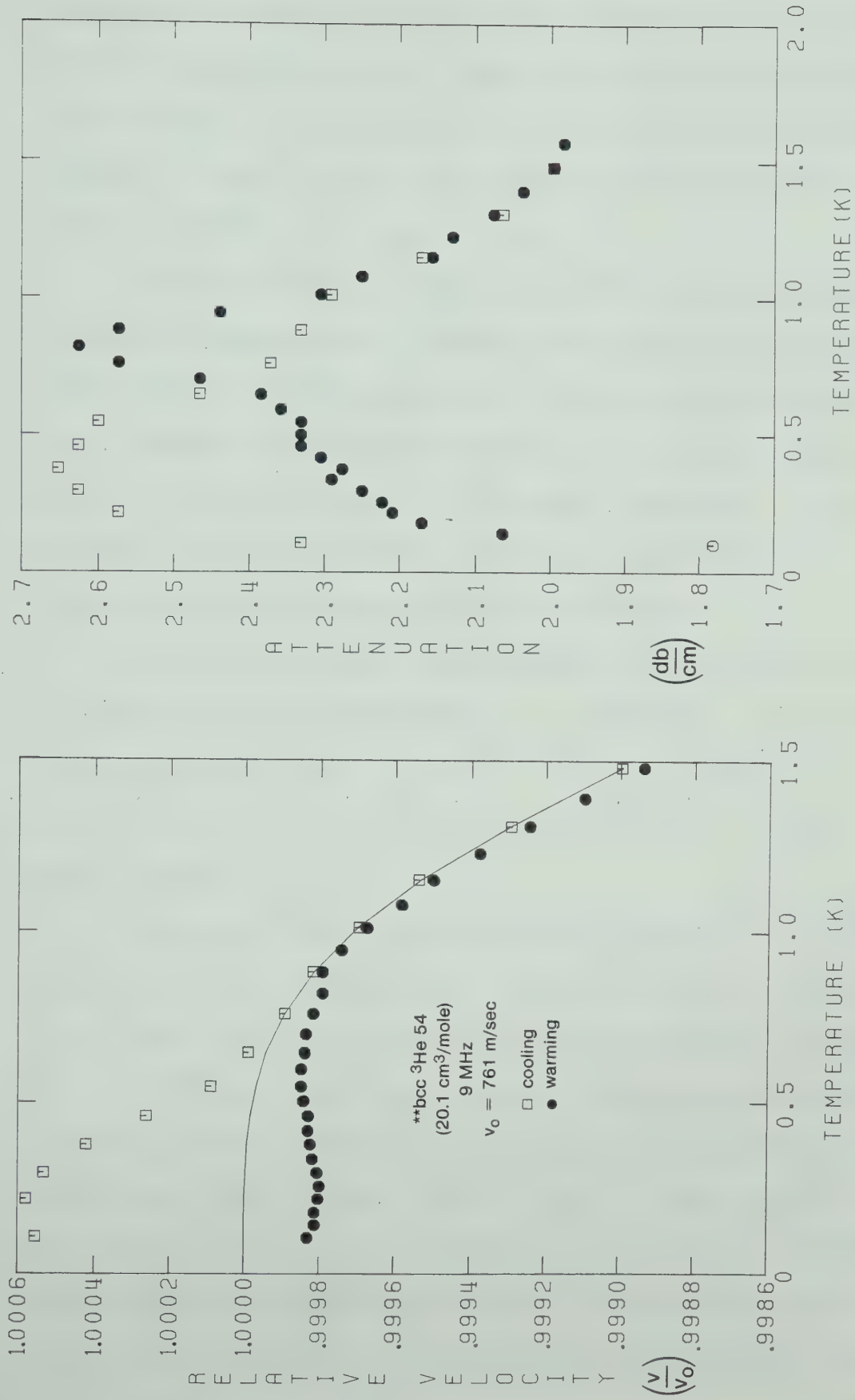


Figure 4.31 Dislocation fits (3 and 9 MHz) of v and α for * bcc ^3He 50 (47 ppm ^4He).

Figure 4.32 v and α in **bcc ^3He 54 (430 ppm ^4He) @ 3 MHz

Figure 4.33 v and α in **bcc ^3He 54** (430 ppm ^4He) @ 9 MHz

did not appear to be affected but during warming the high temperature recovery appeared as a large dip in the 3 MHz velocity accompanied by a large peak in the attenuation. This may not be significant but may merely be a larger version of the dip in v and peak in α seen in the pure crystal bcc ^3He 43 (figure 4.21).

In this crystal, when about 10^3 high amplitude 3 MHz pulses were applied at 150 mK, the anomaly changed to the form shown by solid symbols in figures 4.32 and 4.33. This compares to the approximately 10^5 pulses required to produce the same effect in the purer crystals. It thus appears that, in bcc ^3He , the impurities help to pin the dislocations at concentrations of 430 ppm.

Figure 4.34 shows the anomaly in **bcc ^3He 54 during cooling and the dislocation fit to the data. The dislocation parameters ($RA = 3.12 \times 10^7 \text{ m}^{-2}$, $B = 2.23 \times 10^{-8} \text{ T}^3 \text{ mks}$, $L = 1.30 \times 10^{-5} \text{ m}$) again agree quite well with those in pure crystals.

As in hcp ^3He , the addition of 0.53% ^4He to the ^3He greatly reduced the anomaly. Figures 4.35, 4.36 and 4.37 show v and α at 3, 9 and 21 MHz in the crystal ***bcc ^3He 56 (0.53% ^4He). At 9 and 21 MHz there was neither an anomaly nor any hysteresis due to the application of high amplitude 3 MHz pulses. In contrast to the hcp ^3He case, there remained a small anomaly at 3 MHz which was eliminated by the high amplitude 3 MHz pulses with a resulting hysteresis in v and α . The amplitude dependence seen in

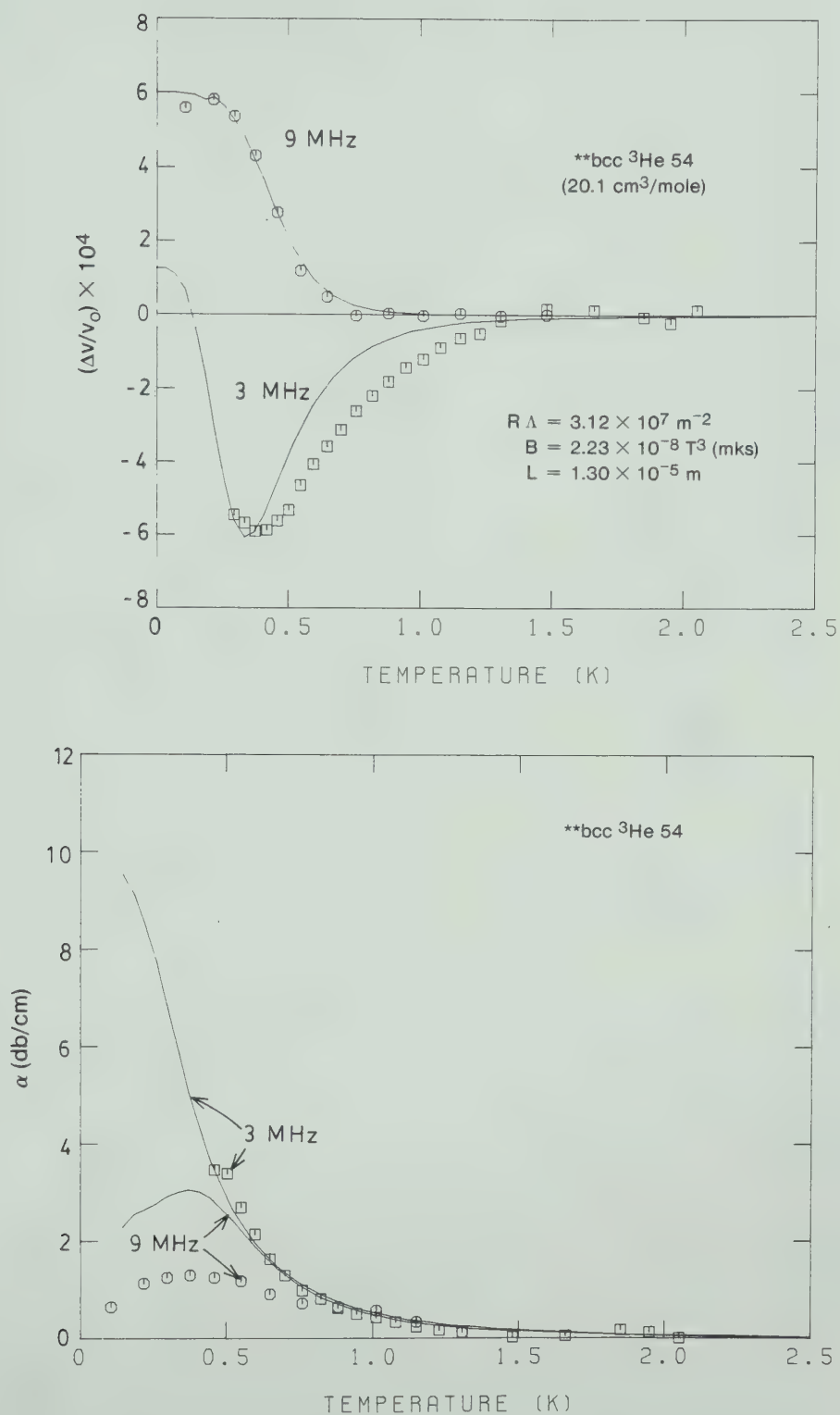
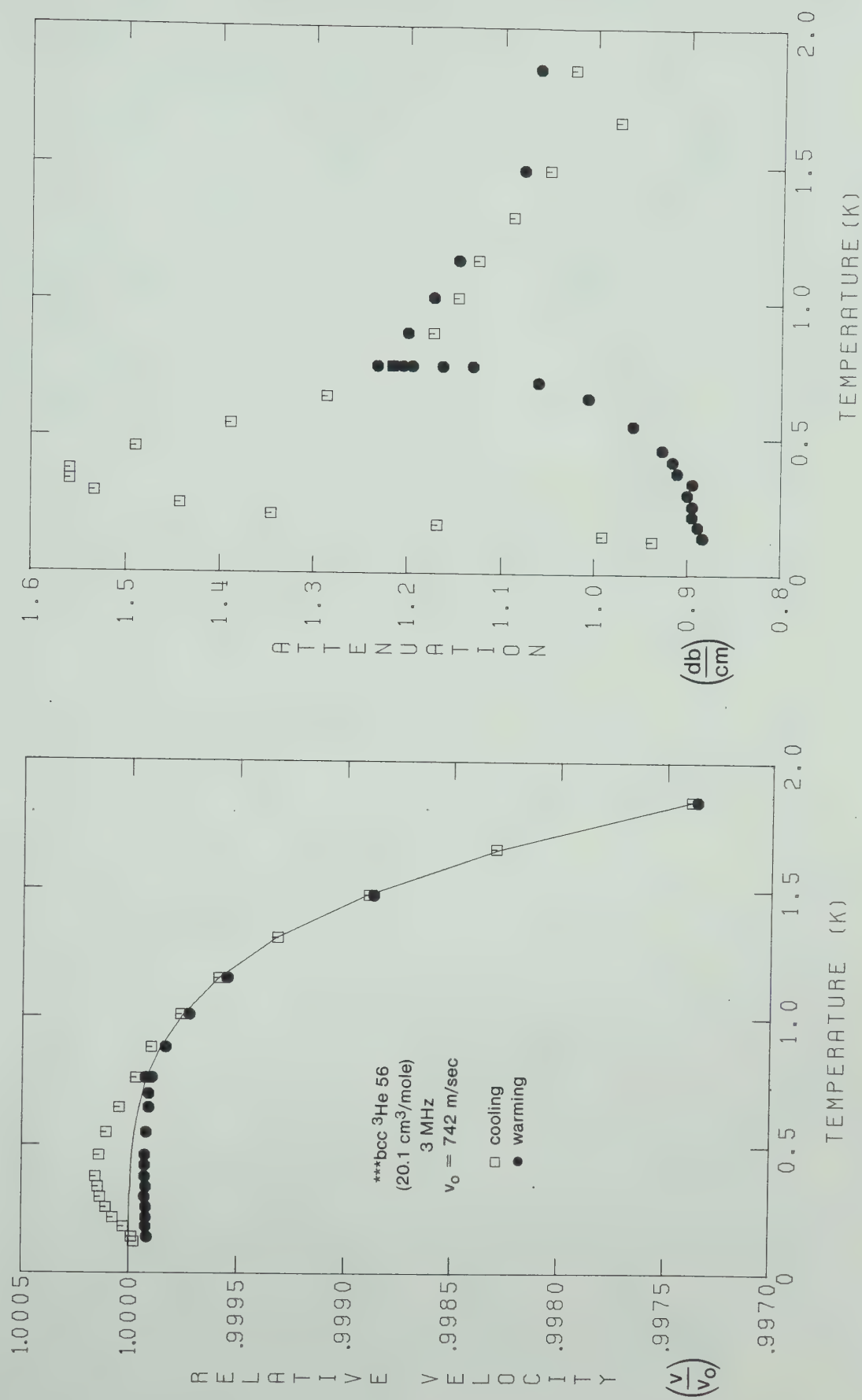


Figure 4.34 Dislocation fits (3 and 9 MHz) of v and α for **bcc ^3He 54 (430 ppm ^4He).

Figure 4.35 v and α in ***bcc ^3He 56 (0.53% ^4He) @ 3 MHz

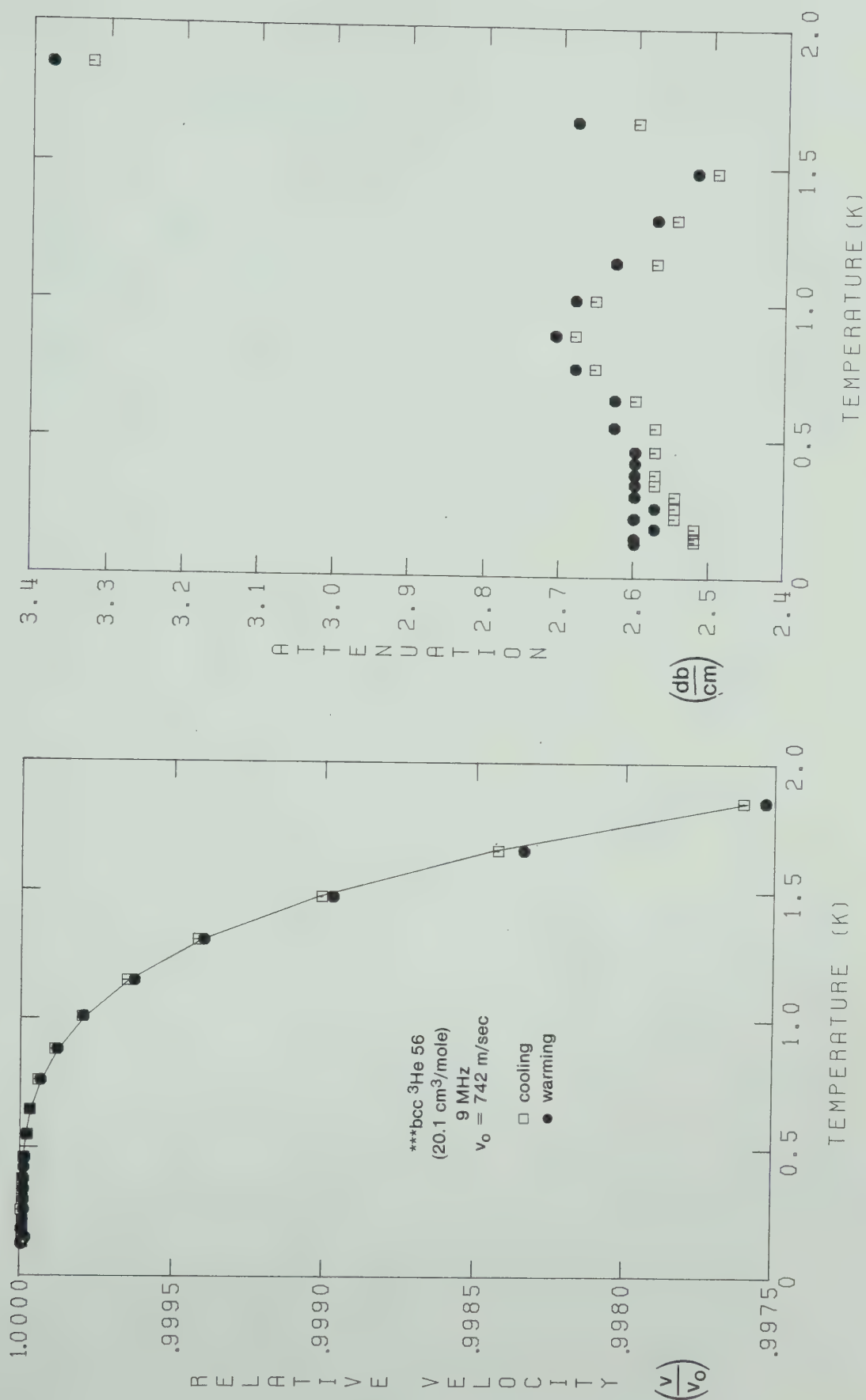
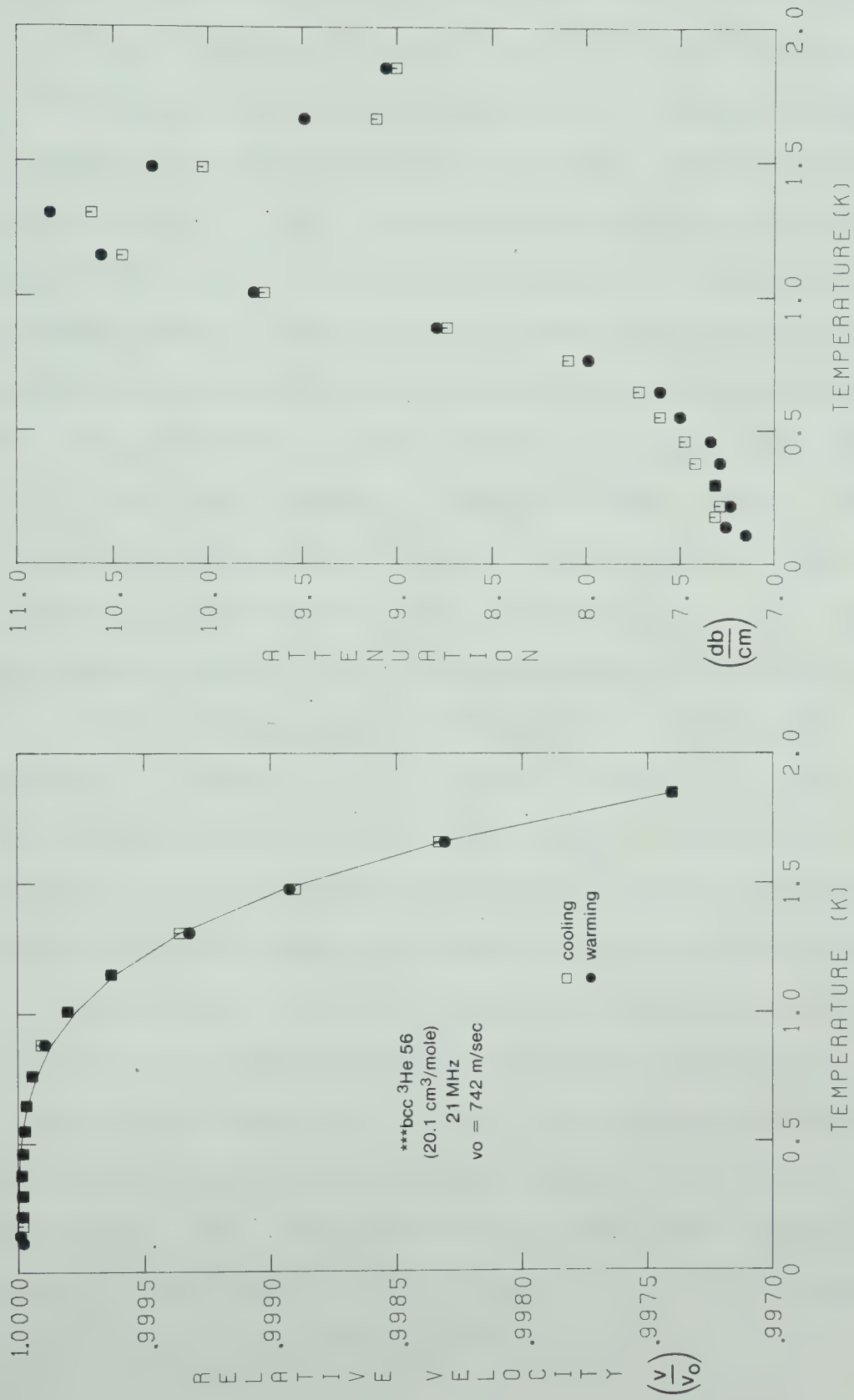


Figure 4.36 v and α in ***bcc ^3He 56 (0.53% ^4He) @ 9 MHz

Figure 4.37 v and α in ***bcc ^3He 56 (0.53% ^4He) @ 21 MHz

***hcp ^3He 17 (figure 4.20) was not studied in this crystal although there were some indications that it existed.

One crystal was grown from the 0.53% ^4He gas at 24.2 cm^3/mole . No anomaly was observed at 3 MHz when the crystal was cooled to 150 mK. However, when the sample cooled below 125 mK, the attenuation began to increase. By warming above 125 mK, the attenuation could be made to decrease again. There was no measurable change in the sound velocity associated with the changes in attenuation. The time constant for the changes was quite long. When the crystal was cooled to 100 mK and kept there, the attenuation was still changing after an hour. When the crystal was then warmed, the attenuation did not return to its cooling value until the temperature reached 600 mK.

This effect can be attributed to the isotopic phase separation (Edwards et al. (1962) and Mullin (1968)) expected at about 140 mK. Iwasa et al. (1981) observed a change in the amplitude dependence of the attenuation below the phase separation temperature in dilute solutions of ^4He in ^3He . They attributed the increase to a multiplication of dislocations during the phase separation. Greenberg and Armstrong (1980) have observed hysteresis in the low temperature thermal conductivity of bcc ^3He containing ^4He . They also interpreted their results in terms of dislocations which nucleated the ^4He clusters formed during the phase separation.

4.4 hcp ^4He

4.4-1 hcp ^4He 1 ($17.7 \text{ cm}^3/\text{mole}$)

Crystals of hcp ^4He were grown in order to provide a comparison to the ^3He results and to previous work on hcp ^4He . In particular, since the hysteresis due to high amplitude 3 MHz pulses had not previously been observed in ^4He , it was possible that this was an isotopic effect. The pure ^4He crystals were grown from Matheson purity ^4He . This was not analysed for ^3He content but probably contained less than 1 ppm of ^3He .

Figures 4.38 and 4.39 show the data at 3 and 9 MHz from the crystal hcp ^4He 7 ($17.7 \text{ cm}^3/\text{mole}$). The data taken during cooling (open symbols) show a velocity anomaly which is negative at 3 MHz and positive at 9 MHz, accompanied by a large attenuation. These features are in agreement with previous work on hcp ^4He (e.g. Calder (1977)) and with the results on ^3He .

Between the cooling data and that taken on warming (solid symbols), the pulse amplitude was increased from its measuring value (corresponding to a stress $\sim 200 \text{ Nt/m}^2$) by 12 db and 10^5 pulses were applied. The effect on the anomaly was very similar to the ^3He case, namely a reduction of the 3 MHz anomaly, a change of the 9 MHz velocity anomaly from positive to negative and a decrease in the attenuation at both frequencies. The pulse amplitude dependent effect thus is common to both isotopes.

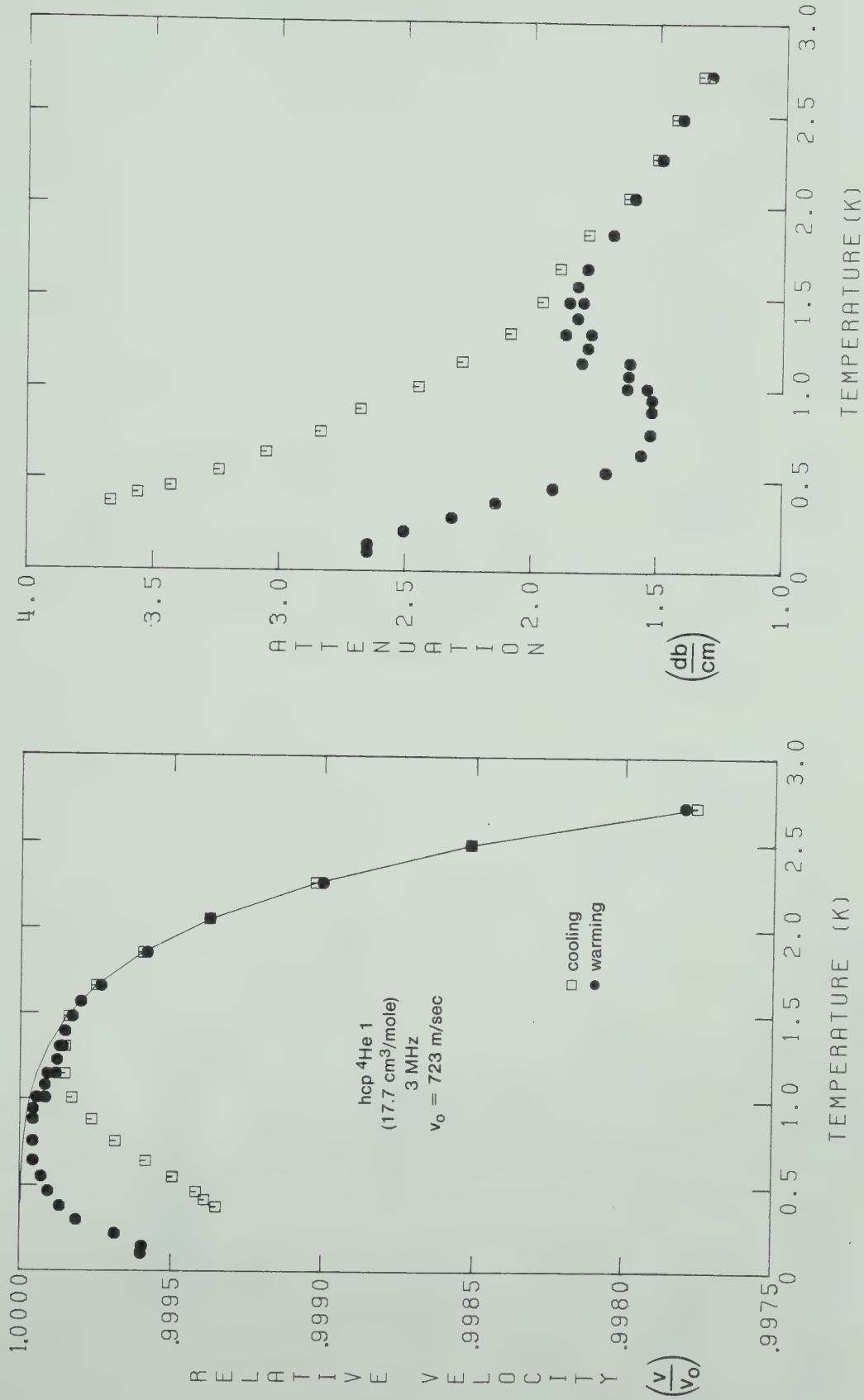


Figure 4.38 v and α in hcp ^4He 1 (17.7 cm³/mole) @ 3 MHz

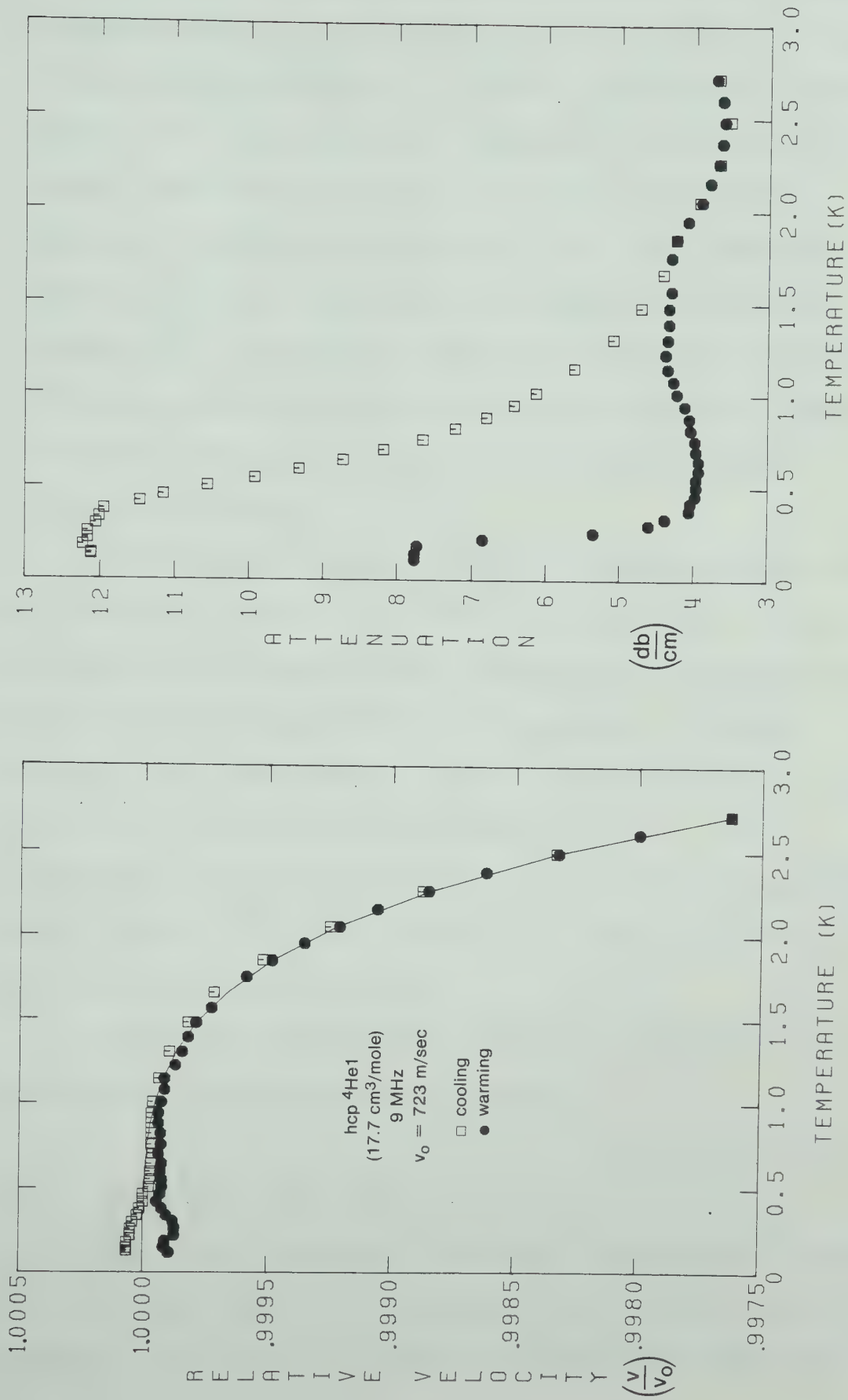


Figure 4.39 v and α in hcp $^4\text{He1}$ (17.7 cm³/mole) @ 3 MHz

The rather rapid decrease in α between 100 and 500 mK during warming which can be seen in figures 4.38 and 4.39 may be significant. It was not associated with the recovery of v and α to their original values since on cooling from 500 mK back to 100 mK the attenuation increased, showing no hysteresis. The time dependent recovery of v and α occurred at a higher temperature around 1.5 K. To explain the change in v and α below 500 mK during warming in terms of dislocations would require a damping much greater than that indicated from the anomaly on cooling.

The cooling anomaly and the dislocation theory fit are shown in figure 4.40. The velocity data fit quite well but the attenuation is considerably larger than that predicted using the dislocation parameters from the velocity fit. The general form of the dislocation predictions for α and the ratio between the 3 and 9 MHz attenuation agree with the data. The dislocation parameters ($RA = 2.69 \times 10^7 \text{ m}^{-2}$, $B = 2.24 \times 10^{-8} \text{ T}^3 \text{ mks}$, $L = 3.80 \times 10^{-6} \text{ m}$) are similar to those in ^3He .

The other crystal grown from pure ^4He showed a similar but slightly smaller anomaly.

4.4-2 hcp ^4He ($20.3 \text{ cm}^3/\text{mole}$)

Since most previous ultrasonic measurements on hcp ^4He were performed at lower densities (Suzuki et al. (1979), Wanner et al. (1976)), several crystals were grown at a

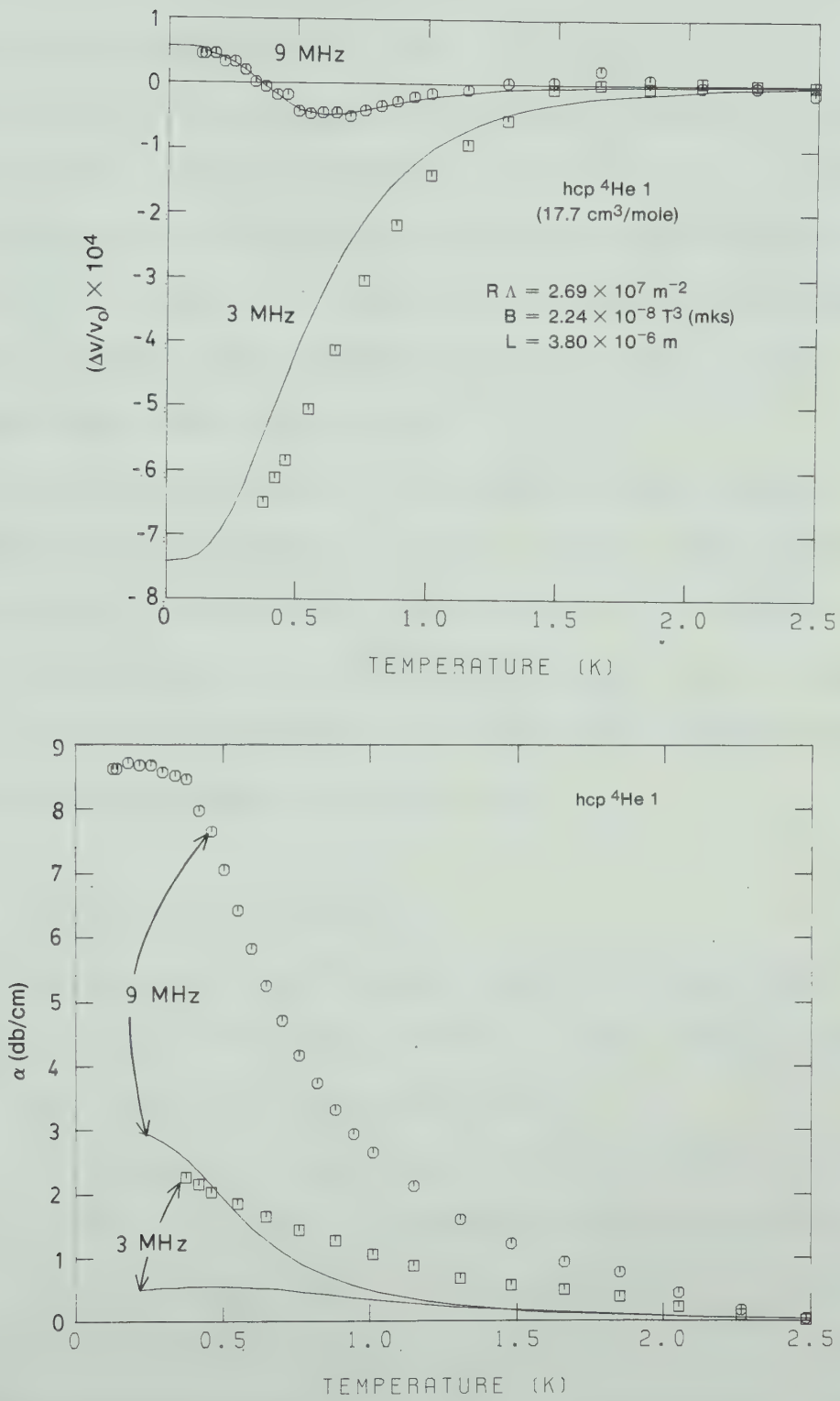


Figure 4.40 Dislocation fits (3 and 9 MHz) of v and α for hcp $^4\text{He 1}$.

density of $20.3 \text{ cm}^3/\text{mole}$.

In each of these crystals, the attenuation rose so steeply that measurements were impossible below 1 K. This indicated the presence of a large anomaly although the velocity remained adiabatic down to 1 K. All of the crystals grown at this density had the same velocity (see table 3 in section 4.5) perhaps indicating that they all grew at a particular orientation which had a large value of the orientation factor R .

By applying large 3 MHz pulses at 200 mK, the attenuation was reduced. During warming, the anomaly recovered to its original form around 0.9 K during which time the attenuation increased until the signal disappeared.

Since it was possible to take only limited data on these crystals, none are displayed.

4.4-3 Effects of Impurities

Crystals of hcp ^4He were grown from gas with ^3He concentrations of 10 ppm (denoted by *), 105 ppm (denoted by **) and 1400 ppm (denoted by ***).

In figure 4.41 the results are shown for *hcp ^4He 7 (10 ppm ^3He). Figure 4.42 shows the anomaly observed in **hcp ^4He 8 (105 ppm ^3He). No effects due to the impurities were observed in either crystal. In both cases, the velocity fits are quite good but, as in pure hcp ^4He , the predicted attenuation is a factor of 2-3 smaller than the measured attenuation. The relative sizes of the 3 and 9

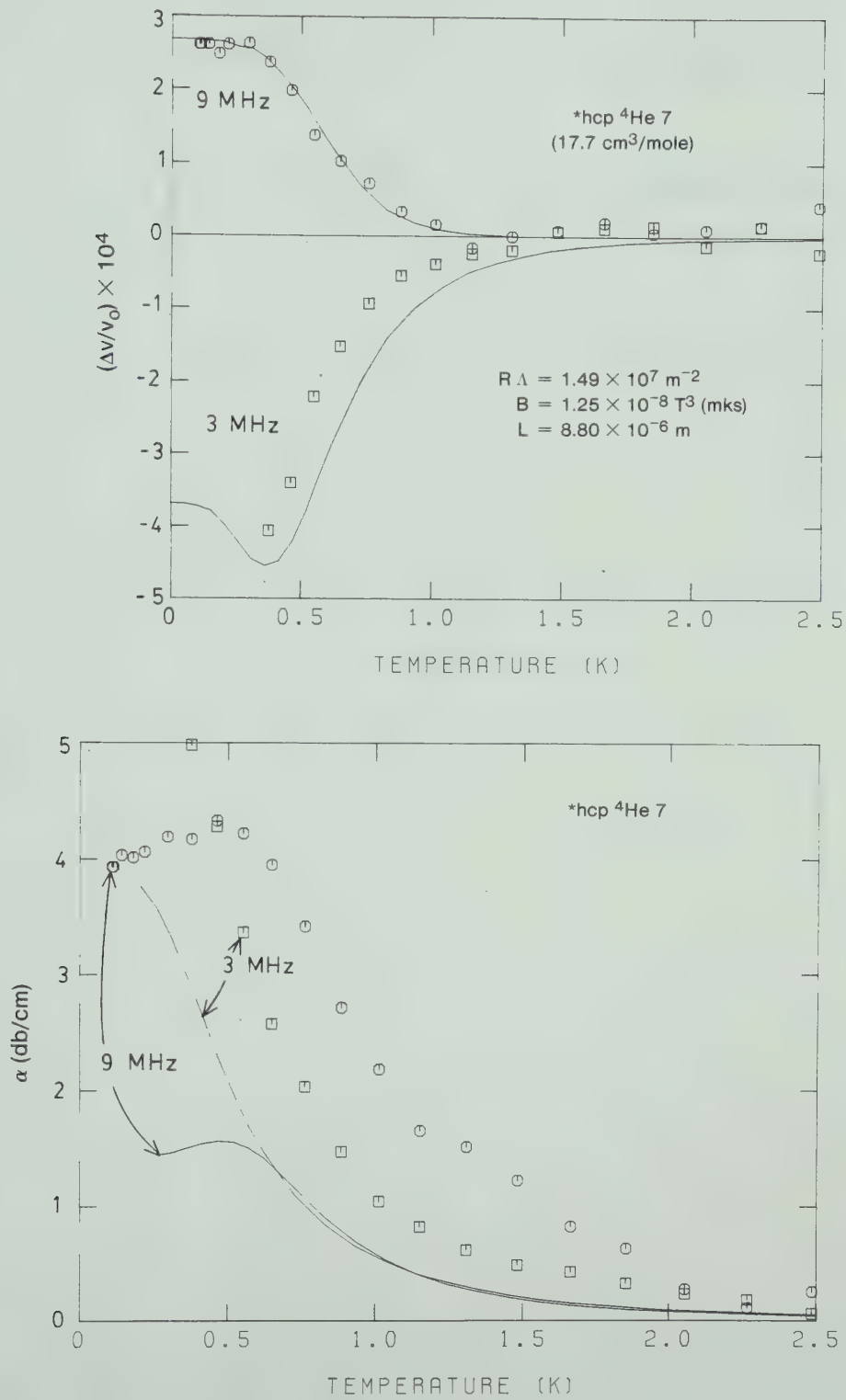


Figure 4.41 Dislocation fits (3 and 9 MHz) of v and α for *hcp ^3He 7 (10 ppm ^3He)

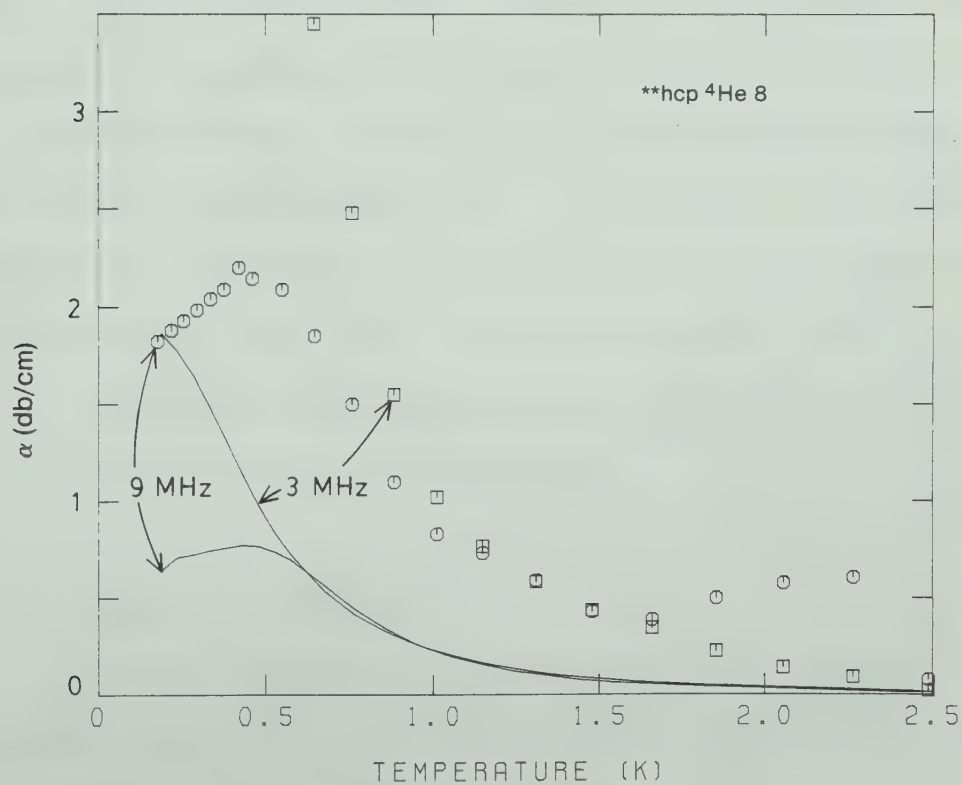
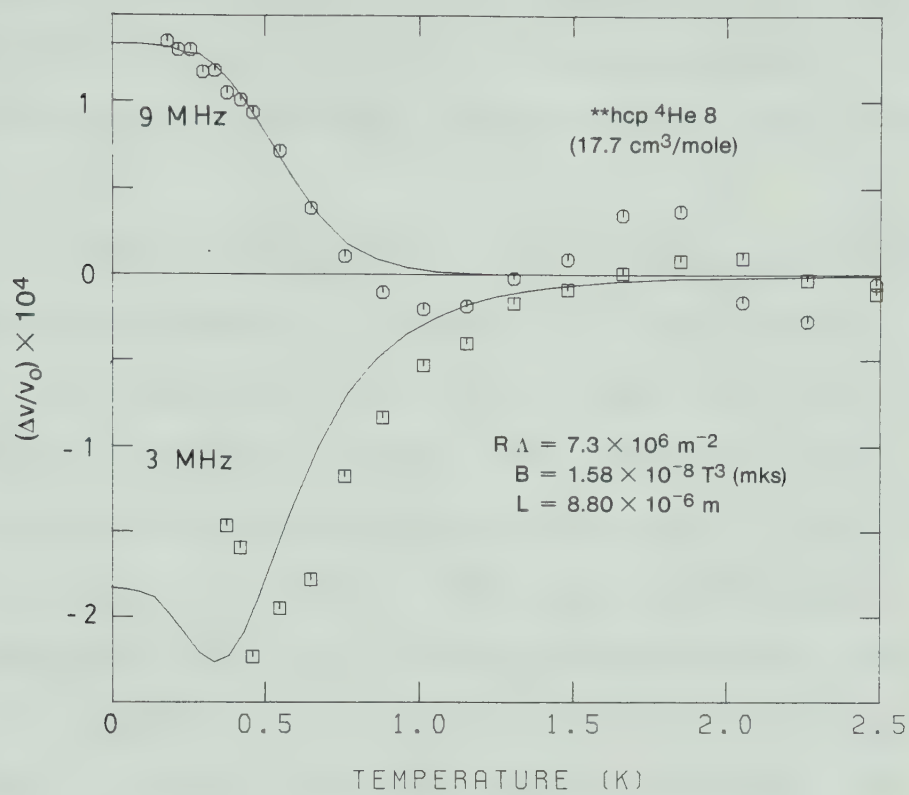


Figure 4.42 Dislocation fits (3 and 9 MHz) of v and α for ^{4}He 8 (105 ppm ^3He).

MHz attenuation as well as the maximum in the 9 MHz attenuation at about 0.5 K are correctly predicted using the dislocation parameters determined from the velocity data.

By adding 1400 ppm ^3He , the anomaly was almost completely eliminated. Figures 4.43 and 4.44 show v and α at 3 and 9 MHz in ***hcp ^3He 9. The 9 MHz data show no anomaly or hysteresis but at 3 MHz there is a small hysteresis in the attenuation below 1.5 K. This probably indicates that 1400 ppm of ^3He is not sufficient to completely pin the dislocations at this stress amplitude.

In addition to the impure crystals grown at 17.7 cm^3/mole , a crystal was grown at 20.3 cm^3/mole with 1400 ppm of ^3He . This crystal, ***hcp ^4He 10, had the same velocity (512 m/sec) as the pure crystal hcp ^4He 4 but, in contrast to that crystal, it had low attenuation over the entire temperature range. It behaved like the crystal in figures 4.43 and 4.44 with no anomaly and only a small hysteresis in the 3 MHz attenuation below 1 K.

The amplitude dependence of v and α was not studied in any of the impure ^4He crystals.

4.5 Adiabatic Region

In the temperature region above the anomaly, the velocity decreased with temperature with a temperature dependence of the adiabatic form

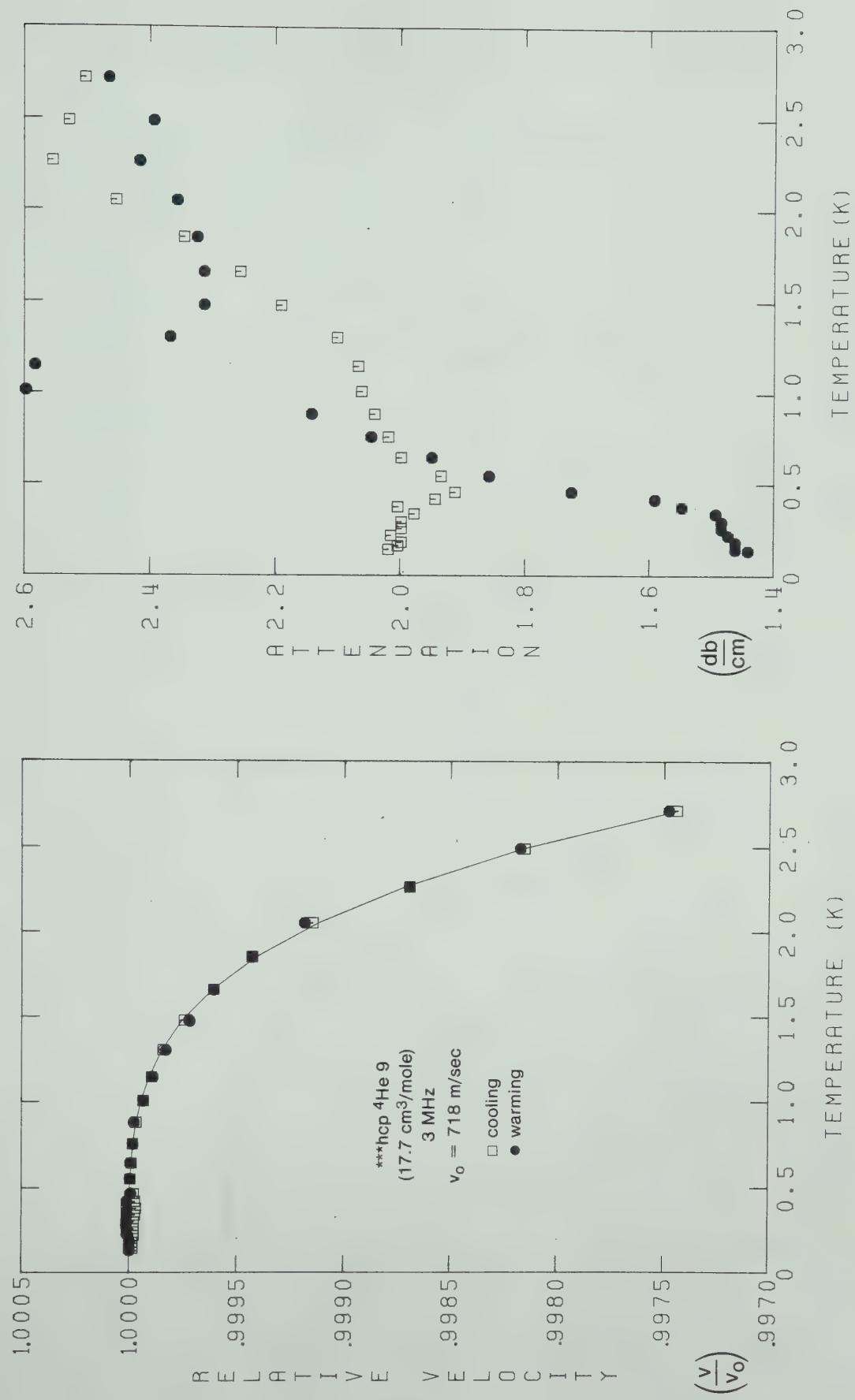


Figure 4.43 v and α in ***hcp ⁴He 9 (1400 ppm ³He) @ 3 MHz

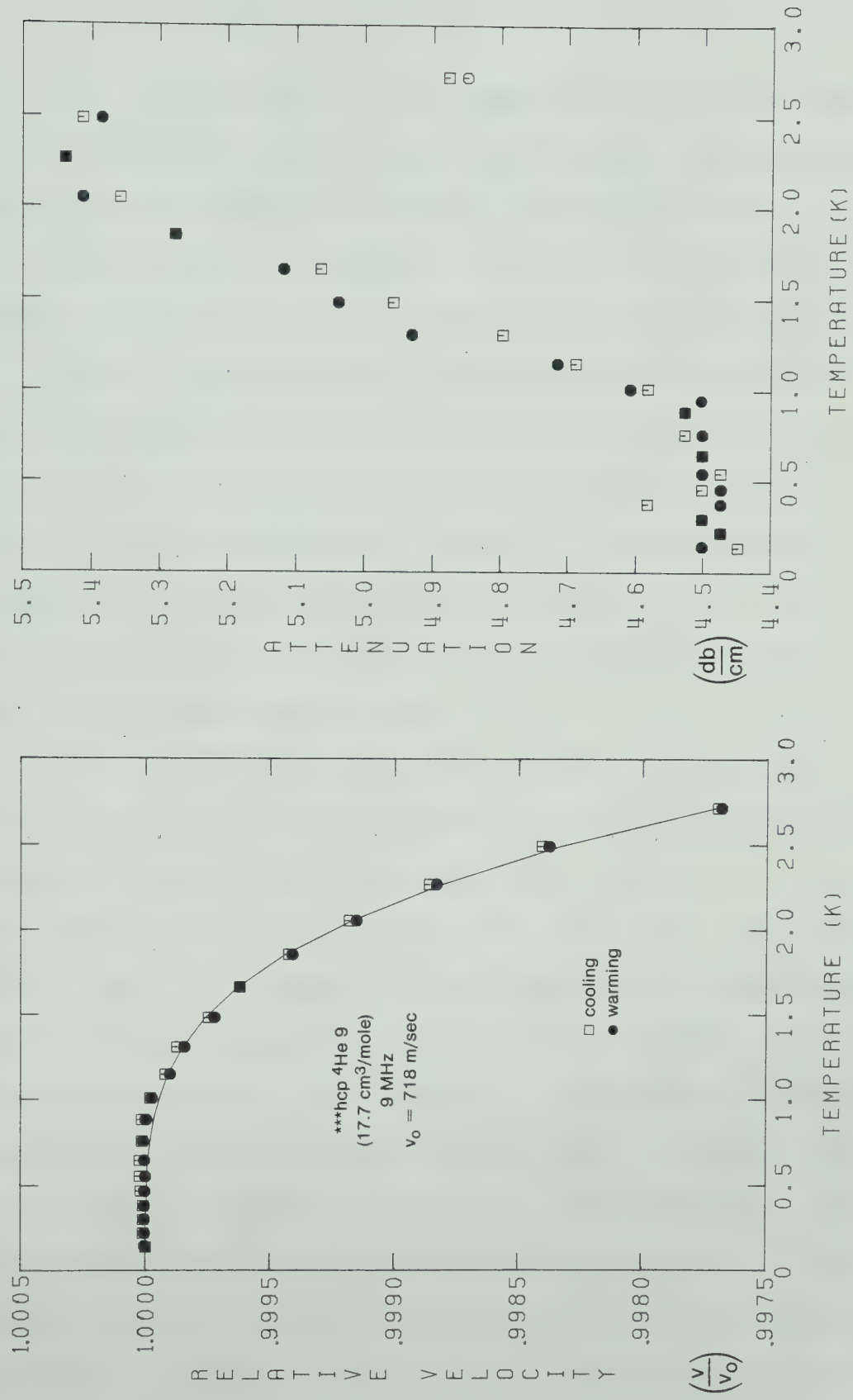


Figure 4.44 v and α in ***hcp ³He 9 (1400 ppm ³He) @ 9 MHz

$$v_a(T) - v_a(0) = aT^4 + bT^6. \quad (2.2-6)$$

The coefficients a and b obtained by a least squares fit to the sound velocity above the anomaly are tabulated, along with the adiabatic velocity extrapolated to $T = 0$, in tables 1, 2 and 3. Table 1 gives the coefficients for hcp ^3He , table 2 for bcc ^3He and table 3 for hcp ^4He .

Before discussing the values of the coefficients, some comments on the method of obtaining them are in order. The velocity data for a particular crystal were first plotted against temperature. Then, if an anomaly was present, the maximum temperature at which it was observed was estimated and only the data above that temperature were used in the least squares fit.

At 9 and 21 MHz, where the velocity anomaly was usually positive, this worked well in the sense that the parameters a and b did not depend very strongly on the exact temperature range of the fit. At 3 MHz, the parameters a and b did depend on the temperature range chosen. This can be understood by looking at figure 2.6. The negative anomaly at 3 MHz extends to considerably higher temperatures than the anomalies at 9 and 21 MHz and, due to its smooth temperature dependence, it cannot be easily distinguished from the adiabatic velocity change. Thus, it was difficult to choose an upper temperature limit for the anomaly and this resulted in an uncertainty in the coefficients a and b at 3 MHz. This uncertainty also

TABLE 1

ADIABATIC SOUND VELOCITY IN hcp ^3He

Crystal	Molar Volume (cm^3)	^4He (ppm)	$v_a(0)$ (m/sec)	$\Omega/2\pi$ (MHz)	$a \times 10^2$ (m/sec-K 4)	$b \times 10^2$ (m/sec-K 6)
hcp ^3He 2	18.6	1.35	830	3	-2.87	-0.108
				9	-4.82	0.054
hcp ^3He 3	18.6	1.35	831	3	-4.85	0.098
				9	-5.23	0.110
				21	-5.13	0.098
hcp ^3He 4	18.6	1.35	806	3	-4.31	0.146
				9	-4.63	-0.022
hcp ^3He 5	18.6	1.35	870	3	-2.29	-0.108
				9	-2.67	-0.047
				21	-3.23	0.003
*hcp ^3He 12	18.6	47	825	3	-3.83	-0.004
				9	-2.58	-0.136
**hcp ^3He 13	18.6	430	823	3	-4.54	0.068
				9	-4.43	0.053
***hcp ^3He 15	18.6	5300	825	3	-5.92	0.207
				9	-4.24	-0.012
***hcp ^3He 17	18.6	5300	821	3	-6.92	0.366
				21	-4.29	0.054
hcp ^3He 7	17.8	1.35	1009	3	-1.15	-0.046
				9	-2.78	0.085
hcp ^3He 9	17.8	1.35	914	3	-2.62	0.001
				9	-2.34	-0.023
				21	-2.00	-0.044

TABLE 2

ADIABATIC SOUND VELOCITY IN bcc ^3He

Crystal	Molar Volume (cm^3)	^4He (ppm)	$v_a(0)$ (m/sec)	$\Omega_i/2\pi$ (MHz)	$a \times 10^2$ (m/sec-K 4)	$b \times 10^2$ (m/sec-K 6)
bcc ^3He 46	24.2	1.35	488	3 9	-49.52 27.04	-82.3 -275.4
*bcc ^3He 53	24.2	47	498	3 9	-10.03 61.28	-218.0 -343.6
bcc ^3He 45	22.3	1.35	592	3 9	-16.35 -46.18	-9.31 5.92
bcc ^3He 33	20.1	1.35	722	3 9	-18.73 -7.82	0.63 -4.62
bcc ^3He 36	20.1	1.35	792	3 9 21	-19.16 -13.09 -16.67	0.773 -1.383 -0.666
bcc ^3He 43	20.1	1.35	745	3 9	-17.23 -16.81	1.625 0.812
*bcc ^3He 48	20.1	47	689	3	-17.93	1.766
*bcc ^3He 50	20.1	47	728	3 9	-18.37 -15.98	0.585 0.471
**bcc ^3He 54	20.1	430	761	3 9	-16.34 -26.87	-0.133 5.01
***bcc ^3He 56	20.1	5300	753	3 9 21	-17.92 -15.35 -16.24	0.355 -0.010 -0.120

TABLE 3

ADIABATIC SOUND VELOCITY IN hcp ^4He

Crystal	Molar Volume (cm^3)	^3He (ppm)	$v_a(0)$ (m/sec)	$\Omega/2\pi$ (MHz)	$a \times 10^2$ (m/sec-K 4)	$b \times 10^2$ (m/sec-K 6)
hcp ^4He 4	20.3	$\lesssim 1$	511	3	-22.93	1.52
***hcp ^4He 10	20.3	1400	512	3	-23.48	1.66
				9	-22.69	1.37
hcp ^4He 11	20.3	~ 200	512	3	-16.18	-0.16
hcp ^4He 12	20.3	< 200	522	3	-24.84	1.93
hcp ^4He 1	17.7	$\lesssim 1$	724	3	-2.02	-0.127
				9	-3.02	-0.021
hcp ^4He 3	17.7	$\lesssim 1$	724	3	-3.08	-0.022
				9	-3.79	0.058
				21	-3.55	0.015
*hcp ^4He 7	17.7	10	723	3	-3.52	0.019
				9	-3.61	0.103
**hcp ^4He 8	17.7	105	723	3	-3.76	0.054
				9	-5.04	0.203
***hcp ^4He 9	17.7	1400	723	3	-3.84	0.060
				9	-3.79	0.104

affected the 3 MHz anomaly. The general effect was to reduce the size of a negative anomaly from its true value by including part of the anomaly in the adiabatic temperature dependence.

From tables 1, 2 and 3 it appears that the coefficients a and b at 9 and 21 MHz do agree better than those at 3 and 9 MHz, supporting the above considerations.

Not enough crystals were studied at each density to make definite statements about the variations in a and b for different orientations. There does, however, appear to be some variation in a from crystal to crystal, especially in hcp ^3He . In most crystals, the coefficients b found at different frequencies are too inconsistent to draw any conclusions.

The coefficients a shown for hcp ^4He in table 3 do not show much variation between crystals but the velocities in all of the crystals at a particular density were the same. This probably means that the crystals grew at the same orientation and so the coefficients for the adiabatic velocity are expected to agree.

Two points should be noted about the density dependence of a and b . First, both a and b increase in magnitude as the density decreases. Secondly, especially in bcc ^3He where a larger range of densities was studied, the coefficient b becomes much larger with respect to a at lower densities. A similar large T^6 coefficient in the velocity has been observed in bcc ^3He before (Wanner et al.

(1973) and Iwasa and Suzuki (1981)) and was attributed by the latter authors to the influence of thermal vacancies as discussed in section 2.3 (cf. equation 2.3-1).

4.6 Thermally Activated Recovery

It was mentioned in earlier sections of this chapter that the recovery during warming of v and α to their original values was thermally activated. The first indication of this was the observation that, if the warming was stopped in the recovery region, v and α were time dependent and eventually reached their cooling values. The rate at which this recovery occurred increased rapidly with temperature. It proved possible to measure the recovery rate as a function of temperature in ^3He at several densities and thus to determine the activation energy of the recovery process.

In hcp ^4He , the recovery occurred around 1 to 1.5 K at $17.7 \text{ cm}^3/\text{mole}$ and around 0.9 K at $20.3 \text{ cm}^3/\text{mole}$. Although the recovery rate increased with temperature, the data were not good enough to measure the rates and so no activation energies could be determined.

The general method used to measure the recovery rates was as follows. The crystal was first cooled from some temperature near melting to its minimum temperature. Then, a large number of high amplitude 3 MHz pulses were applied, decreasing the anomaly as much as possible. The crystal was then warmed quickly to a temperature in the

recovery region and held there while v and α were measured as functions of time. When the recovery was either completed or proceeding very slowly, the crystal was warmed to near melting and the procedure repeated, stopping at a different temperature in the recovery region. By comparing the curves for v and α as functions of time at different temperatures, the relative recovery rates could be determined.

Figure 4.45A shows the recovery of α (at 3 MHz) in the crystal hcp ^3He 5 ($18.6 \text{ cm}^3/\text{mole}$) at temperatures between 1.39 and 1.75 K. At these temperatures the velocity anomaly was very small so no significant changes in v were observed during the recovery. Each attenuation curve started from the same low temperature value of α and eventually reached the cooling value. Since the cooling value of α decreased with temperature in this region (see figure 4.1), some correction was necessary in order that the changes in α directly reflected the stage in the recovery process. The α values shown in figure 4.45A have been scaled by a factor equal to the measured difference between the cooling value of α and its initial low temperature value. This ensured that the various curves in figure 4.45A had the same asymptotic value.

The similarity in the shapes of the various curves in figure 4.45A is apparent. By scaling the time dependence of each isotherm by a factor τ (with τ chosen to be 1 for $T = 1.57 \text{ K}$), the various isotherms could be made to

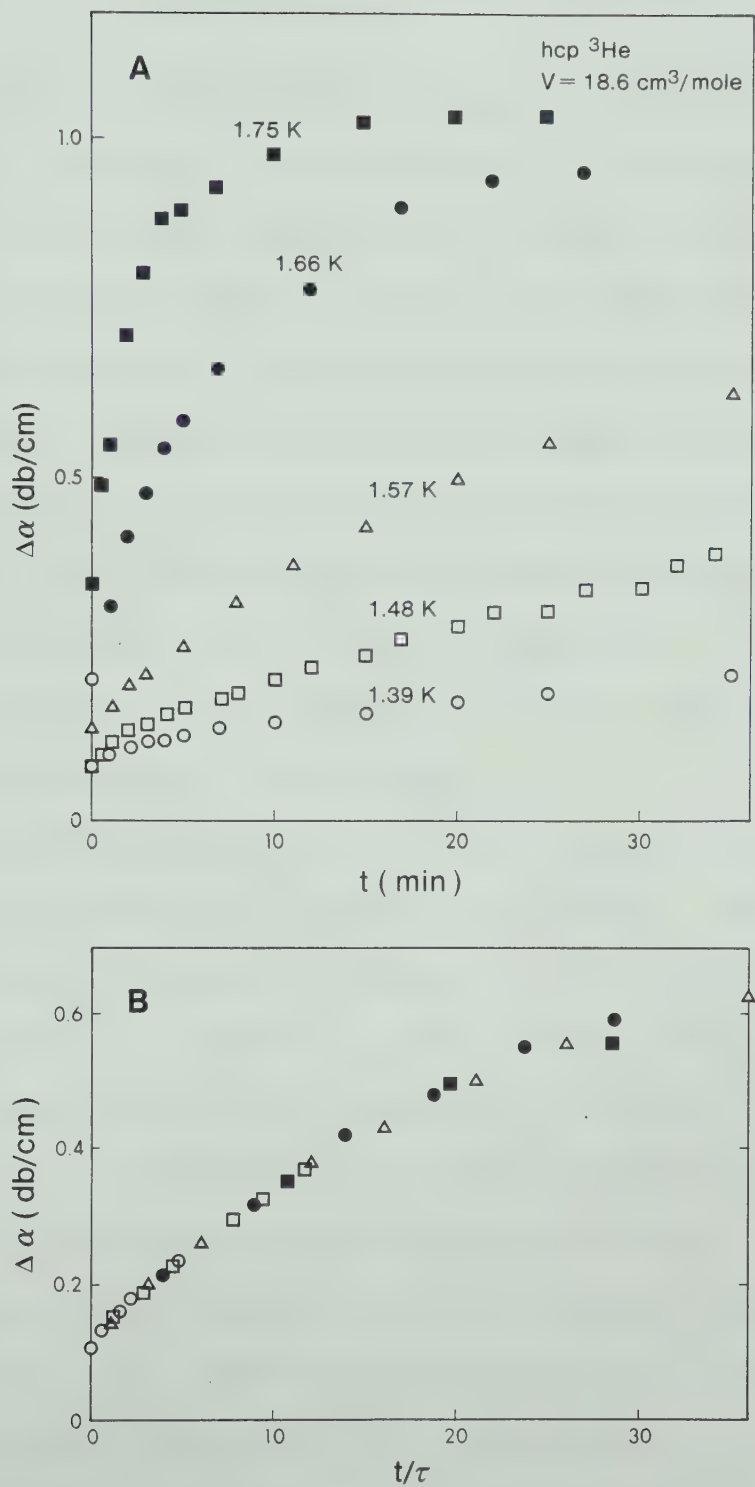


Figure 4.45 Time dependent recovery in hcp ^3He 5 (18.6 cm³/mole)

coincide as shown in figure 4.45B. The recovery rates at different temperatures (relative to $T = 1.57$ K) are then given by $1/\tau$. The values of τ thus obtained are listed in table 4.

Figure 4.46 shows the analogous results for bcc ^3He 43 ($20.1 \text{ cm}^3/\text{mole}$). In this case, it is easier to use the velocity since the attenuation overshoot its cooling value and it was therefore difficult to choose an appropriate scaling factor. The velocity required no scaling if the results were plotted as a deviation from the adiabatic velocity at the appropriate temperature.

Once again, the various isotherms coincided when scaled by an appropriate τ (with τ chosen as 1 for $T = 0.76$ K). The values of τ are listed in table 4 and the universal curve is shown in figure 4.46B.

Note that the velocity did not recover monotonically to its cooling value but rather went through a minimum. However, the curve shown in figure 4.46B is very similar to the one shown in figure 2.3 for the dislocation contribution to the velocity as a function of average loop length. The thermally activated recovery thus corresponded to an increase of the average loop length with time.

Figure 4.47 shows the recovery in bcc ^3He 45 ($22.3 \text{ cm}^3/\text{mole}$). In this case the interpretation is not as clear since the initial state did not correspond to a pinned anomaly (cf. figure 4.25). However, the recovery was still thermally activated as can be seen from the attenuation

TABLE 4
RECOVERY RATES IN ^3He

hcp ^3He 5 ($18.6 \text{ cm}^3/\text{mole}$)

T(K)	τ	$\ln (1/\tau)$
1.39	9.26	-2.23
1.48	3.08	-1.12
1.57	1.00	0
1.66	0.202	1.60
1.75	0.056	2.88

bcc ^3He 43 ($20.1 \text{ cm}^3/\text{mole}$)

T(K)	τ	$\ln (1/\tau)$
0.698	2.65	-0.973
0.730	2.38	-0.868
0.758	1.00	0
0.787	0.370	0.993
0.818	0.252	1.139
0.881	0.076	2.574

bcc ^3He 45 ($22.3 \text{ cm}^3/\text{mole}$)

T(K)	τ	$\ln (1/\tau)$
0.417	7.58	-2.018
0.461	2.70	-0.993
0.504	1.00	0
0.547	0.323	1.13
0.595	0.100	2.303

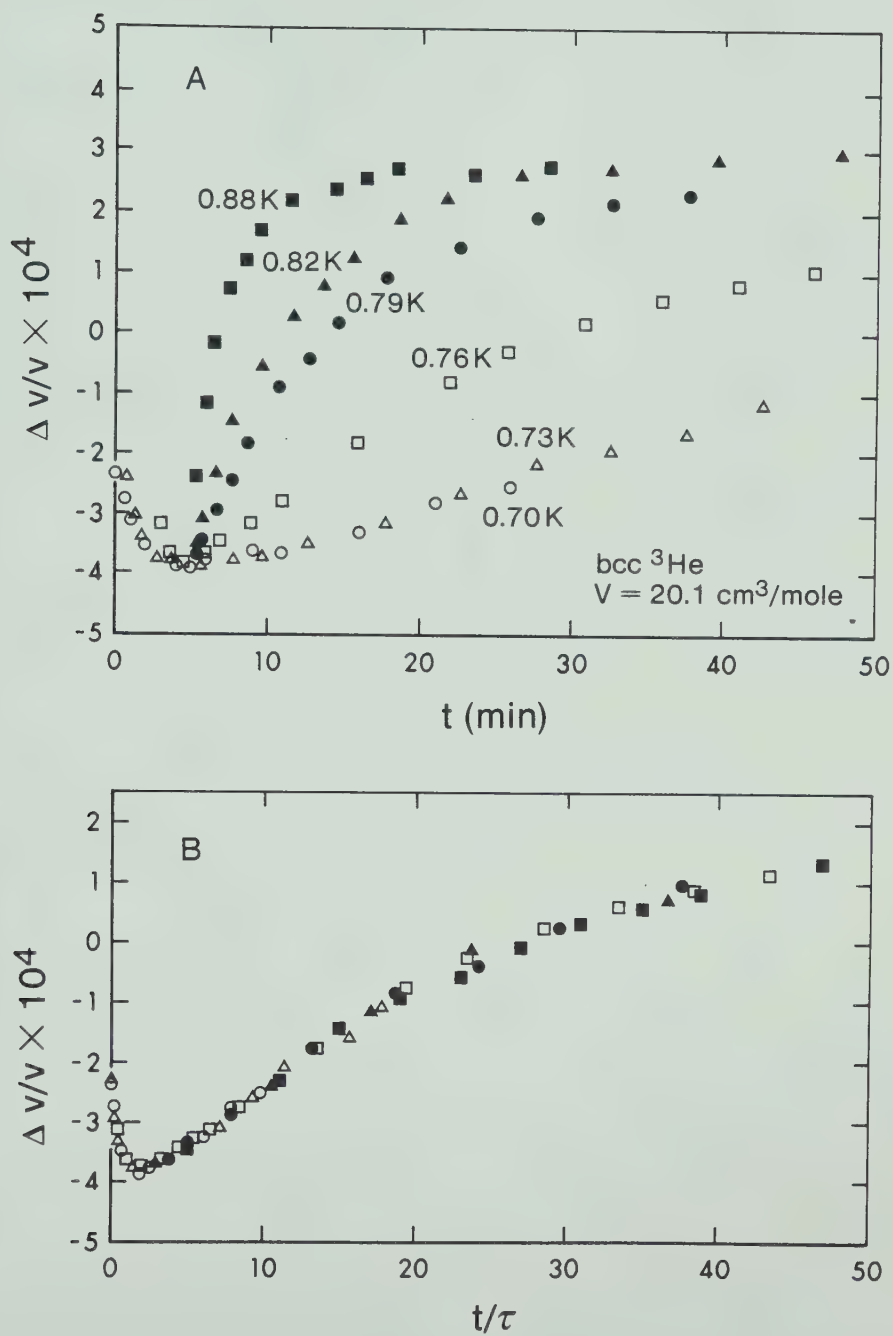
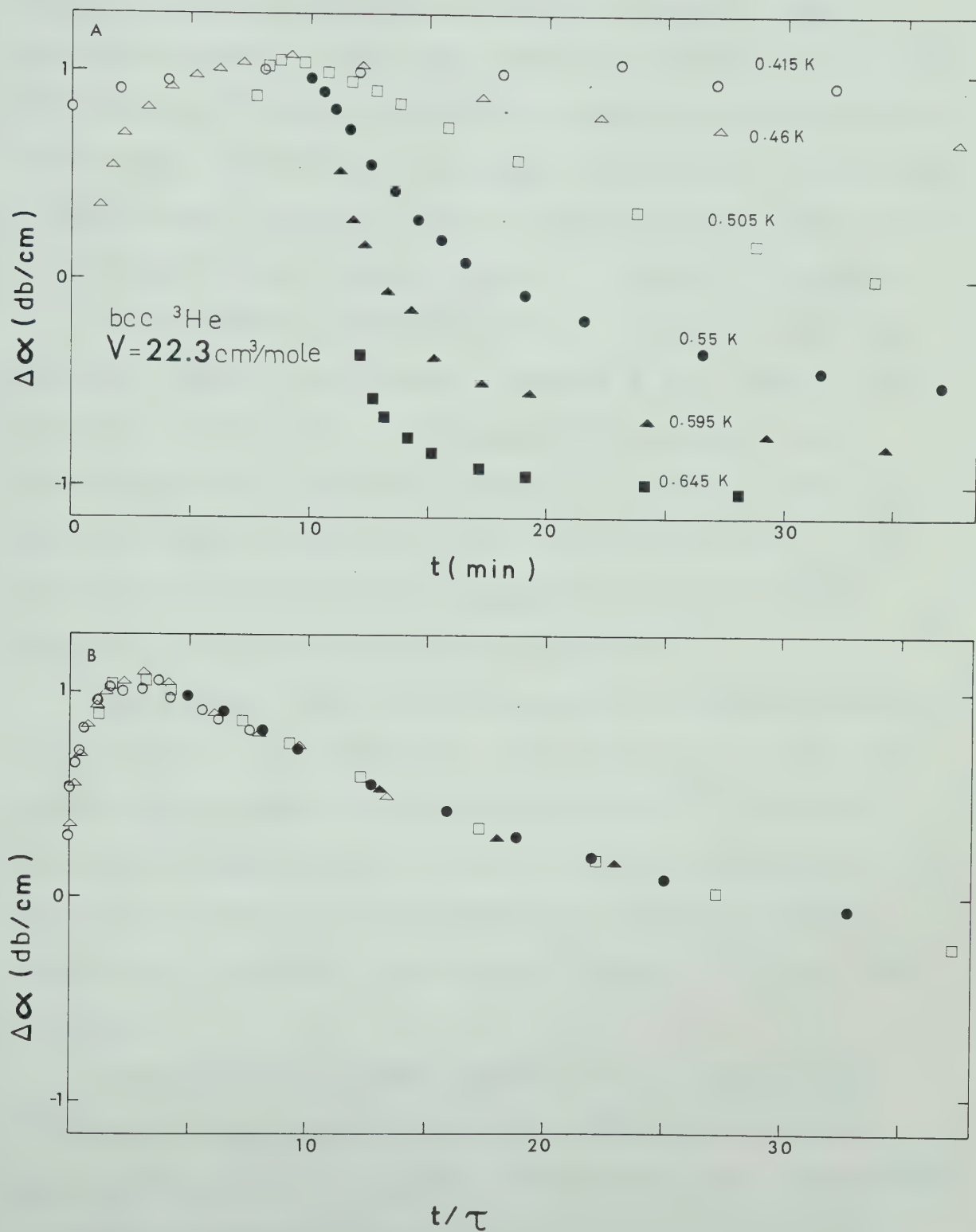


Figure 4.46 Time dependent recovery in bcc ^3He 43 ($20.1 \text{ cm}^3/\text{mole}$)

Figure 4.47 Time dependent recovery in bcc ^3He 45 ($22.3 \text{ cm}^3/\text{mole}$)

recovery curves in figure 4.47. The velocity changes could only be followed in a narrow temperature range so the attenuation was chosen for the determination of the activation energy. The final (cooling) values of α depended only weakly on temperature and the attenuation went through a peak whose temperature dependence was unknown. Therefore, no scaling was applied to the α values which may have led to systematic errors in the rates $1/\tau$ (listed in table 4).

The recovery rates determined in this way for the three ^3He crystals are shown in figure 4.48. Here $\ln(1/\tau)$ is plotted against $1/T$. The resulting straight lines indicate that the recovery process is thermally activated. From the slopes (determined by a least squares fit), the activation energies can be determined for the different crystals. The values are listed in table 5.

An attempt was made to measure an activation energy in bcc ^3He 46 ($24.2 \text{ cm}^3/\text{mole}$). The recovery rate did not decrease with temperature as quickly as $e^{-W/T}$ and so no activation energy could be found. This non-thermally activated recovery at low temperatures may reflect the non-thermal (tunneling) mobility of defects in ^3He at low pressures.

A similar effect was noticed in bcc ^3He 45 ($22.3 \text{ cm}^3/\text{mole}$) at low temperatures. As a result, the rates determined at the three higher temperatures were considered to be more reliable and were used to find the activation energy. This accounts for the relatively large uncertainty

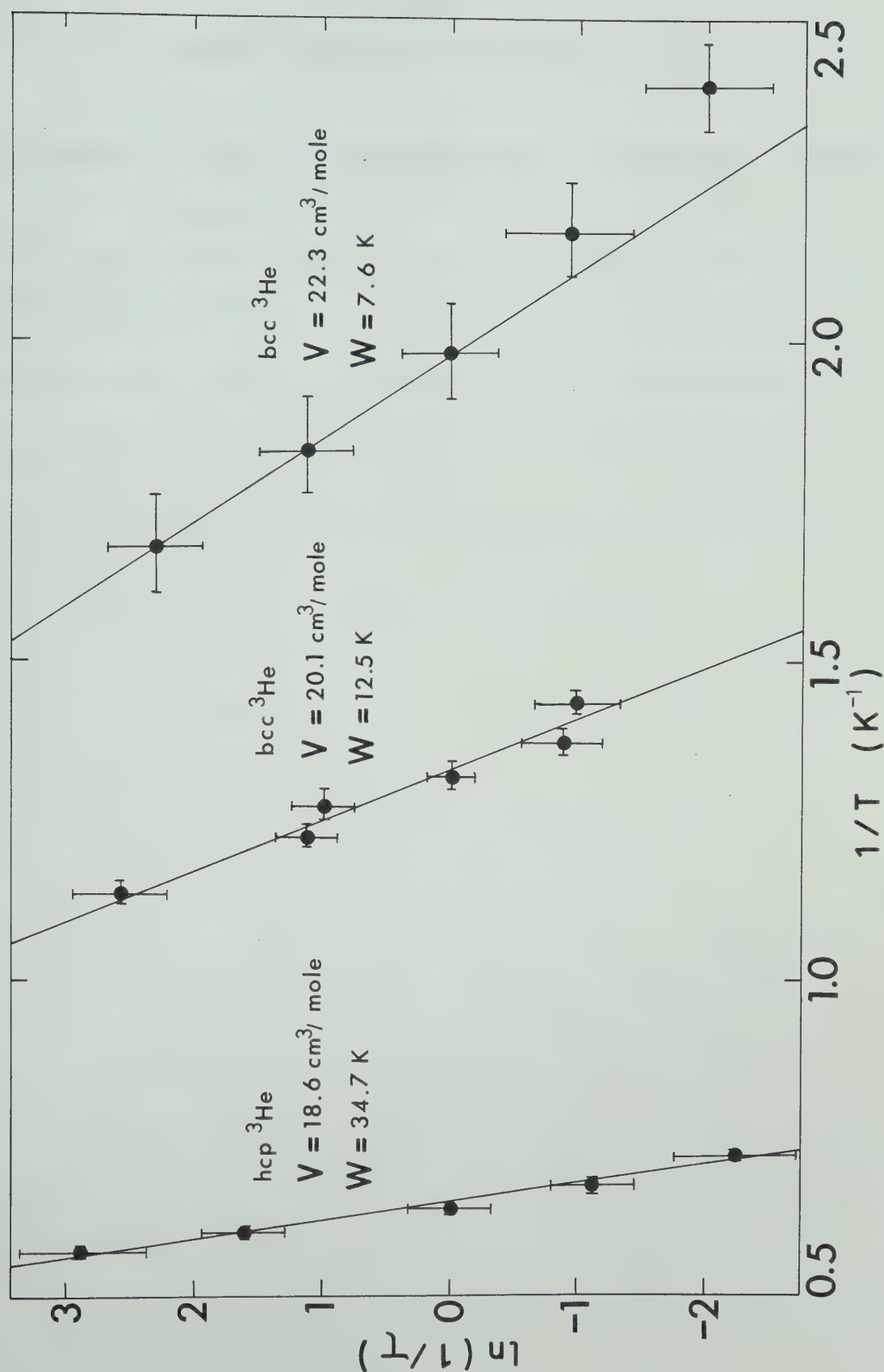
Figure 4.48 Thermal activation of the recovery process in ^3He .

TABLE 5
THERMAL ACTIVATION ENERGIES IN ^3He

Crystal	Molar Volume (cm^3)	Crystallographic Phase	Activation Energy W (K)
hcp ^3He 5	18.6	hcp	34.7 ± 5
bcc ^3He 43	20.1	bcc	12.5 ± 2
bcc ^3He 45	22.3	bcc	$7.6 \begin{smallmatrix} + 1 \\ - 2 \end{smallmatrix}$

quoted for W at $22.3 \text{ cm}^3/\text{mole}$.

4.7 Dislocation Parameters

All the dislocation parameters found by fitting to the anomalies in different crystals are collected in tables 6, 7 and 8.

In hcp ^3He , the values of the average loop length L vary by about an order of magnitude while the dislocation densities RA vary by nearly two orders of magnitude. Since the dislocation densities depend on the random dislocation network and contain the orientation factor R , they are expected to differ considerably from crystal to crystal. The damping B , which should be characteristic of the crystal lattice itself, varies only by a factor of four between crystals and some of this may be due to uncertainties in the fitting procedure.

The values of L , RA and B found in bcc ^3He show considerably less variation. At least part of this is due to the fact that the orientation factor R is much less anisotropic in cubic lattices than in hexagonal ones. No significant reduction in the average loop length L is observed in crystals containing 47 or 430 ppm of ^4He .

The values of L and RA in hcp ^4He vary much less than in hcp ^3He . This may be due to the fact, mentioned previously, that the hcp ^4He crystals all appeared to grow at the same orientation (as indicated by the sound velocity).

TABLE 6
DISLOCATION PARAMETERS FOR hcp ^3He

Crystal	Molar Volume (cm^3)	^4He (ppm)	$t=L/\ell_c$ @ 3MHz	L (m)	$R\lambda$ (m^{-2})	$\frac{g}{(B=gT)^3}$ (mks)
hcp ^3He 2	18.6	1.35	0.14	5.94×10^{-6}	4.28×10^7	1.00×10^{-8}
hcp ^3He 3	18.6	1.35	0.24	1.02×10^{-5}	1.70×10^6	1.00×10^{-8}
hcp ^3He 5	18.6	1.35	1.5	6.37×10^{-5}	1.84×10^7	1.41×10^{-8}
*hcp ^3He 12	18.6	47	0.14	5.94×10^{-6}	1.18×10^8	2.25×10^{-8}
**hcp ^3He 13	18.6	430	0.17	7.21×10^{-6}	2.17×10^7	5.67×10^{-9}
hcp ^3He 7	17.8	1.35	0.13	7.30×10^{-6}	4.32×10^7	5.73×10^{-9}

TABLE 7
DISLOCATION PARAMETERS FOR bcc ^3He

Crystal	Molar Volume (cm^3)	^4He (ppm)	$t=L/\ell_c$ @ 3MHz	L (m)	$R\lambda$ (m^{-2})	g ($B=gT^3$) (mks)
bcc ^3He 36	20.1	1.35	0.27	9.66×10^{-6}	2.62×10^7	2.76×10^{-8}
bcc ^3He 43	20.1	1.35	0.26	9.38×10^{-6}	1.96×10^7	2.70×10^{-8}
*bcc ^3He 50	20.1	47	0.20	7.18×10^{-6}	5.86×10^7	2.21×10^{-8}
**bcc ^3He 54	20.1	430	0.36	1.30×10^{-5}	3.12×10^7	2.23×10^{-8}

TABLE 8

DISLOCATION PARAMETERS FOR hcp ^4He

Crystal	Molar Volume (cm^3)	^3He (ppm)	$t=L/\ell_c$ @ 3MHz	L (m)	$R\Lambda$ (m^{-2})	g ($B=gT^3$) (mks)
hcp ^4He 1	17.7	$\lesssim 1$	0.13	3.80×10^{-6}	2.69×10^7	2.24×10^{-8}
*hcp ^4He 7	17.7	10	0.30	8.80×10^{-6}	1.49×10^7	1.25×10^{-8}
**hcp ^4He 8	17.7	105	0.30	8.80×10^{-6}	7.30×10^6	1.58×10^{-8}

4.8 Zero Sound

From the discussion in section 2.2, sound is expected to propagate as "zero sound" at sufficiently low temperatures. The expected zero sound velocity and attenuation dependences on temperature should be observable in solid helium.

From the results discussed in this thesis and the work of others (e.g. Calder (1977) or Iwasa et al. (1979)) it appears that at low temperatures, the dominant contribution to both v and α comes from interactions between sound waves and dislocations. If this contribution can be suppressed, the zero sound predictions may be tested.

The only crystals studied in which there was no noticeable dislocation contribution to v or α (as indicated by the absence both of a visible anomaly and of hysteresis after applying large 3 MHz pulses) were those of hcp ^3He with 0.53% ^4He . The bcc ^3He crystals with 0.53% ^4He still had a small 3 MHz anomaly and the hcp ^4He crystals with 1400 ppm of ^3He showed hysteresis in α .

Figure 4.49 shows the attenuation in ***hcp ^3He 17 at 3 and 21 MHz. The attenuation values are shifted to be approximately zero at low temperatures. Also shown are curves of the zero sound form (see equation 2.2-11)

$$\alpha = 5.5 \times 10^{-9} \omega T^4 \text{ db/cm} \quad (4.8-1)$$

where the factor 5.5×10^{-9} is determined by fitting to the

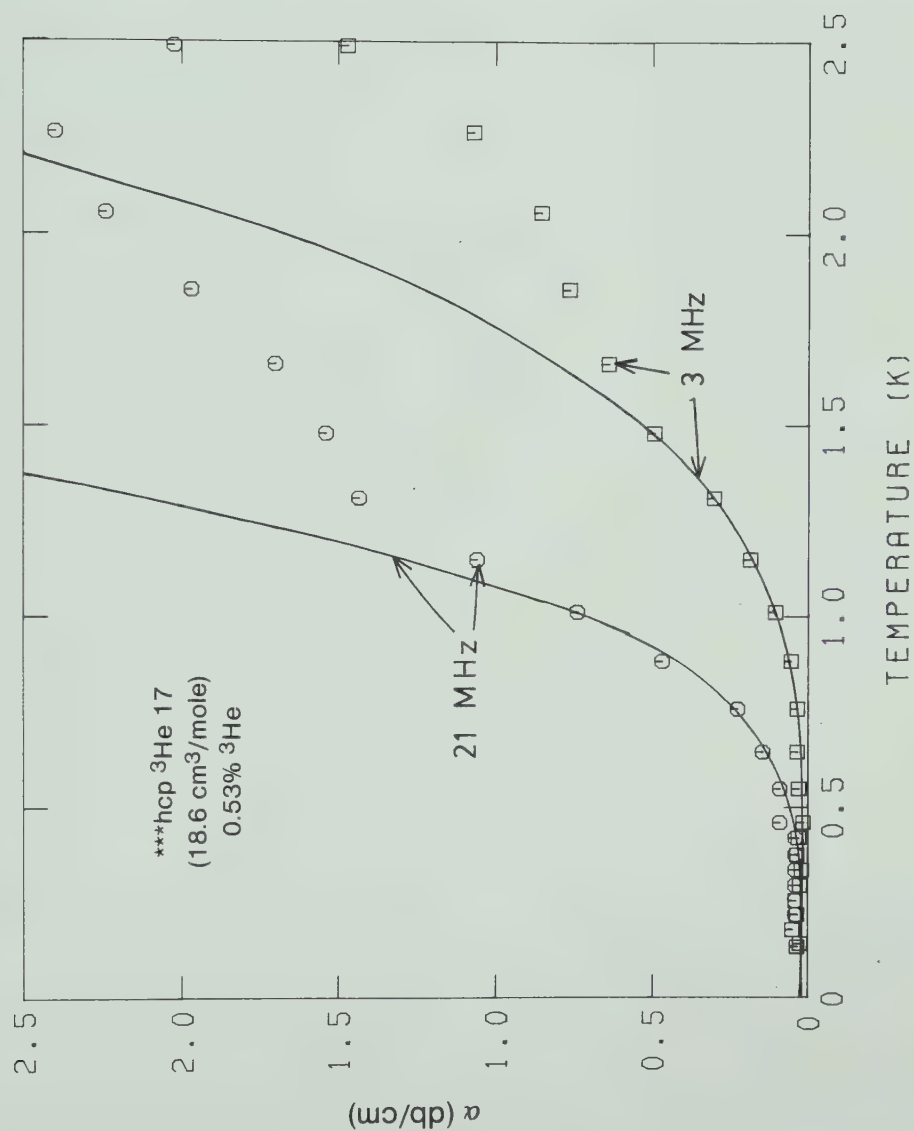


Figure 4.49 Zero sound attenuation in ***hcp ^3He 17 (0.53% ^4He).

21 MHz data. Below 1 K the agreement is excellent.

In the other crystals where the dislocation contribution was nearly suppressed, the attenuation increased with temperature at low temperatures and was larger at higher frequencies but no detailed analysis was made.

CHAPTER 5

DISCUSSION AND CONCLUSIONS

5.1 Discussion

In this chapter, the results described in Chapter 4 are compared to previous experimental work on solid helium and arguments are given for attributing the sound anomaly to dislocations. The comparison between the data and the theory of Granato and Lüke (1956) is discussed in some detail.

The previous measurements of the temperature dependence of the sound velocity in solid ^3He (Wanner et al (1973), Iwasa and Suzuki (1981), Iwasa et al (1981)) were made at low densities ($V > 24 \text{ cm}^3/\text{mole}$) in impure crystals (^4He concentration ≥ 200 ppm). The present work therefore contains the first measurements of the temperature dependence of the sound velocity and attenuation in hcp ^3He and in bcc ^3He at high densities. As a consequence, it also contains the first observations of an anomalous velocity and attenuation in ^3He since the anomaly was only present in high density crystals.

All previous measurements in ^3He (and most of those in ^4He) used sound frequencies greater than 10 MHz. The use of a 3 MHz transducer in this work resulted in a reduction of the anomalies when high amplitude 3 MHz pulses were applied at low temperature. This effect had not

previously been observed in either ^3He or ^4He . It allowed the anomaly to be changed and its recovery at high temperatures to be studied. The thermally activated recovery of the ultrasonic signal allowed the first acoustic measurements of activation energies to be made.

The use, for the first time, of high purity ^3He (1.35 ppm ^4He) allowed the effects of impurities to be examined. Although the absence in previous measurements of an anomaly in ^3He seems to be due to the low densities used, rather than to the ^4He present, it was important to check this. The addition of 0.53% of ^4He to the ^3He suppressed the anomaly and permitted both the amplitude dependence of the attenuation and its zero sound behaviour at low amplitudes to be observed for the first time in ^3He .

The results from the low density bcc ^3He crystals ($24.2 \text{ cm}^3/\text{mole}$) can be directly compared to previous work. The adiabatic coefficients listed in table 2 are approximately the same as those quoted by Wanner et al (1973) at $24.1 \text{ cm}^3/\text{mole}$. Iwasa and Suzuki (1981) observed a similar temperature dependence at $23.8 \text{ cm}^3/\text{mole}$ although they analysed it in terms of a term proportional to T^4 and one due to the vacancies. Neither of the above experiments observed an anomaly, in agreement with the observations during cooling of bcc ^3He 46 (cf. figures 4.27 and 4.28).

Iwasa et al (1981) investigated the effects of ^4He impurities in bcc ^3He ($24.4 \text{ cm}^3/\text{mole}$). No anomaly or amplitude dependence was seen but the frequency (10 MHz)

was high enough that the effects described in section 4.3-3 due to high amplitude 3 MHz pulses would not be expected. They observed an attenuation change at the isotopic phase separation. The phase separation occurred at 86 mK for 480 ppm of ^4He and at 98 mK for 1600 ppm of ^4He . These values are somewhat lower than the temperatures of 99 and 117 mK which they calculate from the regular solution theory (Edwards et al (1962)). The phase separation temperature discussed in section 4.3-4 for ^3He containing 0.53% ^4He was 125 mK, also somewhat lower than the calculated regular solution phase separation temperature of 144 mK. Greenberg and Armstrong (1980) observed the phase separation in their thermal conductivity measurements. At 500 ppm of ^4He , it occurred around 94 mK, somewhat higher than the acoustic measurements would indicate.

In view of the almost complete similarity between hcp ^3He and ^4He and of the large number of ultrasonic experiments which have been performed on ^4He , some discussion of other ^4He results is in order.

Previous work in this laboratory (Calder and Franck (1977) and Calder (1977)) on hcp ^4He at $17.4 \text{ cm}^3/\text{mole}$ (5, 15 and 25 MHz) showed anomalies very similar to those described in this thesis. The magnitude of the anomaly ranged from $\Delta v/v_0 < 10^{-4}$ to $\Delta v/v_0 \sim 3 \times 10^{-3}$, roughly the same range as observed in hcp ^3He at $17.8 \text{ cm}^3/\text{mole}$ (cf. section 4.2-3). Although the anomalies these authors described were not attributed to dislocations, the results

were in qualitative agreement with dislocation theory as described in this thesis. The amplitude dependences of v and α were not studied and no hysteresis was observed. This may have been due to the higher frequencies used (> 5 MHz) or to lower pulse amplitudes.

Several other ultrasonic measurements on hcp ^4He have shown an anomaly which has been interpreted in terms of dislocations. The measurements of Wanner et al (1976) were made at a single frequency (8 or 12 MHz) and showed either a positive or a negative anomaly which ranged in magnitude from $\Delta v/v_0 \sim 3 \times 10^{-4}$ to $\Delta v/v_0 \sim 3 \times 10^{-3}$.

The experiments and analysis most closely related to this thesis are those of Iwasa et al (1979). In hcp ^4He at $20.32 \text{ cm}^3/\text{mole}$, they observed positive velocity anomalies at 10 MHz as large as $\Delta v/v_0 \sim 3 \times 10^{-3}$. This is several times larger than those typically observed at 9 MHz in this work but the anomalies observed by Iwasa et al decreased when the crystal was warmed above 1 K. The anomalies they observed in a "well annealed" crystal were smaller ($\Delta v/v_0 \sim 3 \times 10^{-4}$). They analysed the frequency dependences of v and α in terms of an exponential distribution of dislocation loop lengths and found that the anomaly agreed qualitatively with the theory. They also found quantitative discrepancies similar to those shown in Chapter 4 of this thesis.

The agreement shown in Chapter 4 between the data and the Granato-Lücke theory of dislocation resonance is

evidence both for the existence of dislocations in helium and for the applicability of the vibrating string model but other possible causes of the anomaly should be discussed.

There are several reasons to believe that the anomaly is not a property of the perfect lattice. The anomaly varied both in magnitude and in shape in different crystals at the same density. Although some of the variation in magnitude could be due to an orientation effect, the anomaly differed between the hcp ^4He crystals whose sound velocities indicated that they had the same orientation. The fact that the anomaly could be reduced or eliminated either by applying high amplitude sound pulses or by adding isotopic impurities also argues against the anomaly being a bulk property of the crystal. Finally, the hysteresis seen after applying large pulses indicates that either the warming or the cooling state (or both) are metastable. The anomaly thus seems to be connected to some defect property which can vary from crystal to crystal.

There are several types of defects possible in helium. Of the point defects, only isotopic impurities and vacancies are likely to be important since other impurities freeze out at much higher temperatures.

It is difficult to attribute the anomaly to the isotopic impurities. The fact that the anomaly is present in helium with about 1 ppm of isotopic impurities and is essentially unchanged when 400 ppm are added indicates

that the anomaly is not sensitive to the impurity concentration. In addition, adding more impurities (≥ 1000 ppm) decreases rather than increases the anomaly.

Vacancies also are unable to explain the anomaly. The number of thermal vacancies decreases rapidly with temperature while the anomaly remains large. Also, as the density increases the number of vacancies decreases but the anomaly gets larger.

The other defects known to be important in solids are dislocations. There is considerable evidence for their existence in helium besides the sound measurements already described.

Low angle grain boundaries which are expected to consist of arrays of dislocations can be inferred from the mosaic spread observed in neutron diffraction experiments (Minkiewicz (1973)) and more directly from X-ray measurements (Fraas et al (1977)).

NMR measurements of spin lattice relaxation rates in bcc ^3He (Gifford et al (1970)) indicate the presence of small domains $\sim 50\mu$ in size, presumably consisting of low angle grain boundaries or stacking faults.

Charge mobilities were measured in plastically deformed ^4He by Gudenko and Tsymbalenko (1979) and by Guenin and Dahm (1981). Both groups could explain their results by assuming that ions were trapped by the dislocations produced during the deformation.

A variety of plastic flow measurements have been

made on solid helium. The results of Suzuki (1977) and of Sakai et al (1979) indicated that helium behaves much like a conventional solid where plastic flow involves the creation and movement of dislocations. Sanders et al (1977) and (1978) were able to melt a thin layer of helium around their crystals and thus to produce unconstrained crystals of hcp and bcc ^4He . They observed a very low yield stress of less than $5 \times 10^3 \text{ Nt/m}^2$ in these crystals which they interpreted as indicating a low Peierls stress. In hcp ^4He they found that small amounts of deformation led to very large increases in attenuation, in agreement with the expected increase in dislocation density. In bcc ^4He , however, deformation did not affect the attenuation, leading them to speculate that the plastic flow involved vacancies rather than dislocation multiplication.

Thermal conductivity measurements by Greenberg and Armstrong (1979) showed an anomalous contribution which could be explained by the scattering of thermal phonons by dislocations.

Although direct observation of dislocations has not been possible in helium, there is considerable evidence that they do exist and that they behave much like dislocations in conventional solids. The problem then is to determine the effects of the dislocations on sound propagation.

The best established theory of dislocation - sound wave interactions is that of Granato and Lücke. This

theory starts with a model of a dislocation as a damped vibrating string whose equation of motion is given by

$$A \frac{\partial^2 \xi}{\partial t^2} + B \frac{\partial \xi}{\partial t} - C \frac{\partial^2 \xi}{\partial x^2} = a\sigma. \quad (2.3-3)$$

Several assumptions are implicit in this model. The Peierls stress is neglected, an assumption often justified by the existence of large numbers of thermally activated kinks. At low temperatures, this may no longer be valid.

As usually developed, the theory assumes an elastically isotropic crystal. For several cases, such quantities as the elastic strain energies, which determine the dislocation effective mass A and string tension C , can be exactly calculated (Amelinckx (1979)). For basal dislocations in hexagonal crystals, the results are very close to the isotropic values but the effects of anisotropy for more general dislocation orientations are unknown.

Even if the concepts of an effective mass and a string tension for dislocations are valid, the expressions used for A and C are suspect. In this work and in all the work on helium, the values are those given in the original paper by Granato and Lücke (1956), namely

$$A = \pi \rho a^2 \quad ; \quad C = \frac{2Ga^2}{\pi(1-\nu)}. \quad (5.1-1)$$

These expressions include only the elastic energy of the dislocation strain field and ignore the core structure of

the dislocations, the effects of anisotropy, and the differences between screw and edge dislocations. It is probably more reasonable to assume (Balluffi and Granato (1979))

$$A = \alpha \rho a^2 \quad ; \quad B = \beta G a^2 \quad (5.1-2)$$

where α and β are numerical factors of order 0.5.

Although the damping coefficient B is treated as a parameter to be determined from experiment, the form assumed for B ($= gT^n$ where $n = 3$ in the analysis of Chapter 4) may not be correct. The damping due to thermal phonons certainly increases with temperature and the dominant contribution at low temperatures is expected to have the form $B \propto T^3$ (Ninomiya (1974)) but other damping mechanisms are possible. For example, a vibrating dislocation must lose some of its energy by radiating. Although the radiation force is not proportional to the dislocation velocity, its effects can be included by adding a frequency dependent term B_R to B (Garber and Granato (1970)) where

$$B_R = \frac{1}{8} \rho a^2 \omega. \quad (5.1-3)$$

For solid helium at 3 MHz, $B_R \approx 5 \times 10^{-11}$ mks which is negligible compared to the observed damping above 200 mK. At lower temperatures or higher frequencies, radiation damping may be significant.

Another important assumption made in the dislocation analysis of the anomalies in Chapter 4 was that the dislocation loop length distribution was exponential:

$$N(\ell) = \frac{\Lambda}{L^2} \exp \left(\frac{-\ell}{L} \right) . \quad (2.3-9)$$

This distribution is plausible for the case of pinning by point defects (Koehler (1952)) but is difficult to justify for network pinning.

The effects of choosing a Gaussian loop length distribution were investigated by Iwasa et al (1979). They found that the frequency dependence of the anomaly could be fit better (using one additional adjustable parameter). They also found that selecting different distributions changed the values of Λ and L by factors of 5 or more. The values of Λ and L found in Chapter 4 thus are not the true dislocation densities and lengths but rather are appropriate only to an exponential length distribution.

Despite the uncertainties in the applicability of the Granato-Lücke theory to helium and the uncertainties in the choices made for A, B, C and the length distribution $N(\ell)$, many of the predictions of the theory are relatively insensitive to the details of the dislocation properties. The degree to which the measurements presented in Chapter 4 agree with the Granato-Lücke theory will now be discussed.

One of the most stringent tests of the dislocation explanation of the anomaly is its frequency dependence.

The Granato-Lücke theory predicts that any negative velocity anomaly must eventually become positive at sufficiently high frequency. Further increases in sound frequency result in a smaller but still positive anomaly. This prediction is due to the resonance nature of the vibrating string model and is independent of the loop length distribution. The fact that, within the experimental accuracy, the sound velocity in solid helium during cooling always showed this frequency dependence is perhaps the strongest evidence in favour of the dislocation explanation of the anomaly. The quantitative disagreements between the predicted and measured sound velocities at different frequencies could easily be due to the choice of an exponential loop length distribution.

The attenuation is predicted by the Granato-Lücke theory and, since no adjustable parameters are involved, it provides an additional test of the theory. As noted in Chapter 4, the dislocation predictions for the attenuation almost always agreed qualitatively with the measurements. That is, the relative sizes of the attenuation at different frequencies and the approximate temperatures of the maxima in α were correctly predicted. In some crystals (e.g. hcp ^3He 3), the magnitude of the predicted attenuation was approximately correct while in others (e.g. hcp ^4He 1) the predicted attenuation was a factor of 3 too small.

Some of this discrepancy was no doubt due to the choice of an exponential distribution. By choosing a

different distribution, the relative sizes of the velocity and attenuation anomalies could easily be changed by a factor of 2. Another possibility was the assumption of isotropy. The three hcp ^4He crystals grown at $17.7 \text{ cm}^3/\text{mole}$ which had the same sound velocity (and presumably the same orientation) also had the same ratio of approximately 3 between the measured and predicted attenuation but in ^3He where a range of orientations were observed, there was no such consistency.

The orientation dependence of the anomaly is also unambiguously predicted by the Granato-Lücke theory. In hcp crystals, the orientation factor R is expected to be of the form shown in figure 2.4, varying between zero and about 0.13 for longitudinal sound. This orientation dependence has been verified by Tsuruoka and Hiki (1979) in hcp ^4He . Although the slip systems in bcc materials are not well enough defined to calculate the orientation factor, it is expected to be much more isotropic than in hcp materials. In fcc materials, the orientation factor varies only between about 0.04 and 0.09 (Green and Hinton (1966)) and a similar orientation dependence is likely in bcc materials.

The anomalies observed in helium have this orientation dependence. Although the orientations could not be determined in ^3He , the observed range of velocities (10% in hcp ^3He , 15% in bcc ^3He) indicate that a wide range of orientations were obtained in both phases. However, the

size of the anomaly (RA) varied by about two orders of magnitude in hcp ^3He but only by a factor of three in bcc ^3He .

In hcp ^4He , little orientation dependence was seen, no doubt because the crystals at each density had the same orientation. Since the elastic constants of hcp ^4He are known, the orientations of the hcp ^4He crystals could be estimated from the sound velocities. The crystals grown at $20.3 \text{ cm}^3/\text{mole}$ (which showed a very large attenuation anomaly) all had an orientation of $\theta = 57 \pm 5^\circ$, corresponding to a large orientation factor of about 0.1. The orientation of the crystals grown at $17.7 \text{ cm}^3/\text{mole}$ (which showed a much smaller anomaly) could not be uniquely determined since the velocity is double valued (cf. figure 2.1). The two possible orientations were $\theta = 44 \pm 4^\circ$ ($R \approx 0.11$) and $\theta = 80 \pm 10^\circ$ ($R \lesssim 0.01$). In view of the observed tendency of hcp helium crystals to grow with the c-axis perpendicular to the growth direction (Fraas et al (1977)), the orientation $\theta \approx 80^\circ$ is more likely and the smaller anomaly can be explained in terms of the orientation factor alone.

The amplitude dependence observed in ***hcp ^3He 17 (cf. figure 4.20) also supports the dislocation theory since it can be explained in terms of stress induced breakaway from impurity pinning points. The binding energy obtained ($W_B \sim 250 \text{ mK}$) is similar to that obtained by Iwasa and Suzuki (1980) for ^3He in hcp ^4He ($W_B \sim 300 \text{ mK}$) but binding

energies measured in hcp ^4He by other techniques vary from 0.7 K (Paalanen et al (1981)) to 1.8 K (Tsymbalenko (1979)). Theoretical estimates of the binding energy between an edge dislocation and an isotopic impurity in helium vary between 0.6 K (Iwasa and Suzuki (1980)) and 2.8 K (Tsuruoka and Hiki (1979)) so it is difficult to compare theory to experiment.

The temperature dependence of the velocity anomaly is important. Since all theories of dislocation damping predict a damping increasing with temperature, the observed adiabatic velocity and low attenuation at high temperatures is expected. Since the damping affects the long loops most, the short loops should be dominant at high temperatures, resulting in a negative although perhaps small velocity anomaly. At low temperatures, the long loops become undamped and, depending on the distribution, may give a positive velocity anomaly. Several crystals (e.g. hcp ^4He 1 at 9 MHz) had a negative anomaly at high temperatures and a positive one at low temperatures but none showed the opposite behaviour (i.e. a positive anomaly at high temperature and a negative one at low temperature), in agreement with expected behaviour. The existence of a velocity anomaly which changes from positive to negative as the temperature is raised is evidence for a distribution of loop lengths rather than a single length.

The values of the damping parameter B which were found from the velocity data should be properties of the

lattice and not of the dislocation network and so should be reasonably consistent in crystals at the same density.

In fact, B varies only by a factor of about two in hcp ^3He and ^4He and only by about 20% in bcc ^3He .

Since the temperature dependence of the damping was found to be approximately $B \propto T^3$, the values found can be compared to the damping due to the fluttering mechanism. At low temperatures, this is (Ninomiya (1974))

$$B \approx \frac{14.4 k_B}{\pi h^2 c^3} T^3 \quad (5.1-4)$$

where c is an average which may be taken as the Debye velocity. For bcc ^3He at $20.1 \text{ cm}^3/\text{mole}$ ($c \approx 310 \text{ m/sec}$), the fluttering value of B is about $1.1 \times 10^{-8} T^3 \text{ mks}$. This compares to the observed range of B from 2.21×10^{-8} to $2.76 \times 10^{-8} T^3 \text{ mks}$ (table 7). In hcp ^3He at $18.6 \text{ cm}^3/\text{mole}$, the fluttering value of B is about $4.3 \times 10^{-9} T^3 \text{ mks}$ while the observed range is from 5.67×10^{-9} to $2.25 \times 10^{-8} T^3 \text{ mks}$. Considering the uncertainties in determining B from the data and in the theoretical value, the agreement (within a factor of about 5) is quite good. The decrease in B with increasing density agrees with the fluttering prediction.

It should also be mentioned that the fact that the anomaly is essentially independent of isotope agrees with the dislocation interpretation but eliminates any explanation that depends on the statistics (Fermi or Bose). The suppression of the anomaly when isotopic impurities are

added is also expected if dislocations are the cause since the impurities simply pin the dislocations, but it is difficult to understand if the anomaly is either a bulk property of the crystal or is due to point defects.

It thus appears that the Granato-Lücke theory provides a good description of the sound anomaly observed in solid helium during cooling. The dislocation parameters take on reasonable values and the damping is well described by the fluttering expression (5.1-4). Most of the discrepancies between the theory and experiment may be due to the choice of loop length distribution.

The effect of high amplitude 3 MHz pulses at low temperature is not as well understood. At high densities in ^3He or in ^4He , the changes in the anomaly when the 3 MHz pulses are applied can invariably be interpreted as a shortening of the loop lengths. The attenuation decreases and positive velocity anomalies become negative and become small when many pulses are applied. This was studied in most detail in the crystal hcp ^3He 5 shown in section 4.2-1 but the behaviour was the same in bcc ^3He and hcp ^4He .

During the thermally activated recovery of the anomaly at high temperatures, the loop length increases. Comparing the recovery curve for bcc ^3He 43 shown in figure 4.46 to the curve shown in figure 2.3 for the dislocation contribution to velocity as a function of loop length supports this assertion.

The reproducibility of the anomaly after warming

above the recovery temperature indicates that the high amplitude pulses did not irreversibly change the dislocation network (as would be expected if plastic flow occurred).

There are some puzzling features of the high amplitude pulse effect. In hcp ^3He 5, the values of B and RA found after the application of high amplitude pulses disagreed with those found from the anomaly during cooling by factors of about 5. Although part of this may be due to the choice of an exponential loop length distribution and to the fact that the large changes in average loop length observed are unlikely to preserve the form of the distribution, it is difficult to explain the large change in B .

The overshoot of the attenuation past its cooling value observed in the recovery in bcc ^3He (e.g. figure 4.32) is also unexplained since figure 2.3 shows only a small increase of α above its final value and then only at low damping. This too may be connected to the non-exponential length distribution.

Although it seems that the effect of the large 3 MHz pulses is to shorten the loops, the pinning mechanism is not known. Isotopic impurities pin the dislocations at concentrations around 1000 ppm but they don't seem to be directly connected to the pinning effect of the large pulses since the pulses have essentially the same pinning effect in pure crystals ($\lesssim 1$ ppm of impurities) as in crystals with 430 ppm. It is still possible that the 1 ppm or so of

impurities is important in the pinning.

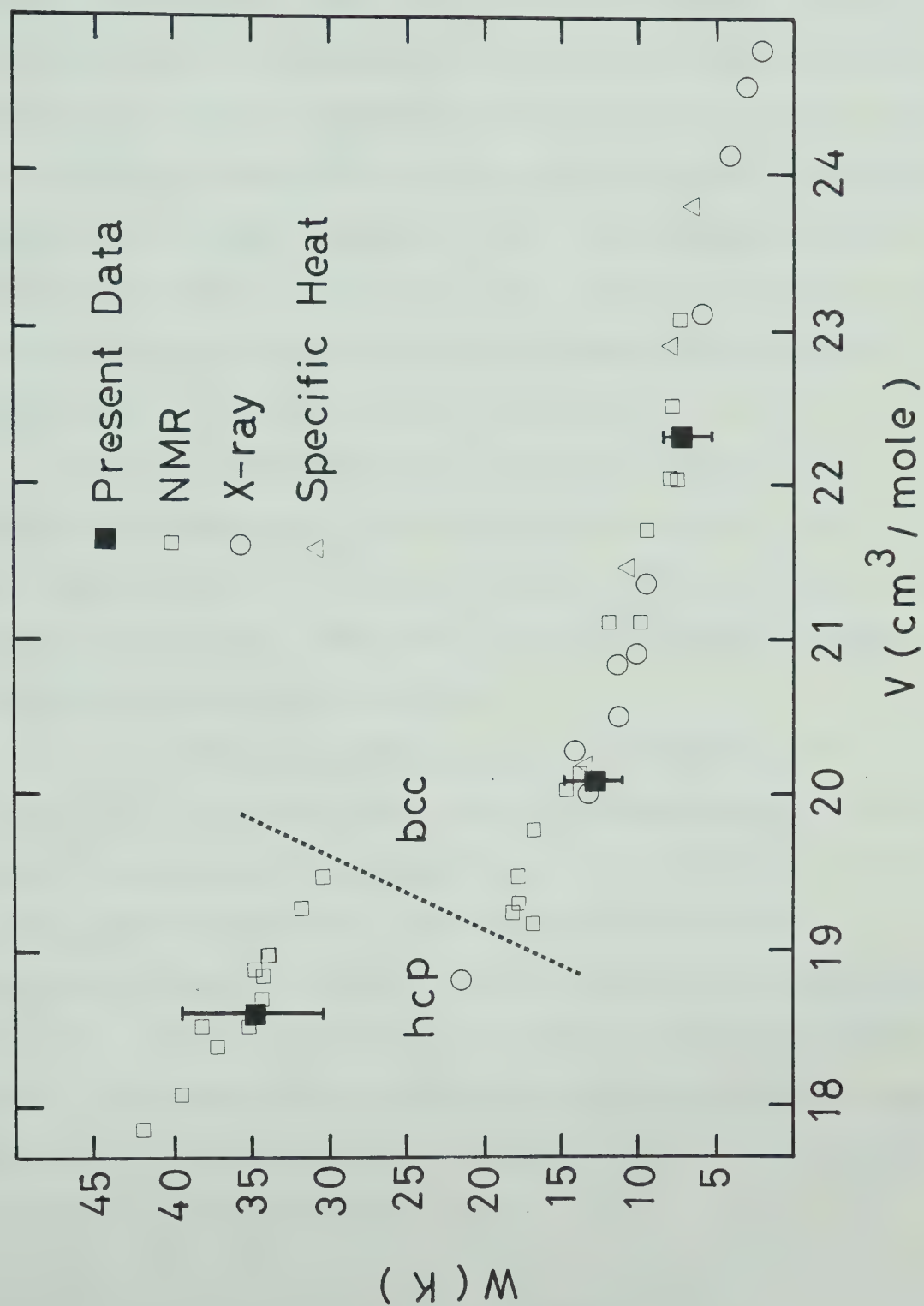
Another possibility is the creation of jogs on the dislocations under the action of the large pulses but it is not clear how effectively these would pin the dislocations.

The behaviour during recovery does not help to resolve this question since most pinning mechanisms (including impurities and jogs) can only leave the dislocations via thermally activated processes.

In any event, the pinning seems to require large displacements of the dislocations since it occurs only at low temperatures (where the damping is small), at large stress amplitudes and at low frequencies, each of which contributes to large dislocation motions.

The activation energies listed in table 5 for the recovery process correspond closely to the activation energies for mobile vacancies in ^3He . These activation energies can be derived from NMR, specific heat and X-ray measurements. These values are shown in figure 5.1 along with the activation energies from the recovery rates as listed in table 5. The NMR and specific heat values are taken from Sullivan et al (1975) and the X-ray values from Heald (1976). The agreement is excellent, leading to the conclusion that the dislocation unpinning is accomplished by mobile vacancies. These could allow impurities to diffuse away from the dislocations or jogs to anneal out.

The low density bcc ^3He crystals behave somewhat

Figure 5.1 Vacancy Activation Energies in ^3He

differently. As the density is decreased, the anomaly observed on cooling decreases until at $22.3 \text{ cm}^3/\text{mole}$ it is barely observable. This could mean that there are few dislocations at low densities or that they are immobile. Iwasa et al (1981) maintain that most dislocations in bcc crystals are screw dislocations and that these cannot move because of a large Peierls stress. The existence of an anomaly in higher density bcc ^3He , however, indicates that it is not the structure which is responsible for the absence of an anomaly at low densities.

The fact that the high amplitude pulses seem to create an anomaly at low densities (cf. figure 4.27) is not understood. It may not be connected to the anomaly observed at higher densities. It would require further investigation to resolve this.

The complete pinning of the dislocation anomaly in ***hcp ^3He 17 allowed the remaining attenuation to be compared to the zero sound prediction. As shown in figure 4.49, the attenuation at low temperatures has the T^4 dependence and the linear dependence on ω which are predicted. Similar measurements by Iwasa and Suzuki (1980) on hcp ^4He containing 1% ^3He showed essentially the same behaviour. They found $\alpha = 1.9 \times 10^{-9} \omega T^4 \text{ db/cm}$ (at $20.06 \text{ cm}^3/\text{mole}$) compared to the value

$$\alpha = 5.5 \times 10^{-9} \omega T^4 \text{ db/cm} \quad (4.8-1)$$

found in section 4.8 for hcp ^3He at $18.6 \text{ cm}^3/\text{mole}$. The difference of a factor of 3 in the coefficient may be due either to the difference in isotope or in molar volume.

5.2 Conclusion

In conclusion, the experiments described in this thesis showed that the sound velocity anomaly previously observed in hcp ^4He is also present in both hcp and bcc ^3He . The size of the anomaly is similar in the two isotopes and is approximately the same as observed in previous work on hcp ^4He . The anomaly observed during cooling agreed well with the Granato-Lücke theory of dislocation resonance and the dislocation densities, loop lengths and damping assumed reasonable values. It was found that, by applying large 3 MHz pulses at low temperatures, the anomaly could be reduced in a manner which suggested that the dislocations were being pinned. Although the pinning mechanism was not determined, it was found that the dislocations were unpinned by thermal vacancies at about one half of the melting temperature. By adding isotopic impurities, the dislocations could also be pinned. From the amplitude dependence of the attenuation in an impure hcp ^3He crystal, an estimate of the binding energy between a ^4He impurity and a dislocation was obtained. When the dislocations were completely pinned, the remaining attenuation agreed well with the theory of zero sound.

BIBLIOGRAPHY

- Abraham, B.M., Eckstein, Y., Ketterson, J.B., Kuchnir, M.,
Roach, P.R., Phys. Rev. A1, 250 (1970).
- Ackerman, C.C., Overton, W.C., Phys. Rev. Lett. 22, 764
(1969).
- Akhieser, A., J. Phys. (USSR) 1, 277 (1969).
- Amelinckx, S., Dislocations in Solids, F.R.N. Nabarro, ed.,
Vol. 2, p. 201, North-Holland, Amsterdam (1979).
- Andreev, A.F., Sov. Phys. Usp., 19, 137 (1976).
- Balluffi, R.W., Granato, A.V., Dislocations in Solids,
F.R.N. Nabarro, ed., Vol. 4, p. 3, North-Holland,
Amsterdam (1979).
- Berberich, P., Leiderer, P., Hunklinger, S., J. Low Temp.
Phys. 22, 61 (1976).
- Bhatia, A.B., Ultrasonic Absorption, Clarendon Press,
Oxford, (1967).
- Brailsford, A.D., J. Appl. Phys. 43, 1380 (1972).
- Calder, I.D., Ph.D. Thesis, University of Alberta,
Edmonton (1977, unpublished).
- Calder, I.D., J. Acoust. Soc. Am. 63, 967 (1978).
- Calder, I.D., Franck, J.P., Phys. Rev. B15, 5262 (1977).
- Calder, I.D., Franck, J.P., J. Low Temp. Phys. 30, 579 (1978).
- Crepeau, R.H., Heybey, O., Lee, D.M., Strauss, S.A., Phys.
Rev. A3, 1162 (1971).
- de Batist, R., Internal Friction of Structural Defects in
Crystalline Solids, North-Holland, Amsterdam (1972).
- de Wette, F.W., Nijboer, B.R.A., Phys. Lett. 18, 19 (1965).
- Edwards, D.O., McWilliams, A.S., Daunt, J.G., Phys. Rev.
Lett. 9, 195 (1962).
- Fraas, B.A., Heald, S.M., Simmons, R.O., J. Crystal Growth
42, 370 (1977).
- Franck, J.P., Hewko, R.A.D., Phys. Rev. Lett. 31, 1291 (1973).
- Fredkin, D.R., Werthamer, N.R., Phys. Rev. 167, 607 (1965).

- Friedel, J., Dislocations, Pergamon, Oxford (1964).
- Garber, J.A., Granato, A.V., J. Phys. Chem. Solids 31, 1863 (1970).
- Gerold, V., Dislocations in Solids, F.R.N. Nabarro, ed., Vol. 4, p. 219, North-Holland, Amsterdam (1979).
- Gifford, R.P., Truscott, W.S., Hatton, J., J. Low Temp. Phys. 4, 153 (1970).
- Glyde, H.R., Rare Gas Solids, M.L. Klein, J. A. Venables, eds. Vol. 1, p. 382, Academic Press, N.Y. (1976).
- Granato, A.V., Lücke, K., J. Appl. Phys. 27, 583 (1956).
- Green, R.E., Hinton, T., Trans. AIME 236, 435 (1966).
- Greenberg, A.S., Armstrong, G., Phys. Rev. B20, 1050 (1979).
- Greenberg, A.S., Armstrong, G., Phys. Rev. B22, 4336 (1980).
- Greywall, D.S., Phys. Rev. A3, 2106 (1971).
- Greywall, D.S., Phys. Rev. B11, 1070 (1975).
- Greywall, D.S., Phys. Rev. B13, 1056 (1976).
- Greywall, D.S., Phys. Rev. B15, 2604 (1977).
- Gudenko, A.V., Tsymbalenko, V.L., Sov. Phys. JETP 49, 712 (1979).
- Guenin, B.M., Dahm, A.J., Phys. Rev. B23, 1139 (1981).
- Guyer, R.A., Solid State Physics 23, 413 (1969).
- Guyer, R.A., Krumhansl, J.A., Phys. Rev. 133, A1411 (1964).
- Heald, S.M., Ph.D. Thesis, University of Illinois at Urbana-Champaign (1976, unpublished).
- Henneke, E.G., Green, R.E., Trans. AIME 239, 231 (1967).
- Hetherington, J.H., Phys. Rev. 176, 231 (1968).
- Hikata, A., Kwun, H., Elbaum, C., Phys. Rev. B21, 3932 (1980).
- Hirth, J.P., Lothe, J., Theory of Dislocations, McGraw-Hill N.Y. (1968).
- Hogan, E.M., Guyer, R.A., Fairbank, H.A., Phys. Rev. 185, 356 (1969).

- Holder, J., Rev. Sci. Instr. 41, 1355 (1970).
- Iwasa, I., Araki, K., Suzuki, H., J. Phys. Soc. Jpn. 46, 1119 (1979).
- Iwasa, I., Suzuki, H., J. Phys. Soc. Jpn. 49, 1722 (1980).
- Iwasa, I., Saito, N., Suzuki, H., Physica 107B, 203 (1981).
- Iwasa, I., Suzuki, H. (1981, to be published).
- Iwasa, I., Saito, N., Suzuki, H. (1981, to be published).
- Koehler, J.S., Imperfections in Nearly Perfect Crystals, John Wiley and Sons, N.Y. (1952).
- Maradudin, A.A., Montroll, E.W., Weiss, G.H., Ipatova, I.P., Solid State Physics Suppl. 3, 1 (1971).
- Maris, H.J., Physical Acoustics, W.P. Mason, ed., Vol. VIII, p. 279, Academic Press, N.Y. (1971).
- Meierovich, A.E., Sov. Phys. JETP 40, 368 (1975).
- Mikheev, V.A., Essel'son, B.N., Grigoriev, V.N., Mikhin, N.P., Fiz. Nizk. Temp. 3, 385 (1977).
- Mineev, V.P., Sov. Phys. JETP 36, 964 (1973).
- Minkiewicz, V.J., Kitchens, T.A., Shirane, G., Osgood, E.B., Phys. Rev. A8, 1513 (1973).
- Mullin, W.J., Phys. Rev. Lett. 20, 254 (1968).
- Musgrave, M.J.P., Crystal Acoustics, Holden-Day, San Francisco (1970).
- Nabarro, F.R.N., Theory of Crystal Dislocations, Clarendon, Oxford (1967).
- Ninomiya, T., J. Phys. Soc. Jpn. 36, 399 (1974).
- Nosanow, L.H., Phys. Rev. 146, 120 (1966).
- Paalanen, M.A., Bishop, D.J., Dail, H.W., Phys. Rev. Lett. 46, 664 (1981).
- Papadakis, E.P., Physical Acoustics, W.P. Mason and R.N. Thurston, eds., Vol. XII, p. 277, Academic Press, N.Y. (1976).
- Sakai, A., Nishioka, Y., Sukuki, H., J. Phys. Soc. Jpn. 46, 881 (1979).

Sanders, D.J., Kwun, H., Hikata, A., Elbaum, C., Phys. Rev. Lett. 39, 815 (1977).

Sanders, D.J., Kwun, H., Hikata, A., Elbaum, C., Phys. Rev. Lett. 40, 458 (1978).

Sullivan, N., Deville, G., Landesman, A., Phys. Rev. B11, 1858 (1975).

Suzuki, H., J. Phys. Soc. Jpn., 42, 1865 (1977).

Thomlinson, W.C., J. Low Temp. Phys. 9, 167 (1972).

Truell, R., Elbaum, C., Chick, B.B. Ultrasonic Methods in Solid State Physics, Academic Press, N.Y. (1969).

Tsuruoka, F. and Hiki, Y., Phys. Rev. B20, 2702 (1979).

Tsymbalenko, V.L., Sov. Phys. JETP 47, 787 (1978).

Tsymbalenko, V.L., Sov. Phys. JETP 49, 859 (1979).

Vignos, J.H., Fairbank, H.A., Phys. Rev. 147, 185 (1966).

Wanner, R., Ph.D. Thesis, University of Alberta, Edmonton (1970, unpublished).

Wanner, R., Franck, J.P., Phys. Rev. Lett. 24, 365 (1970).

Wanner, R., Mueller, K.H., Fairbank, H.A., J. Low Temp. Phys. 13, 153 (1973).

Wanner, R., Iwasa, I., Wales, S., Solid State Comm. 18, 853 (1976).

B30337